USE OF OPTICAL SUPERBEAMS IN ATMOSPHERIC TURBULENCE APPLICATIONS

by

Yalong Gu

A dissertation submitted to the faculty of
The University of North Carolina at Charlotte
in partial fulfillment of the requirements
for the degree of Doctor of Philosophy in
Optical Science and Engineering

Charlotte

2011

Approved by:

_____
Dr. Gregory J. Gbur

_____
Dr. Wei Cai

_____
Dr. Michael A. Fiddy

_____
Dr. Robert K. Tyson

_____
Dr. Praveen Ramaprabhu

ABSTRACT

YALONG GU. Use of Optical Superbeams in Atmospheric Turbulence Applications.
(Under the direction of DR. GREGORY J. GBUR)

The use of nonconventional beam classes in turbulence applications is investigated. Through the study on pseudo-Bessel correlated beam propagation in the atmosphere, it is shown that scintillation reduction by a partially coherent beam can be obtained by a corresponding incoherent beam array with finite number of beamlets. General guidelines for scintillation reduction by incoherent beam arrays are developed; these guidelines include reducing correlation of beamlet atmospheric propagation, maximizing the total intensity arriving at the detector, and selecting beamlets with small scintillation. With these goals in mind, Airy beams, a novel beam class, are applied to generate an incoherent beam array whose scintillations are significantly reduced. By the analogy with two-mode partially coherent beams, nonuniformly polarized beams are demonstrated to be of small scintillation. This suggests a relatively easy and inexpensive method to reduce the scintillation of a coherent optical beam. Finally a method to measure atmospheric turbulence strength by using vortex beams is proposed and its feasibility is theoretically demonstrated.

ACKNOWLEDGEMENTS

My thanks go to my parents, Zhaokang Gu and Weixia Wang, for their constant support throughout my whole education.

Special thanks go to my beloved wife, Yue Dong. Her support and belief in me are indispensable for this dissertation.

I would like to thank Prof. Wei Cai, Prof. Michael Fiddy, Dr. Robert Tyson and Dr. Praveen Ramaprabhu for serving on my dissertation committee.

Thanks to all instructors who have imparted knowledge of optical sciences in the past five years, including Dr. Angela Davies, Dr. Tsing-Hua Her, Prof. Eric Johnson, Prof. Yasin Raja and Dr. Thomas Suleski.

My gratitude goes to Dr. Olga Korotkova and Prof. Taco Visser for their advice in my dissertation research.

I would like to thank my former group colleague, Dr. Choon How Gan, for not only providing insightful discussions on research project but also creating a good research atmosphere in Grigg 242.

Finally, I am deeply indebted to my advisor, Dr. Greg Gbur. When I first caught a glimpse of his name in the reference list of an *Applied Optics* paper in late 2004, I never imagined that I could finish my dissertation under his supervision today. Studying abroad is in itself a challenge. This dissertation would not have been possible without his patient guidance on both academic subjects and English writing skills. The four-year dissertation research under his guidance would be a great experience in my life. In one our meeting in Fall 2007, he said that a graduate student should know more

than his advisor in his research field. I hope I can make it some day in the future.

I am grateful for funding support from the United States Air Force Office of Scientific Research under grant FA9550-08-1-0063.

TABLE OF CONTENTS

LIST OF TABLES

LIST OF FIGURES

CHAPTER 1: OPTICAL BEAM PROPAGATION IN ATMOSPHERE

The technique of communicating with light over long distances has been used since nearly the dawn of history. The Lighthouse of Alexandria, completed in the third century BC, guided ships into the harbor at night time by sending navigation signals in the form of light [1]. Roughly in the same period, the Great Wall of China was built in northern China. One of its missions was early warning of nomadic invaders. The signal of invasion was relayed through the fires on the top of the sequential beacon towers [2]. Light gave ancient people a fast and long-range communication method to convey important information.

Effective communication requires rapid transmission of information over significant distances. Increasing the information transmission rate has been one of the fundamental motivations in the development of communication systems. The ancient optical communications operated at very low rate and only sent simple information. Techniques become more sophisticated in modern times. The heliograph, which appeared in the 19th century, is a wireless telegraph that uses reflected sunlight flashes as signals. With Morse code, the heliograph can send relatively complicated information over tens of kilometers. In 1880, a successful intercontinental heliograph communication was reported. Through relay, a message was delivered from Afghanistan to London in a day [3].

A revolutionary development of wireless telecommunication began in the early 20th century, following the pioneering work by Marconi. A typical telecommunication system sends information by modulating a sinusoidal electromagnetic wave, which is known as the *carrier*. In principle the amount of transmitted information is directly related to the frequency range of the carrier, which can be enlarged by increasing the carrier's frequency. The width of the radio frequency band is from 10^3 Hz to 10^8 Hz, while the width of the optical frequency band is from 10^{14} Hz to 10^{15} Hz. The high bandwidth of the optical frequency range makes very high speed communications possible. Therefore the development of telecommunication systems led to exploring optical frequencies as the carriers.

Modern free-space optical communication has been developed since the invention of lasers in 1960s. Lasers possess several extraordinary characteristics that regular light sources do not have, including high brightness, directionality, monochromaticity and spatial coherence. Therefore they are reliable light sources which enables people to extend radio frequency atmospheric communication to the optical frequency band. Its highly directional nature also makes the communications highly secure. However, as the signal transmission channel of free-space optical communication, the atmosphere is a random medium. Due to the short wavelength of optical frequency wavefield, the fluctuations of the refractive index of the atmosphere cause variations in the amplitude, phase and polarization of the propagating optical beams, resulting in a variety of deleterious effects. The random nature of the atmosphere imposes inherent obstacles on the development of free-space optical communication systems.

The efforts to mitigate turbulence effects and improve the performance of free space optical communication systems requires the knowledge of optical beam propagation in the atmosphere, which must be determined separately. Wave propagation in random media has been a subject of extensive research for many decades. Several excellent articles and books provide comprehensive reviews on the advances of this subject in different periods of the last half-century [4–10]. In the late 1950s, Chervon and Tatarskii made the first two complete treatments on the problem of wave propagation in random media [11, 12]. By using the Rytov approximation [13, Chapter 13], the propagation characteristics of plane waves were investigated. The study was extended to the case of spherical waves [14, 15] and directional beams in the late 1960s. Schmeltzer formulated the general expressions for beam wave propagation in random media [16]. Based on these formulas, the turbulence induced amplitude fluctuations of optical beams were identified [17, 18]. Ishimaru also studied the problem of laser beam propagation and gave interpretations in terms of spectral expansions [19, 20].

Although the early theories provided a preliminary framework on the study of wave propagation in random media, they failed to explain certain phenomena observed in experiments. For example, on propagating through the near earth atmosphere, the irradiance fluctuations of a plane wave would initially increase as predicted in Ref. [12], but gradually stop increasing and eventually saturate [21]. This discrepancy is due to limitations of the Rytov approximations applied in the early theories, which assumes smooth and weak perturbations. However, it is not applicable as the propagation path

or the turbulence strength increases because the fluctuations are no longer small.

Various theoretical approaches were proposed to circumvent this limitation. The parabolic equation method is one of the most general methods applicable under all fluctuation conditions [9]. Another method is the extended Huygens-Fresnel principle. It was first developed by Feizulin and Kravtsov in the former USSR [22] and Lutomirski and Yura in the USA [23]. Combined with the quadratic approximation of the turbulence term [24], the extended Huygens-Fresnel principle has been widely used in the studies of the second order statistical propagation properties of various types of beam in the atmosphere (see, for instance, [25, 26]).

Scintillation, the fourth order statistical moment, is another significant property of wave propagation in random media. It characterizes the intensity fluctuations of a wavefield and strong scintillation is a big limitation for free-space optical communication. The scintillation indices of plane waves, spherical waves and Gaussian beams in weak fluctuations have been obtained by the Rytov method [9, 10]. In recent years, Baykal et al. used the Rytov method to investigate the scintillation properties of various beam types in weak turbulence [27]. The nature of wave scintillations in strong fluctuation conditions is a challenging issue. The extended Huygens-Fresnel principle is not applicable for the fourth order moment under these conditions, while the exact solutions of the parabolic equation method only exist in the case of first and second order moments of the wavefield. An asymptotic theory for laser beam scintillations in the saturation regime was developed in the mid 1970s [28, 29]. A strong scintillation theory was later

developed based on the path-integral approach [8, 30]. It was applied in the analysis of beam scintillations for the ground-to-space propagation paths [31, 32]. Recently, Andrews et al. introduced an approximation technique based on a modification of the Rytov method and extended many weak fluctuation results into the moderate-to-strong fluctuation regimes [10].

In general, the existing theories for the statistical moments, especially the fourth order moment, of a wavefield in random media are analytically intractable. However, numerical simulations are straightforward and applicable in all fluctuation conditions. Wave propagation in a random medium can be simulated by a multiple random phase screen method [33], in which an extended medium is modeled by a collection of random phase screens with appropriate statistical properties, and the wavefield undergoes free-space propagation between them. By this method, Martin and Flatté first numerically studied the intensity fluctuations of plane waves and spherical waves in the atmospheric turbulence [33, 34]. Several algorithms were later proposed to generate random phase screens with high accuracy (see, for instance, [35, 36]). Recently Schmidt wrote a comprehensive review of the numerical simulation methods for wave propagation in random media [37, Chapter 9]. Today, numerical simulations are indispensable tools in the study of wave propagation in random media.

Over decades of studies, the propagation characteristics of conventional Gaussian laser beams in the atmosphere have been well-determined. The associated turbulence effects, including scintillation, beam spreading, beam wander and

decrease of spatial coherence, severely affect the performance of free-space optical communication systems [10]. Numerous efforts have been done to mitigate these turbulence effects. One promising research direction is to develop beam classes other than conventional Gaussian beams which have superior properties in atmospheric propagation, loosely referred to as 'superbeams'. These unconventional beam classes include partially coherent beams, vortex beams and Airy beams. In particular, the observations of improved propagation characteristics of partially coherent beams in the atmosphere suggests their application in free-space optical communications.

Early studies focused on the evolution of the mutual coherence function of a coherent laser beam propagating in turbulence [24, 38, 39]. Fante derived the expression for the generalized two-position, two-frequency mutual coherence function of an electromagnetic beam in a turbulent medium by using the extended Huygens-Fresnel principle [40]. The state of source coherence was later incorporated and the propagation characteristics of partially coherent beams in the atmosphere were investigated, including the dependence of the average light intensity on the degree of source coherence [41], the influence of source coherence on the coherence radius of the propagated beam [42] and the relation between the far field intensity angular distribution and the source coherence [43]. One of the most intriguing observations of partially coherent beam propagation in the atmosphere in the early studies is the scintillation properties of such beams. It was found that the scintillation of a partially coherent beam can be lower than that of its fully coherent counterpart [44–47].

The early observations of scintillation reduction by partially coherent beams made the study of partial coherence based turbulence effects a topic of renewed interest in the new millennium. By using the extended Huygens-Fresnel principle, Gbur and Wolf investigated the turbulence-induced spreading effects of partially coherent beams and showed that they are less affected than fully coherent beams [48], a result that was experimentally demonstrated by Dogariu and Amarande [49]. This property was also studied by using a Hilbert-space method [50] and the coherent mode representation method [51]. Salem et al. investigated the beam spreading effect of partially coherent beams in a long-distance atmosphere propagation and showed that they are less affected by changes in the atmospheric conditions [52]. The turbulence-induced beam spreading effects of various types of partially coherent beams have also been investigated in the recent years (see, for instance, [53, 54]).

The most important application of partially coherent beams in free-space optical communications is scintillation reduction. By modeling partial coherence with a thin (complex) phase screen with a Gaussian spectrum, Korotkova et al. showed that a Gaussian Schell-model beam has lower scintillation than a fully coherent counterpart [55]. Later Schulz theoretically showed that the beam that minimizes the scintillation index is in general partially coherent [56]. Since then, a large amount of work has been done on the study of various strategies for reducing scintillation with partial coherence. By passing a coherent Gaussian beam through a time-varying phase screen, Xiao et al. proposed a model of pseudo-partially coherent beam. The partially coherent characteristics are obtained along with the

inherent time averaging of the photodetection process [57]. Their application in free-space optical communications was also studied [58, 59]. Berman et al. proposed a spectral coding method to suppress the intensity fluctuations of a partially coherent beam in free-space high-speed optical communication [60]. Incoherent beam arrays have been investigated as an easily constructed partially coherent source. Peleg et al. demonstrated, both theoretically and experimentally, the scintillation reduction with beams of different wavelengths [61–63]. Baykal et al. also studied a Gaussian beam array whose constituent beamlets are partially coherent [64]. Beside partially spatially coherent beams, partially temporally coherent beams were also considered[1]. Kiasaleh studied the scintillations of a multiwavelength Gaussian beam [65].

Inspired by the results of fundamental propagation properties of partially coherent beams in the atmosphere, people have investigated the performance of free-space optical communication systems using partially coherent beams (see, for instance [66, 67]). The design of a free-space optical communication system is based on the balanced considerations among several key parameters. For example, both low scintillation and high received intensity are desired. Several studies have been performed on optimization of partially coherent beams for free-space optical communications. Based on the probability density function of the intensity fluctuations, Chen et al. proposed a criterion to optimize the initial state of source coherence [68]. Voelz and Xiao developed a different metric to determine the

[1]Unless otherwise specified, the term "partially coherent" in this dissertation is referred to as being partially spatially coherent.

characteristics of the optimized coherence length that balance the effects of beam spreading and scintillation [69]. More recently, Borah and Voelz analyzed the selection of partially coherent parameters specific to the optical communication problems, which concerned the performance optimization as a function of various communication link parameters [70].

Although a large amount of work has been done on the application of partially coherent beams in free-space optical communication, several important questions remain. The foremost among these is that the underlying physics of scintillation reduction by partially coherent beams is still obscure. Although Schulz demonstrated an optimal solution in Ref. [56], his results are expressed in the form of a general mode decomposition,which is not readily implemented. In addition, besides partially coherent beams, it has been revealed that several other unconventional beam classes possess exotic and potentially helpful properties; of most interest are vortex beams and Airy beams.

In recent years, optical beams which possess an intensity null along their propagation axis have attracted much attention. They are usually named as *vortex beams* due to the symbolic helical phase structures around the intensity nulls. Vortex beams have been investigated for various applications, including laser communications [71, 72], optical tweezers and spanners [73]. One of their most attractive features is the orbital angular momentum carried by these beams [74]; with this vortex beams may propagate in the atmosphere less distorted than conventional Gaussian beams [71, 75]. It has also been shown that they can

'self-heal' around certain obstacles [76]. Besides orbital angular momentum, vortex beams also carry conserved and discrete topological charge. Recent work shows that the charge is relatively stable when a vortex beam propagates in the atmosphere and that it could be used as an information carrier in optical communications [77].

Airy beams are a newly discovered beam class, which are nondiffracting solutions of the paraxial wave equation. They can propagate along parabolic trajectories while keeping their transverse amplitude profiles invariant. The study also shows that they can resist external perturbations when propagating under turbulent conditions or passing through obstacles [78]. These attractive properties of vortex beams and Airy beams suggest their applications in the atmospheric turbulence.

This dissertation attempts to investigate the abovementioned phenomena. Our goal is to develop general guidelines for minimizing beam scintillation and to explore the possible applications of vortex beams and Airy beams in atmospheric turbulence. The whole dissertation is organized as follows: The basic theory, including the coherence theory, the optical properties of atmospheric turbulence, classic theory of optical beam propagation in the atmosphere, and the numerical simulations of optical beam propagation in the atmosphere, are summarized in Chapter 2. Scintillation reduction by incoherent beam arrays is discussed in Chapter 3. A new array configuration and constituent electromagnetic beamlets are applied in this chapter. The general guidelines for scintillation reduction by use of incoherent beam arrays are developed as well. In Chapter 4, the vector nature of beams is taken into account and the scintillation reduction associated with non-uniformly polarized beams is investigated.

The application of vortex beams in determining the atmospheric turbulence strength is studied in Chapter 5. Finally, conclusions are presented in Chapter 6.

CHAPTER 2: BASIC THEORY

The atmosphere is a thick layer of gases covering Earth, which is held in place by Earth's gravity. Due to the solar radiation and the Earth's rotation, it is warmed up in the daytime and gradually cools down in the night time. The induced temperature gradient gives rise to winds and convection, resulting in the disturbances of air masses. In addition, there are clouds and aerosol particles suspended in the atmosphere. The refractive index of atmosphere fluctuates in time and space and can be characterized by a random function of position and time. To begin with, it is worthwhile to distinguish two confusing terms, i.e. turbulent media and turbid media. The distinction between these two terms lies in the different character of the scattering mechanism relative to wavelength. For turbulent media, the typical distance over which the refractive index varies is much larger than the wavelength of the propagating beam. In addition, these refractive index variations are small and continuous in space. Temperature gradient induced refractive index fluctuations fall into this category. In contrast, the scatterers in turbid media, such as clouds, dusts and rains, are discrete and cause sharp discontinuities in refractive index. These distinctions make the propagation behaviors of optical beams as well as the corresponding calculational approaches very different for the types of media. This dissertation is devoted to beam propagation in so-called clean air atmospheric

turbulence.

Because of turbulent fluctuations, the coherence of an optical beam decreases on propagation in the atmosphere. The basics of coherence theory is briefly introduced in Sec. 2.1 of this chapter. The review of the optical properties of atmospheric turbulence and the classical theory of optical beam propagation in atmospheric turbulence are presented in Sec. 2.2 and Sec. 2.3 respectively. A summary of numerical simulation methods is given in Sec. 2.4.

2.1 Coherence Theory

Coherence theory may be defined as the study of the statistical properties of light. It is a quite broad subject and here its basic concepts which will be used in this dissertation is introduced. In general, an optical field possesses random fluctuations. Its electric field vector $\mathbf{E}(\mathbf{r}, t)$ is a random function of both space $\mathbf{r}$ and time t. For simplicity its scalar form $U(\mathbf{r}, t)$ is considered. The coherence theory can be easily extended to the electromagnetic case (vector field) which is discussed in detail in Ref. [79]. For a statistically stationary scalar wavefield, its cross correlation function, also known as the *mutual coherence function*, is defined as [80]

$$\Gamma(\mathbf{r}_1, \mathbf{r}_2, \tau) = \langle U(\mathbf{r}_1, t) U^*(\mathbf{r}_2, t + \tau) \rangle, \tag{2.1.1}$$

where the angle brackets indicate a time average or, equivalently, an ensemble average for ergodic fields. The *complex degree of coherence* is defined as the normalized form

of mutual coherence function,

$$\gamma(\mathbf{r}_1, \mathbf{r}_2, \tau) = \frac{\Gamma(\mathbf{r}_1, \mathbf{r}_2, \tau)}{\sqrt{\Gamma(\mathbf{r}_1, \mathbf{r}_1, 0)\Gamma(\mathbf{r}_2, \mathbf{r}_2, 0)}}, \tag{2.1.2}$$

where $\Gamma(\mathbf{r}, \mathbf{r}, 0) = I(\mathbf{r})$ is the average intensity at the position $\mathbf{r}$. The complex degree of coherence $\gamma(\mathbf{r}_1, \mathbf{r}_2, \tau)$ is a measure of the statistical similarity of wavefield fluctuations at the points $\mathbf{r}_1$ and $\mathbf{r}_2$ with a time delay τ. Its modulus $|\gamma(\mathbf{r}_1, \mathbf{r}_2, \tau)|$ can be obtained by measuring the visibility of double slit interference fringes [79]. It can be shown that $0 \leq |\gamma(\mathbf{r}_1, \mathbf{r}_2, \tau)| \leq 1$, where the extreme value unity denotes full coherence and the other extreme value zero means complete incoherence.

It is more convenient for our purposes, however, to work within the space-frequency domain. The *cross-spectral density* of the wavefield is defined as the temporal Fourier transform of the mutual coherence function with respect to the time delay τ [80, Sec. 4.3],

$$W(\mathbf{r}_1, \mathbf{r}_2, \omega) = \frac{1}{2\pi} \int_{-\infty}^{\infty} \Gamma(\mathbf{r}_1, \mathbf{r}_2, \tau) e^{i\omega\tau} d\tau. \tag{2.1.3}$$

The cross-spectral density characterizes the intensity and spatial coherence of the field at frequency ω, and contains the same information at the mutual coherence function. Its normalized form is called the *spectral degree of coherence*,

$$\mu(\mathbf{r}_1, \mathbf{r}_2, \omega) = \frac{W(\mathbf{r}_1, \mathbf{r}_2, \omega)}{\sqrt{W(\mathbf{r}_1, \mathbf{r}_1, \omega)W(\mathbf{r}_2, \mathbf{r}_2, \omega)}}, \tag{2.1.4}$$

where $W(\mathbf{r}, \mathbf{r}, \omega) = S(\mathbf{r}, \omega)$ is the intensity at the frequency ω and the position $\mathbf{r}$, also referred to as the *spectral density*. Like the complex degree of coherence, the magnitude of the spectral degree of coherence is also bounded between zero and

unity, i.e. $0 \leq |\mu(\mathbf{r}_1, \mathbf{r}_2, \omega)| \leq 1$.

It has been shown that the cross-spectral density of an arbitrary partially coherent wavefield at frequency ω may always be expressed as the average of an ensemble of monochromatic realizations of the field [81]

$$W(\mathbf{r}_1, \mathbf{r}_2, \omega) = \langle U^*(\mathbf{r}_1, \omega) U(\mathbf{r}_2, \omega) \rangle_\omega, \tag{2.1.5}$$

where $U(\mathbf{r}, \omega)$ is a monochromatic realization of the partially coherent field and the subscript ω denotes averaging with respect to this special ensemble. The advantage of this representation is that it allows one to construct models of partially coherent fields in the frequency domain directly without resorting first to finding the more complicated mutual coherence function. From now on a monochromatic field is considered and the depiction of frequency ω in the function arguments is suppressed. It is also noted that focusing on single frequency ω is equivalent to studying narrowband light wave.

2.2 Optical Properties of Atmospheric Turbulence

Atmospheric turbulence is chaotic motions of air characterized by winds varying in velocity and direction. As a result, air masses are unstable and eventually break up into turbulent eddies of different scale sizes. The structure of atmospheric turbulence can be understood by the *energy cascade theory* [10] (see Fig. 2.1). The action of wind creates unstable air masses with different characteristic dimension (eddies). These turbulent eddies have been shown to be bounded by two characteristic scales, the *outer scale* L_0 and the *inner scale* l_0. The turbulent eddies of size between these two

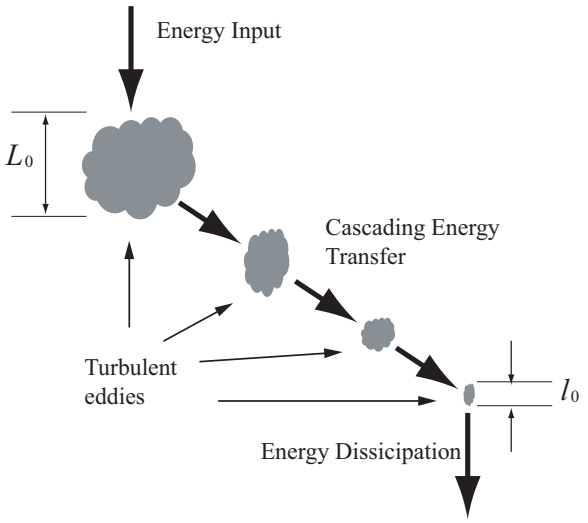

Figure 2.1: Illustration of energy cascade theory of atmospheric turbulence.

scales forms the inertial subrange. A fraction of wind energy is converted to turbulence energy at the outer scale L_0. Under the influence of inertial forces, the large eddies break up into small eddies and the input energy is transferred in a cascading manner until eddies reach the smallest size, the inner scale l_0. Turbulent eddies dissipate their energy through viscous effects below the inner scale l_0. Near the ground, the inner scale l_0 is typically of a few millimeters, while the outer scale L_0 varies between 1 m and 100 m. Because wavefronts of optical beams are of limited size, they are affected by large and small turbulent eddies in different manners. For example, large eddies randomly deflect propagation directions and induce beam wander and image dancing. On contrary, small eddies distort local wavefront of an optical beam and cause intensity fluctuations. Therefore optical beam propagation in the atmosphere depends on the values of inner scale and outer scale, known as the inner scale effects and the outer scale effects (see, for instance [82, 83]).

Due to the turbulent motions of air, the refractive index of atmosphere is a random

function of both space $\mathbf{r}$ and time t, which can be written as

$$n(\mathbf{r}, t) = n_0 + n_1(\mathbf{r}, t), \tag{2.2.1}$$

where $n_0 = \langle n(\mathbf{r}, t) \rangle \approx 1$ is the mean value of the refractive index $n(\mathbf{r}, t)$ and $n_1(\mathbf{r}, t)$ represents the random fluctuation about the mean value. The angle brackets denote an ensemble average. The refractive index fluctuations are the most important factor for various effects when optical beams propagate in the atmosphere, and therefore are commonly referred as *optical turbulence* [84]. In general, the rate of time variation of the refractive index $n(\mathbf{R}, t)$ is very slow whereas the time required for optical beams to propagate through the atmosphere is very short. Therefore the time dependence in Eq. (2.2.1) can be ignored,

$$n(\mathbf{r}) = 1 + n_1(\mathbf{r}). \tag{2.2.2}$$

At optical frequencies, the refractive index of atmosphere is approximately given by [5]

$$n(\mathbf{r}) = 1 + 77.6 \times 10^{-6} \left(1 + 7.52 \times 10^{-3} \lambda^{-2}\right) \frac{P(\mathbf{r})}{T(\mathbf{r})}, \tag{2.2.3}$$

where $P(\mathbf{r})$ is the atmospheric pressure in millibars, $T(\mathbf{r})$ is the atmospheric temperature in Kelvin, and λ is the optical wavelength in μm. The pressure fluctuations are usually negligible, leaving the temperature fluctuations as the primary factor of the refractive index fluctuations. From Eq. (2.2.3), it can be seen that the magnitude of $n_1(\mathbf{r})$ is several orders of magnitude smaller than n_0. At sea level, its typical value is 3×10^{-4}.

The statistical properties of the refractive index of the atmosphere directly affect

the propagation of optical beams within it. The autocorrelation function of the refractive index fluctuation $n_1(\mathbf{r})$ is defined as [10]

$$\Gamma_n(\mathbf{r}_1, \mathbf{r}_2) = \langle n_1(\mathbf{r}_1) n_1(\mathbf{r}_2) \rangle, \tag{2.2.4}$$

where the angle brackets denote an ensemble average. As turbulent eddies in the inertial subrange are assumed statistically homogeneous and isotropic, its refractive index $n_1(\mathbf{r})$ have the same statistical properties. Here being homogeneous means that the statistical quantity $\Gamma_n(\mathbf{r}_1, \mathbf{r}_2)$ depends on $\Delta\mathbf{r} = \mathbf{r}_1 - \mathbf{r}_2$. By statistical isotropy, $\Gamma_n(\mathbf{r}_1, \mathbf{r}_2)$ is only the function of the scalar distance $\Delta r = |\Delta\mathbf{r}|$ irrespective of the relative orientation between $\mathbf{r}_1$ and $\mathbf{r}_2$. With these properties, Eq. (2.2.4) takes a simple form

$$\Gamma_n(\Delta r) = \langle n_1(\mathbf{r}_1) n_1(\mathbf{r}_1 + \Delta\mathbf{r}) \rangle. \tag{2.2.5}$$

Another important statistical quantity of n_1 is the structure function $D_n(\mathbf{r}_1, \mathbf{r}_1)$ defined as

$$D_n(\mathbf{r}_1, \mathbf{r}_2) = \langle [n_1(\mathbf{r}_1) - n_1(\mathbf{r}_2)]^2 \rangle. \tag{2.2.6}$$

On the assumption of homogeneity and isotropy, it follows that

$$D_n(\Delta r) = 2\left[\Gamma_n(\Delta r) - \Gamma_n(0)\right]. \tag{2.2.7}$$

Under the assumption of statistical homogeneity, the power spectral density (power spectrum) $\Phi_n(\boldsymbol{\kappa})$ of n_1 and its autocorrelation function form a three dimensional

Fourier transform pair,

$$\Phi_n(\boldsymbol{\kappa}) = \frac{1}{(2\pi)^3} \int \Gamma_n(\Delta\mathbf{r}) \exp(-i\boldsymbol{\kappa} \cdot \Delta\mathbf{r}) d^3\Delta r \tag{2.2.8a}$$

$$\Gamma_n(\mathbf{r}) = \int \Phi_n(\boldsymbol{\kappa}) \exp(i\boldsymbol{\kappa} \cdot \Delta\mathbf{r}) d^3\kappa, \tag{2.2.8b}$$

where $\boldsymbol{\kappa}$ is the vector wavenumber and $\kappa = |\boldsymbol{\kappa}|$. Eqs. (2.2.8) can be further simplified by the assumption of statistical isotropy

$$\Phi_n(\kappa) = \frac{1}{2\pi^2\kappa} \int_0^\infty \Gamma_n(\Delta r) \sin(\kappa\Delta r) \Delta r d\Delta r \tag{2.2.9a}$$

$$\Gamma_n(\Delta r) = \frac{4\pi}{\Delta r} \int_0^\infty \Phi_n(\kappa) \sin(\kappa\Delta r) \kappa d\kappa. \tag{2.2.9b}$$

The relation between the structure function $D_n(\Delta r)$ and the power spectral density $\Phi_n(\kappa)$ can also be readily obtained. From Eqs. (2.2.7) and (2.2.9b), it can be shown that

$$D_n(\Delta r) = 8\pi \int_0^\infty \kappa^2 \Phi_n(\kappa) \left[1 - \frac{\sin(\kappa\Delta r)}{\kappa\Delta r}\right] d\kappa. \tag{2.2.10}$$

The expression of $\Phi_n(\kappa)$ in terms of $D_n(\Delta r)$ can also be derived without too much difficulty [5]

$$\Phi_n(\kappa) = \frac{1}{4\pi^2\kappa^2} \int_0^\infty \frac{\sin(\kappa\Delta r)}{\kappa\Delta r} \frac{d}{d\Delta r} \left[(\Delta r)^2 \frac{d}{d\Delta r} D_n(\Delta r)\right] d\Delta r. \tag{2.2.11}$$

From Eq. 2.2.11, the spectral density function $\Phi_n(\kappa)$ can be determined from the knowledge of the structure function $D_n(\Delta r)$. The characterization of turbulence was developed in terms of velocity fluctuations. By dimensional analysis, Kolmogorov first showed that the structure function of wind velocity obeys a 2/3 power law in the inertial subrange [85]. His ideas were later applied to the studies on fluctuations of

passive scalars. The potential temperature Θ is defined as

$$\Theta = T + \alpha_a h, \tag{2.2.12}$$

where T is the atmospheric temperature, α_a is the adiabatic rate of decrease of the temperature and h is height above the Earth's surface. It is considered passive as its fluctuations do not exchange energy with velocity fluctuations. This leads to the same power law relation [86]. From Eq. 2.2.3, it can be shown that the variation of refractive index is proportional to the variation of temperature [5, Chapter 2]

$$\delta n = \frac{79P}{T}\left(\frac{\delta P}{P} - \frac{\delta T}{T}\right) \times 10^{-6}. \tag{2.2.13}$$

As $\delta\Theta = \delta T$ and the pressure fluctuations are negligible, it can be simplified as

$$\delta n = -79P\frac{\delta\Theta}{T^2} \times 10^{-6}. \tag{2.2.14}$$

Eq. (2.2.14) shows that the refractive index fluctuations are also passive and therefore their structure function $D_n(\Delta r)$ also obeys a 2/3 power law in the inertial subrange

$$D_n(\Delta r) = C_n^2(\Delta r)^{2/3} \qquad l_0 < \Delta r < L_0, \tag{2.2.15}$$

where C_n^2 is the refractive index structure constant which characterizes the strength of atmospheric turbulence. Typically, C_n^2 takes the values from 10^{-17} $\mathrm{m}^{-2/3}$ or less to 10^{-13} $\mathrm{m}^{-2/3}$ or more, characterizing the change of atmospheric turbulence strength from weak to strong. In general, C_n^2 is a function of altitude, location and time of day. Its variation with altitude should be taken into account when the propagation path of a beam is slant or vertical. Otherwise it is convenient to assume it is a

constant over a horizontal path. On substituting Eq. (2.2.15) into Eq. (2.2.11) and formally extending the integral limits from $[l_0, L_0]$ to $[0, \infty]$, the following expression is obtained,

$$\Phi_n(\boldsymbol{\kappa}) = 0.033 C_n^2 \kappa^{-11/3}. \tag{2.2.16}$$

Eq. (2.2.16) is the well-known Kolmogorov spectrum of atmospheric turbulence.

The Kolmogorov spectrum [Eq. (2.2.16)] provides a relatively simple mathematical model of atmospheric turbulence and is widely used in theoretical studies. In deriving Eq. (2.2.16), it is assumed that the outer scale L_0 is infinite and the inner scale l_0 is zero. However, under certain circumstances, the effects of outer scale and inner are not negligible. In addition, the singularity at $\kappa = 0$ in Eq. (2.2.16) means that the spectrum is arbitrarily large as $\kappa \to 0$, which is contradictory to the fact that the amount of air masses in the atmosphere is finite. To overcome these defects, the von Karman spectrum is adopted

$$\Phi_n(\boldsymbol{\kappa}) = 0.033 C_n^2 \frac{\exp(-\kappa^2/\kappa_m^2)}{(\kappa^2 + \kappa_0^2)^{11/6}}, \tag{2.2.17}$$

where $\kappa_m = 5.92/l_0$ and $\kappa_0 = 1/L_0$.

Fig. 2.2 illustrates the Kolmogorov spectrum and the von Karman spectrum. It can be seen that the von Karman spectrum reduces to the Kolmogorov spectrum in the inertial subrange. It should be emphasized that both of these two spectrum models are only valid in the inertial subrange where the physical laws governing turbulent flows are well-established. The extension of the von Karman spectrum outside of the inertial subrange is based on mathematical convenience. In the range $\kappa \leq \kappa_0$, the

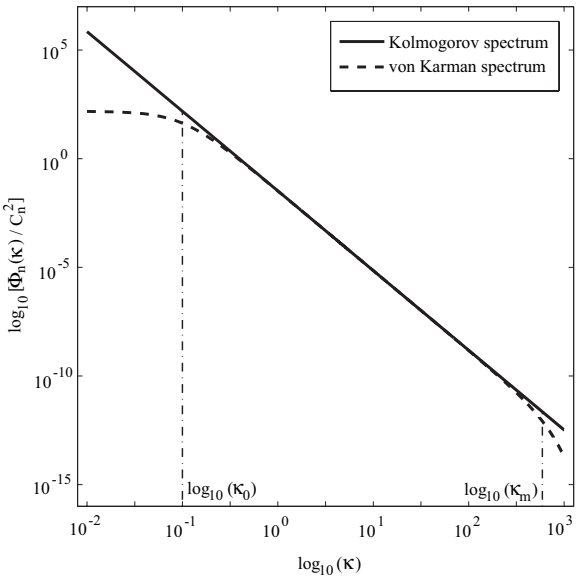

Figure 2.2: Illustration of Kolmogorov spectrum and von Karman spectrum. $L_0 =$ 10 m and $l_0 = 1$ cm.

turbulence spectrum depends on large scale geographic and meteorological conditions. The range $\kappa \geq \kappa_m$ is the dissipation range, where turbulent eddies smaller than inner scale l_0 dissipate their energy as heat by viscous forces. Some research results show that there is a "bump" in the atmospheric temperature fluctuations spectrum at high wavenumber near κ_0 [87, 88]. Since the refractive index of atmosphere obeys the same spectral law as the atmospheric temperature, the bump feature should also appear in the turbulence spectrum and produces a corresponding bump in certain quantities characterizing optical beam propagation in the atmosphere. Hill proposed a numerical spectral model where the bump feature is taken into account [89]. Andrews later developed an analytic approximation to the Hill spectrum which includes an outer scale parameter, now referred to as the modified atmospheric spectrum [90]. However, this dissertation focuses on the general features of optical beam propagation in the atmosphere, which are mainly affected by the turbulent eddies in the inertial

subrange. Therefore, the Kolmogorov spectrum and the von Karman spectrum are used throughout this dissertation.

2.3 Classical Theory of Optical Beam Propagation through Atmospheric Turbulence

The propagation behavior of optical beams in the atmosphere is governed by the wave equation which can be derived from Maxwell's equations. For a medium with arbitrary permittivity ε and magnetic permeability μ, the wave equation has the form [13, Chapter 1]

$$\nabla^2\mathbf{E}(\mathbf{r},t) - \frac{\varepsilon\mu}{c^2}\frac{\partial}{\partial t}\mathbf{E}(\mathbf{r},t) + (\nabla \ln\mu)\times\nabla\times\mathbf{E}(\mathbf{r},t) + \nabla\left[\mathbf{E}(\mathbf{r},t)\cdot\nabla\ln\varepsilon\right] = 0, \quad (2.3.1)$$

where $\mathbf{E}(\mathbf{r},t)$ is the electric field of the wavefield and c is the speed of light in the vacuum. If investigations focus on monochromatic fields, i.e. that

$$\mathbf{E}(\mathbf{r},t) = \mathbf{E}(\mathbf{r})\exp(-i\omega t), \quad (2.3.2)$$

the wave equation (2.3.1) reduces to its monochromatic form

$$\nabla^2\mathbf{E}(\mathbf{r}) + k_0^2\varepsilon\mu\mathbf{E}(\mathbf{r}) + (\nabla\ln\mu)\times\nabla\times\mathbf{E}(\mathbf{r}) + \nabla\left[\mathbf{E}(\mathbf{r})\cdot\nabla\ln\varepsilon\right] = 0, \quad (2.3.3)$$

where $k_0 = \omega/c$ is the wavenumber in the vacuum. The Earth's atmosphere is an inhomogeneous but isotropic medium. Its permittitity ε is a random function of $\mathbf{r}$ and the magnetic permeability μ is assumed to be 1. Therefore the wave equation in the atmosphere has the following form

$$\nabla^2\mathbf{E}(\mathbf{r}) + k_0^2 n^2(\mathbf{r})\mathbf{E}(\mathbf{r}) + 2\nabla\left[\mathbf{E}(\mathbf{r})\cdot\nabla\ln n(\mathbf{r})\right] = 0, \quad (2.3.4)$$

where the relation $\varepsilon = n^2(\mathbf{r})$ is used. The last term of the left hand side of Eq. (2.3.4) is related to the coupling among the orthogonal components of a wavefield, giving rise to the depolarization effects. However, as the wavelength of optical beams is much smaller than the smallest scale of turbulence eddies (the inner scale l_0), it has been shown that the depolarization term is negligible in most turbulence propagation problems [7]. On substituting Eq. (2.2.2) into Eq. (2.3.4) and noting that $n_1(\mathbf{r}) \ll 1$, it simplifies to

$$\nabla^2 \mathbf{E}(\mathbf{r}) + k_0^2 \left[1 + 2n_1(\mathbf{r})\right] \mathbf{E}(\mathbf{r}) = 0. \tag{2.3.5}$$

Due to the symmetry of all three orthogonal components of $\mathbf{E}(\mathbf{r})$, vector equation (2.3.5) can be represented by a scalar equation

$$\nabla^2 U(\mathbf{r}) + k_0^2 \left[1 + 2n_1(\mathbf{r})\right] U(\mathbf{r}) = 0, \tag{2.3.6}$$

where $U(\mathbf{r})$ denotes a transverse component of a wavefield.

Eq. (2.3.6) is the scalar stochastic wave equation which governs the propagation behavior of optical beams in the atmosphere. Due to the random nature of $n_1(\mathbf{r})$, it generally can not be solved in a closed form. Several methods have been developed to solve it under various fluctuation conditions. In the atmosphere, the fluctuation strength of a wavefield can be quantitatively estimated through the so-called *Rytov variance*

$$\sigma_1^2 = 1.23 C_n^2 k_0^{7/6} L^{11/6}, \tag{2.3.7}$$

where L is the propagation distance. In general, weak fluctuations are defined as $\sigma_1^2 \ll 1$ and strong fluctuations are in the regime when $\sigma_1^2 \gg 1$. Under weak fluctuation

conditions, Eq. (2.3.6) can be solved by perturbation theories, including the Born approximation and the Rytov approximation. The analytic theories under strong fluctuation conditions are rather complicated and mathematically challenging. In this dissertation, the extended Huygens-Fresnel principle method is applied to this circumstance.

2.3.1 Born Approximation[1]

By the Born approximation method, the wavefield is modified by adding perturbation terms to the unperturbed wavefield

$$U(\mathbf{r}) = U_0(\mathbf{r}) + U_1(\mathbf{r}) + U_2(\mathbf{r}) + \cdots, \tag{2.3.8}$$

where $U_0(\mathbf{r})$ denotes the unperturbed wavefield in the absence of turbulence, $U_1(\mathbf{r})$ and $U_2(\mathbf{r})$ are the first and second order perturbation terms caused by turbulence. Each term $U_m(\mathbf{r})$ is on the order of smallness $(n_1)^m$. Generally, $U_0(\mathbf{r}) \gg U_1(\mathbf{r}) \gg U_2(\mathbf{r})$. On substituting Eq. (2.3.8) into Eq. (2.3.6) and equating terms of the same order in n_1, the following series of equations are obtained

$$\nabla^2 U_0(\mathbf{r}) + k_0^2 U_0(\mathbf{r}) = 0 \tag{2.3.9a}$$

$$\nabla^2 U_1(\mathbf{r}) + k_0^2 U_1(\mathbf{r}) = -2k_0^2 n_1(\mathbf{r}) U_0(\mathbf{r}) \tag{2.3.9b}$$

$$\nabla^2 U_2(\mathbf{r}) + k_0^2 U_2(\mathbf{r}) = -2k_0^2 n_1(\mathbf{r}) U_1(\mathbf{r}). \tag{2.3.9c}$$

[1]Now the Born approximation is not used in the studies of wave propagation in weak turbulence due to its limitations (see the end of Sec. 2.3.2). However, the formulae of the Rytov approximation are derived based on the Born approximation. It is introduced here for the purpose of illustration.

From Eqs. (2.3.9), it can be seen that the perturbation terms are the solutions of inhomogeneous Helmholtz equations, where the lower order perturbation terms serve (combined with $n_1(\mathbf{r})$) as the source terms.

Given the form of the unperturbed term $U_0(\mathbf{r})$, $U_1(\mathbf{r})$ can be obtained by the Green's function method [13]

$$U_1(\mathbf{r}) = \int G(\mathbf{r}, \mathbf{r}') \left[2k_0^2 n_1(\mathbf{r}') U_0(\mathbf{r}')\right] d^3r', \tag{2.3.10}$$

where $G(\mathbf{r}, \mathbf{r}')$ is the free space Green's function

$$G(\mathbf{r}, \mathbf{r}') = \frac{1}{4\pi|\mathbf{r} - \mathbf{r}'|} \exp\left(ik_0|\mathbf{r} - \mathbf{r}'|\right). \tag{2.3.11}$$

Eq. (2.3.10) can be further simplified by the paraxial approximation. Considering the fact that the wavelength of at optical frequencies is very small compared to the sizes of turbulent eddies, the wavefield is forward scattered in a small cone about the original propagation direction. The maximum scattering angle is of the magnitude of $\lambda/l_0 \sim 10^{-4}$ radians. Under this condition, the free space Green's function can be approximated by its paraxial form

$$G(\mathbf{r}, \mathbf{r}') \approx \frac{1}{4\pi(z - z')} \exp\left[ik_0(z - z') + \frac{ik_0|\boldsymbol{\rho} - \boldsymbol{\rho}'|^2}{2(z - z')}\right]. \tag{2.3.12}$$

where $\mathbf{r} = (\boldsymbol{\rho}, z)$. Accordingly, the first order perturbation term $U_1(\mathbf{r})$ takes the following form

$$U_1(\boldsymbol{\rho}, z) = \frac{k_0^2}{2\pi z} \int_0^z dz' \int d^2\rho' \exp\left[ik_0(z - z') + \frac{ik_0|\boldsymbol{\rho} - \boldsymbol{\rho}'|^2}{2(z - z')}\right] U_0(\boldsymbol{\rho}', z') \frac{n_1(\boldsymbol{\rho}', z')}{z - z'}, \tag{2.3.13}$$

where the wavefield is assumed to propagate along the z axis. The second order perturbation term $U_2(\mathbf{r})$ can be obtained by the similar manner

$$U_2(\boldsymbol{\rho}, z) = \frac{k_0^2}{2\pi z} \int_0^z dz' \int d^2\rho' \exp\left[ik_0(z-z') + \frac{ik_0|\boldsymbol{\rho}-\boldsymbol{\rho}'|^2}{2(z-z')}\right] U_1(\boldsymbol{\rho}', z') \frac{n_1(\boldsymbol{\rho}', z')}{z-z'}. \tag{2.3.14}$$

2.3.2 Rytov Approximation

Unlike the Born approximation, the Rytov approximation assumes the perturbation terms are multiplicative to the unperturbed wavefield

$$U(\mathbf{r}) = U_0(\mathbf{r}) \exp\left[\psi(\mathbf{r})\right], \tag{2.3.15}$$

where $\psi(\mathbf{r}) = \psi_1(\mathbf{r}) + \psi_2(\mathbf{r}) + \cdots$ is a complex phase perturbation of the unperturbed term $U_0(\mathbf{r})$. $\psi_1(\mathbf{r})$ and $\psi_2(\mathbf{r})$ are the corresponding first and the second order perturbation terms. The expressions for $\psi_1(\mathbf{r})$ and $\psi_2(\mathbf{r})$ can be obtained from the results of the Born approximations calculated in the previous subsection.

To begin with, the normalized Born approximations are defined as

$$\phi_m(\boldsymbol{\rho}, z) = \frac{U_m(\boldsymbol{\rho}, z)}{U_0(\boldsymbol{\rho}, z)} \qquad m = 1, 2, ... \tag{2.3.16}$$

By the assumption of equality between the first order Rytov and Born approximations

$$U_0(\boldsymbol{\rho}, z) \exp[\psi_1(\boldsymbol{\rho}, z)] = U_0(\boldsymbol{\rho}, z)[1 + \phi_1(\boldsymbol{\rho}, z)], \tag{2.3.17}$$

it can be shown that, after some calculations,

$$\begin{aligned} \psi_1(\boldsymbol{\rho}, z) &= \ln[1 + \phi_1(\boldsymbol{\rho}, z)] \\ &\approx \phi_1(\boldsymbol{\rho}, z), \qquad |\phi_1(\boldsymbol{\rho}, z)| \ll 1. \end{aligned} \tag{2.3.18}$$

From the definition of $\phi_1(\boldsymbol{\rho}, z)$ and Eq. (2.3.13), the first order Rytov approximation term $\psi_1(\boldsymbol{\rho}, z)$ is given by

$$\psi_1(\boldsymbol{\rho}, z) = \frac{k_0^2}{2\pi z} \int_0^z dz' \int d^2\rho' \exp\left[ik_0(z - z') + \frac{ik_0|\boldsymbol{\rho} - \boldsymbol{\rho}'|^2}{2(z - z')}\right] \frac{U_0(\boldsymbol{\rho}', z')}{U_0(\boldsymbol{\rho}, z)} \frac{n_1(\boldsymbol{\rho}', z')}{z - z'}. \tag{2.3.19}$$

The second order Rytov approximation term $\psi_2(\boldsymbol{\rho}, z)$ can be obtained in a similar manner. By equating the Born and Rytov approximations up to the second order, the following expressions are obtained

$$\begin{aligned} U_0(\boldsymbol{\rho}, z) \exp[\psi_1(\boldsymbol{\rho}, z) + \psi_2(\boldsymbol{\rho}, z)] &= U_0(\boldsymbol{\rho}, z)[1 + \phi_1(\boldsymbol{\rho}, z) + \phi_2(\boldsymbol{\rho}, z)] \\ \psi_1(\boldsymbol{\rho}, z) + \psi_2(\boldsymbol{\rho}, z) &= \ln[1 + \phi_1(\boldsymbol{\rho}, z) + \phi_2(\boldsymbol{\rho}, z)]. \end{aligned} \tag{2.3.20}$$

By further using the Maclaurin series of the right hand side and retaining up to the second order due to $|\phi_1(\boldsymbol{\rho}, z)| \ll 1$ and $|\phi_2(\boldsymbol{\rho}, z)| \ll 1$, it can be shown that

$$\psi_1(\boldsymbol{\rho}, z) + \psi_2(\boldsymbol{\rho}, z) \approx \phi_1(\boldsymbol{\rho}, z) + \phi_2(\boldsymbol{\rho}, z) - \frac{1}{2}\phi_1^2(\boldsymbol{\rho}, z). \tag{2.3.21}$$

With the relation $\psi_1(\boldsymbol{\rho}, z) = \phi_1(\boldsymbol{\rho}, z)$, the second order Rytov approximation term $\psi_1(\boldsymbol{\rho}, z)$ is given by

$$\psi_2(\boldsymbol{\rho}, z) = \phi_2(\boldsymbol{\rho}, z) - \frac{1}{2}\phi_1^2(\boldsymbol{\rho}, z), \tag{2.3.22}$$

where the second order normalized Born approximation term $\phi_2(\boldsymbol{\rho}, z)$ can be obtained

from Eq. (2.3.14)

$$\begin{aligned}\phi_2(\boldsymbol{\rho}, z) &= \frac{k_0^2}{2\pi z}\int_0^z dz' \int d^2\rho' \exp\left[ik_0(z-z') + \frac{ik_0|\boldsymbol{\rho}-\boldsymbol{\rho}'|^2}{2(z-z')}\right] \\ &\times \frac{U_0(\boldsymbol{\rho}', z')}{U_0(\boldsymbol{\rho}, z)} \frac{\phi_1(\boldsymbol{\rho}', z') n_1(\boldsymbol{\rho}', z')}{z-z'}. \end{aligned} \tag{2.3.23}$$

The propagation properties of optical beams in the atmosphere are investigated through the statistical moments of the propagating wavefield. Of most interest are the first, second and fourth statistical moments, since they are measurable quantities by experiments. It has been shown that under weak fluctuation conditions these statistical moments can be well characterized by the Rytov approximations up to the second order term [91]. The first order moments describes the mean wavefield

$$\langle U(\mathbf{r})\rangle = U_0(\mathbf{r})\langle \exp[\psi(\mathbf{r})]\rangle. \tag{2.3.24}$$

The second order moment is defined as

$$\begin{aligned}\Gamma_2(\mathbf{r}_1, \mathbf{r}_2) &= \langle U(\mathbf{r}_1) U^*(\mathbf{r}_2)\rangle \\ &= U_0(\mathbf{r}_1) {U_0}^*(\mathbf{r}_2) \langle \exp[\psi(\mathbf{r}_1) + \psi^*(\mathbf{r}_2)]\rangle. \end{aligned} \tag{2.3.25}$$

Since it has the same form as the cross-spectral density [Eq. 2.1.5], the coherence properties of the propagating beam in the atmosphere can be studied through Eq. (2.3.25). When $\mathbf{r}_1 = \mathbf{r}_2 = \mathbf{r}$, Eq. (2.3.25) is the expression for the average intensity

$$\langle I(\mathbf{r})\rangle = \Gamma_2(\mathbf{r}, \mathbf{r}), \tag{2.3.26}$$

from which the turbulence-induced beam spreading can be evaluated. The intensity

fluctuations of a wavefield are described by the general fourth order moment

$$\begin{aligned}\Gamma_4(\mathbf{r}_1,\mathbf{r}_2,\mathbf{r}_3,\mathbf{r}_4) &= \langle U(\mathbf{r}_1)U^*(\mathbf{r}_2)U(\mathbf{r}_3)U^*(\mathbf{r}_4)\rangle \\ &= U_0(\mathbf{r}_1){U_0}^*(\mathbf{r}_2)U_0(\mathbf{r}_3){U_0}^*(\mathbf{r}_4) \\ &\times \langle\exp[\psi(\mathbf{r}_1)+\psi^*(\mathbf{r}_2)+\psi(\mathbf{r}_3)+\psi^*(\mathbf{r}_4)]\rangle. \qquad (2.3.27)\end{aligned}$$

The strength of intensity fluctuations at $\mathbf{r}$ can be quantitatively characterized by the scintillation index $\sigma^2(\mathbf{r})$. It can be evaluated through Eq. (2.3.27) with $\mathbf{r}_1 = \mathbf{r}_2 = \mathbf{r}_3 = \mathbf{r}_4 = \mathbf{r}$

$$\begin{aligned}\sigma^2(\mathbf{r}) &= \frac{\langle I^2(\mathbf{r})\rangle}{\langle I(\mathbf{r})\rangle^2} - 1 \\ &= \frac{\Gamma_4(\mathbf{r},\mathbf{r},\mathbf{r},\mathbf{r})}{\Gamma_2(\mathbf{r},\mathbf{r})\Gamma_2(\mathbf{r},\mathbf{r})} - 1. \qquad (2.3.28)\end{aligned}$$

The ensemble averages in Eqs. (2.3.24), (2.3.25), and (2.3.27) can be calculated by the method of cumulants [92]

$$\langle\exp(\psi)\rangle = \exp\left[\langle\psi\rangle + \frac{1}{2}\left(\langle\psi^2\rangle - \langle\psi\rangle^2\right)\right]. \qquad (2.3.29)$$

On substituting $\psi_m = \psi_{1m} + \psi_{2m}, m = 1,2,3,4$ and retaining only terms up to the second order, Eqs. (2.3.24), (2.3.25), and (2.3.27) are simplified as the following, respectively,

$$\langle U(\mathbf{r})\rangle = U_0(\mathbf{r})\langle\exp[E_1(\mathbf{r})]\rangle, \qquad (2.3.30)$$

$$\Gamma_2(\mathbf{r}_1,\mathbf{r}_2) = U_0(\mathbf{r}_1){U_0}^*(\mathbf{r}_2)\exp[E_1(\mathbf{r}_1)+E_1^*(\mathbf{r}_2)+E_2(\mathbf{r}_1,\mathbf{r}_2)], \qquad (2.3.31)$$

$$\Gamma_4(\mathbf{r}_1,\mathbf{r}_2,\mathbf{r}_3,\mathbf{r}_4) = \Gamma_2(\mathbf{r}_1,\mathbf{r}_2)\Gamma_2(\mathbf{r}_3,\mathbf{r}_4)\exp[E_2(\mathbf{r}_1,\mathbf{r}_4)+E_2(\mathbf{r}_3,\mathbf{r}_2)]$$
$$\times \exp[E_3(\mathbf{r}_1,\mathbf{r}_3)+E_3^*(\mathbf{r}_2,\mathbf{r}_4)], \quad (2.3.32)$$

where

$$E_1(\mathbf{r}) = \langle\psi_2(\mathbf{r})\rangle + \frac{1}{2}\langle\psi_1^2(\mathbf{r})\rangle, \quad (2.3.33)$$

$$E_2(\mathbf{r}_1,\mathbf{r}_2) = \langle\psi_1(\mathbf{r}_1)\psi_1^*(\mathbf{r}_2)\rangle, \quad (2.3.34)$$

$$E_3(\mathbf{r}_1,\mathbf{r}_2) = \langle\psi_1(\mathbf{r}_1)\psi_1(\mathbf{r}_2)\rangle. \quad (2.3.35)$$

For a given unperturbed optical beam $U_0(\mathbf{r})$ and a specific turbulence spectrum model, the statistical moments of the propagated beam [Eqs. (2.3.30), (2.3.31), and (2.3.32)] can be evaluated with the expressions of $\psi_1(\mathbf{r})$ and $\psi_2(\mathbf{r})$ given in Eqs (2.3.19), (2.3.22), and (2.3.23).

Because the Rytov approximation assumes multiplicative perturbations, it has been shown that this method leads to the lognormal distribution model of the probability density function of the irradiance [10]. This model agrees well with the experimental data obatined in the weak fluctuation regime. Therefore the Rytov approximation method is the standard method used in the regime where the Rytov variance σ_1^2 is low.

2.3.3 The Extended Huygens-Fresnel Principle Method

The Rytov approximation method yields the most fruitful results in the weak fluctuation regime. When the fluctuations of optical beams become strong (high σ_1^2), more sophisticated methods must be employed. One relatively straightforward approach is the use of the extended Huygens-Fresnel principle, which expresses the

propagating wavefield at a receiver plane $z = L$ in the atmosphere as follows

$$U(\boldsymbol{\rho}, L) = -\frac{ik_0}{2\pi L}\exp(ik_0 L)\int d^2\rho' U_0(\boldsymbol{\rho}', 0)\exp\left[\frac{ik_0|\boldsymbol{\rho}-\boldsymbol{\rho}'|}{2L} + \varphi(\boldsymbol{\rho}, \boldsymbol{\rho}')\right], \quad (2.3.36)$$

where $U_0(\boldsymbol{\rho}', 0)$ is the incident wavefield at the transmitter plane $z = 0$, $\varphi(\boldsymbol{\rho}, \boldsymbol{\rho}') = \varphi_1(\boldsymbol{\rho}, \boldsymbol{\rho}') + \varphi_2(\boldsymbol{\rho}, \boldsymbol{\rho}')$ is the random part of the complex phase of a spherical wave propagating in the atmosphere, and $\varphi_1(\boldsymbol{\rho}, \boldsymbol{\rho}')$ and $\varphi_2(\boldsymbol{\rho}, \boldsymbol{\rho}')$ are the corresponding first and second order terms.

By Eq. (2.3.36), the mean field $\langle U(\boldsymbol{\rho}, L)\rangle$, the mutual coherence function $\Gamma_2(\boldsymbol{\rho}_1, \boldsymbol{\rho}_2, L)$, and the general fourth order moment $\Gamma_4(\boldsymbol{\rho}_1, \boldsymbol{\rho}_2, \boldsymbol{\rho}_3, \boldsymbol{\rho}_4, L)$ are obtained,

$$\langle U(\boldsymbol{\rho}, L)\rangle = -\frac{ik_0}{2\pi L}\exp(ik_0 L)\int d^2\rho' U_0(\boldsymbol{\rho}', 0)\exp\left[\frac{ik_0|\boldsymbol{\rho}-\boldsymbol{\rho}'|^2}{2L}\right]\langle\exp\left[\varphi(\boldsymbol{\rho}, \boldsymbol{\rho}')\right]\rangle, \quad (2.3.37)$$

$$\begin{aligned}\Gamma_2(\boldsymbol{\rho}_1, \boldsymbol{\rho}_2, L) &= \langle U(\boldsymbol{\rho}_1, L)U^*(\boldsymbol{\rho}_2, L)\rangle \\ &= \left(\frac{k_0}{2\pi L}\right)^2\int d^2\rho_1'\int d^2\rho_2' U_0(\boldsymbol{\rho}_1', 0)U_0^*(\boldsymbol{\rho}_2', 0)\exp\left[\frac{ik_0|\boldsymbol{\rho}_1-\boldsymbol{\rho}_1'|^2}{2L}\right] \\ &\times \exp\left[-\frac{ik_0|\boldsymbol{\rho}_2-\boldsymbol{\rho}_2'|^2}{2L}\right]\langle\exp\left[\varphi(\boldsymbol{\rho}_1, \boldsymbol{\rho}_1') + \varphi^*(\boldsymbol{\rho}_2, \boldsymbol{\rho}_2')\right]\rangle, \quad (2.3.38)\end{aligned}$$

$$\begin{aligned}\Gamma_4(\boldsymbol{\rho}_1, \boldsymbol{\rho}_2, \boldsymbol{\rho}_3, \boldsymbol{\rho}_4, L) &= \langle U(\boldsymbol{\rho}_1, L)U^*(\boldsymbol{\rho}_2, L)U(\boldsymbol{\rho}_3, L)U^*(\boldsymbol{\rho}_4, L)\rangle \\ &= \left(\frac{k_0}{2\pi L}\right)^4\int d^2\rho_1'\int d^2\rho_2'\int d^2\rho_3'\int d^2\rho_4' \\ &\times U_0(\boldsymbol{\rho}_1', 0)U_0^*(\boldsymbol{\rho}_2', 0)U_0(\boldsymbol{\rho}_3', 0)U_0^*(\boldsymbol{\rho}_4', 0) \\ &\times \langle\exp\left[\varphi(\boldsymbol{\rho}_1, \boldsymbol{\rho}_1') + \varphi^*(\boldsymbol{\rho}_2, \boldsymbol{\rho}_2')\right] + \varphi(\boldsymbol{\rho}_3, \boldsymbol{\rho}_3') + \varphi^*(\boldsymbol{\rho}_4, \boldsymbol{\rho}_4')\rangle \\ &\times \exp\left[\frac{ik_0|\boldsymbol{\rho}_1-\boldsymbol{\rho}_1'|^2}{2L}\right]\exp\left[-\frac{ik_0|\boldsymbol{\rho}_2-\boldsymbol{\rho}_2'|^2}{2L}\right] \\ &\times \exp\left[\frac{ik_0|\boldsymbol{\rho}_3-\boldsymbol{\rho}_3'|^2}{2L}\right]\exp\left[-\frac{ik_0|\boldsymbol{\rho}_4-\boldsymbol{\rho}_4'|^2}{2L}\right]. \quad (2.3.39)\end{aligned}$$

The ensemble averages in Eqs. (2.3.37), (2.3.38), and (2.3.39) can be calculated with the method of cumulants [Eq. (2.3.29)]. After some calculations, the following expressions are obtained

$$\langle \exp\left[\varphi(\boldsymbol{\rho},\boldsymbol{\rho}')\right]\rangle = \exp\left[E_1(\boldsymbol{\rho};\boldsymbol{\rho}')\right], \tag{2.3.40}$$

$$\langle \exp\left[\varphi(\boldsymbol{\rho}_1,\boldsymbol{\rho}_1')+\varphi^*(\boldsymbol{\rho}_2,\boldsymbol{\rho}_2')\right]\rangle = \exp\left[E_1(\boldsymbol{\rho}_1;\boldsymbol{\rho}_1')+E_1^*(\boldsymbol{\rho}_2;\boldsymbol{\rho}_2')+E_2(\boldsymbol{\rho}_1,\boldsymbol{\rho}_2;\boldsymbol{\rho}_1',\boldsymbol{\rho}_2')\right], \tag{2.3.41}$$

$$\begin{aligned}
&\langle \exp\left[\varphi(\boldsymbol{\rho}_1,\boldsymbol{\rho}_1')+\varphi^*(\boldsymbol{\rho}_2,\boldsymbol{\rho}_2')+\varphi(\boldsymbol{\rho}_3,\boldsymbol{\rho}_3')+\varphi^*(\boldsymbol{\rho}_4,\boldsymbol{\rho}_4')\right]\rangle \\
&= \exp\left[E_1(\boldsymbol{\rho}_1;\boldsymbol{\rho}_1')+E_1^*(\boldsymbol{\rho}_2;\boldsymbol{\rho}_2')+E_1(\boldsymbol{\rho}_3;\boldsymbol{\rho}_3')+E_1^*(\boldsymbol{\rho}_4;\boldsymbol{\rho}_4')\right] \\
&\times \exp\left[E_2(\boldsymbol{\rho}_1,\boldsymbol{\rho}_2;\boldsymbol{\rho}_1',\boldsymbol{\rho}_2')+E_2(\boldsymbol{\rho}_1,\boldsymbol{\rho}_4;\boldsymbol{\rho}_1',\boldsymbol{\rho}_4')\right] \\
&\times \exp\left[E_2(\boldsymbol{\rho}_3,\boldsymbol{\rho}_2;\boldsymbol{\rho}_3',\boldsymbol{\rho}_2')+E_2(\boldsymbol{\rho}_3,\boldsymbol{\rho}_4;\boldsymbol{\rho}_3',\boldsymbol{\rho}_4')\right] \\
&\times \exp\left[E_3(\boldsymbol{\rho}_1,\boldsymbol{\rho}_3;\boldsymbol{\rho}_1',\boldsymbol{\rho}_3')+E_3^*(\boldsymbol{\rho}_2,\boldsymbol{\rho}_4;\boldsymbol{\rho}_2',\boldsymbol{\rho}_4')\right],
\end{aligned} \tag{2.3.42}$$

where

$$E_1(\boldsymbol{\rho};\boldsymbol{\rho}') = \langle\varphi_2(\boldsymbol{\rho},\boldsymbol{\rho}')\rangle + \frac{1}{2}\langle\varphi_1^2(\boldsymbol{\rho},\boldsymbol{\rho}')\rangle, \tag{2.3.43}$$

$$E_2(\boldsymbol{\rho}_1,\boldsymbol{\rho}_2;\boldsymbol{\rho}_1',\boldsymbol{\rho}_2') = \langle\varphi_1(\boldsymbol{\rho}_1,\boldsymbol{\rho}_1')\varphi_1^*(\boldsymbol{\rho}_2,\boldsymbol{\rho}_2')\rangle, \tag{2.3.44}$$

$$E_3(\boldsymbol{\rho}_1,\boldsymbol{\rho}_2;\boldsymbol{\rho}_1',\boldsymbol{\rho}_2') = \langle\varphi_1(\boldsymbol{\rho}_1,\boldsymbol{\rho}_1')\varphi_1(\boldsymbol{\rho}_2,\boldsymbol{\rho}_2')\rangle. \tag{2.3.45}$$

When the turbulence is statistically homogeneous and isotropic, quantities E_1, E_2, and E_3 are respectively given by [93]

$$E_1(\boldsymbol{\rho};\boldsymbol{\rho}') = -2\pi^2 k_0^2 L\int_0^\infty \kappa\Phi_n(\kappa)d\kappa, \tag{2.3.46}$$

$$E_2(\boldsymbol{\rho}_1, \boldsymbol{\rho}_1'; \boldsymbol{\rho}_2, \boldsymbol{\rho}_2') = -4\pi^2 k_0^2 L \int_0^1 d\xi \int_0^\infty d\kappa \kappa \Phi_n(\kappa) J_0[\kappa|(1-\xi)\mathbf{p} + \xi\mathbf{p}'|], \quad (2.3.47)$$

$$\begin{aligned} E_3(\boldsymbol{\rho}_1, \boldsymbol{\rho}_1'; \boldsymbol{\rho}_2, \boldsymbol{\rho}_2') &= -4\pi^2 k_0^2 L \int_0^1 d\xi \int_0^\infty d\kappa \exp\left[-\frac{iL\kappa^2}{k_0}\xi(1-\xi)\right] \\ &\times \kappa \Phi_n(\kappa) J_0[\kappa|(1-\xi)\mathbf{p} + \xi\mathbf{p}'|], \end{aligned} \quad (2.3.48)$$

where J_0 is the zero order Bessel function of the first kind, $\mathbf{p} = \boldsymbol{\rho}_1 - \boldsymbol{\rho}_2$, and $\mathbf{p}' = \boldsymbol{\rho}_1' - \boldsymbol{\rho}_2'$.

The extended Huygens-Fresnel principle method is applicable under any fluctuation conditions for the purpose of calculating the second order field moments. When turbulence is homogeneous, the ensemble average $\langle \exp[\varphi(\boldsymbol{\rho}_1, \boldsymbol{\rho}_1') + \varphi^*(\boldsymbol{\rho}_2, \boldsymbol{\rho}_2')]\rangle$ in Eq. (2.3.38) can be approximated by [24]

$$\langle \exp[\varphi(\boldsymbol{\rho}_1, \boldsymbol{\rho}_1') + \varphi^*(\boldsymbol{\rho}_2, \boldsymbol{\rho}_2')]\rangle \approx \exp\left(-\frac{|\mathbf{p}|^2 + \mathbf{p}\cdot\mathbf{p}' + |\mathbf{p}'|^2}{\rho_0^2}\right), \quad (2.3.49)$$

where $\rho_0 = (0.55 C_n^2 k^2 L)^{-3/5}$ is the coherence length of a spherical wave propagating in the atmosphere. Eq. (2.3.49) is the well-known quadratic approximation of the turbulence term. Although it has certain limits [94], it gives a good approximation of the second order statistical properties of fields in turbulence under many circumstances. Combined with this approximation, the extended Huygens-Fresnel principle method has been widely used in the studies of the second order statistical properties of optical beams propagating through the atmosphere.

2.4 Numerical Simulation of Optical Beam Propagation in Atmospheric Turbulence

In general, a theoretical investigation of optical beam propagation in the atmosphere is complicated and mathematically challenging. So far, there is no universal theoretical model applicable under any turbulence conditions. Even in the weak turbulence regime where the theoretical methods are relatively well developed, analytic solutions are rare. From Sec. 2.3, it can be found that investigations of beam scintillation by the extended Huygens-Fresnel principle involves the evaluation of an eight-fold integral. Exact solutions only exist for a few beam types, and do not include most special classes considered here. On the contrary, numerical simulations are relatively straightforward. By simulating beam propagation through the atmosphere and analyzing the corresponding wavefield on the receiver plane, the atmospheric propagation properties of such a beam can be obtained.

A typical numerical simulation method for optical beam propagation in atmospheric turbulence is the so-called multiple random phase screen method [33]. As shown in Fig. 2.3, the atmosphere, an extended random medium, is divided into a collection of two dimensional random phase screens whose mutual separation is Δz. Each phase screen imposes a random phase modulation into the incident wavefield and the propagation between two adjacent phase screens is in free space. The propagation between the nth at plane z_n and the $n+1$th at plane $z_{n+1} = z_n + \Delta z$ is simulated by the following procedure

$$U(\boldsymbol{\rho}, z_n^+) = U(\boldsymbol{\rho}, z_n^-) \exp\left[i\theta(\boldsymbol{\rho}, z_n)\right], \tag{2.4.1a}$$

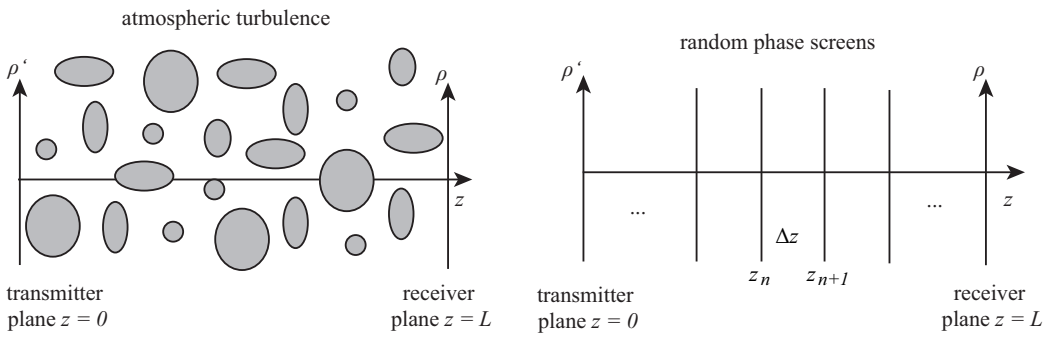

Figure 2.3: Illustration of multiple random phase screen method.

$$\mathscr{F}\left[U(\boldsymbol{\rho}, z_{n+1}^{-})\right] = \mathscr{F}\left[U(\boldsymbol{\rho}, z_{n}^{+})\right] H(\mathbf{f}), \tag{2.4.1b}$$

Eq. (2.4.1a) describes the phase modulation $\theta(\boldsymbol{\rho}, z_n)$ introduced by the nth phase screen, where $U(\boldsymbol{\rho}, z_n^{-})$ is the wavefield incident on the phase screen and $U(\boldsymbol{\rho}, z_n^{+})$ is the corresponding wavefield emerging from the phase screen. The free space propagation between these two phase screens is simulated by the Fourier transfrom method [Eq. (2.4.1b)]. $\mathscr{F}$ denotes Fourier transform. $H(\mathbf{f})$ is the transfer function of propagation in free space [95] and $\mathbf{f}$ is the corresponding two dimensional vector in the spatial frequency domain. Under the paraxial approximation, $H(\mathbf{f})$ takes the following form [95]

$$H(\mathbf{f}) = \exp(ik_0\Delta z)\exp\left(-i\pi\lambda_0\Delta z f^2\right), \tag{2.4.2}$$

where λ_0 is the vacuum wavelength. For the propagation of an incident wavefield $U(\boldsymbol{\rho}, z = 0)$ from the transmitter plane $z = 0$ to the receiver plane $z = L$, it can be simulated by repeating the above procedure for all screens until the wavefield reaches the receiver plane $z = L$.

A crucial aspect of numerical simulation is to generate random phase screens with appropriate statistical properties of the atmosphere. Turbulence is generally assumed

to be spatially uncorrelated along propagation direction, namely δ correlation. By this assumption, the power spectral density function of phase screen Φ_θ takes the following form [33]

$$\Phi_\theta(\boldsymbol{\kappa}_\perp, \Delta z) = 2\pi k_0^2 \Delta z \Phi_n(\boldsymbol{\kappa}_\perp, \kappa_z = 0), \tag{2.4.3}$$

where $\boldsymbol{\kappa}_\perp = (\kappa_x, \kappa_y)$. Random phase screens can be generated by filtering white Gaussian noise with Eq. (2.4.3),

$$\theta_1(x,y) + i\theta_2(x,y) = \mathscr{F}^{-1}\left\{ [a(\kappa_x,\kappa_y) + ib(\kappa_x,\kappa_y)] \left[\Phi_\theta(\kappa_x,\kappa_y,\Delta z)\right]^{-1/2} \right\}, \tag{2.4.4}$$

where $a(\kappa_x, \kappa_y)$ and $b(\kappa_x, \kappa_y)$ are two mutually independent pseudo-random variables in the spatial frequency domain, which satisfy the normal distribution. Upon performing the inverse Fourier transform $\mathscr{F}^{-1}$, two uncorrelated phase screens $\theta_1(x, y)$ and $\theta_2(x, y)$ are generated. A example of a phase screen is illustrated in Fig. 2.4 where the von Karman spectrum is used.

Besides phase screens, a successful numerical simulation of beam propagation in the atmosphere also depends on appropriate selection of the phase screen separation Δz. To correctly model an extended random medium, the intensity fluctuations produced over the distance Δz between two consecutive phase screens should be weak. Two quantitative criteria have been proposed to meet this requirement [33],

$$\sigma^2(\Delta z) < 0.1, \tag{2.4.5a}$$

$$\sigma^2(\Delta z) < 0.1\sigma^2(L) \qquad \text{if } \sigma^2(L) < 0.1, \tag{2.4.5b}$$

where σ^2 denotes the scintillation index. Eq. (2.4.5a) generally requires that the

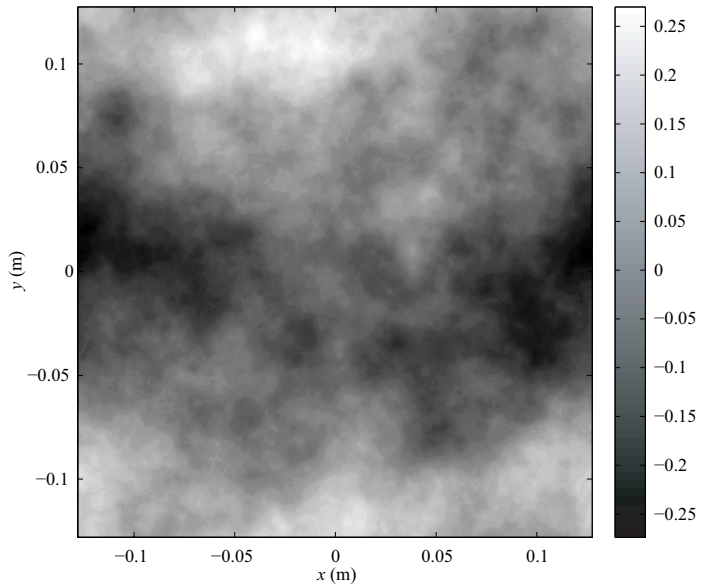

Figure 2.4: Example of random phase screen. von Karman spectrum is used, where $L_0 = 10$ m, $l_0 = 1$ mm, $\Delta z = 200$ m, and $\lambda = 1.55\,\mu$m. The unit of the scale bar is radian.

intensity fluctuations should be weak over the interscreen distance Δz. If the intensity fluctuations over the whole propagation distance L are weak, the second criterion [Eq. (2.4.5b)] should be followed, which states that the interscreen intensity fluctuations should be less than 10% of the total scintillation. By following Eq. (2.4.5), the minimum number of phase screens can be determined for given beam and propagation parameters. An example of the simulated on-axis scintillation index of a Gaussian beam propagating in turbulence is shown in Fig. 2.5. The agreement between the simulated data and the theoretical result developed in Ref. [84] is observed.

It is worth mentioning that the phase screen generation method [Eq. (2.4.4)] is based on the Fourier transform (FT), where the turbulence spectrum is discretely sampled. Due to the limit range of sampling, the lower spatial frequency range of the turbulence spectrum is undersampled and the corresponding phase screens can not

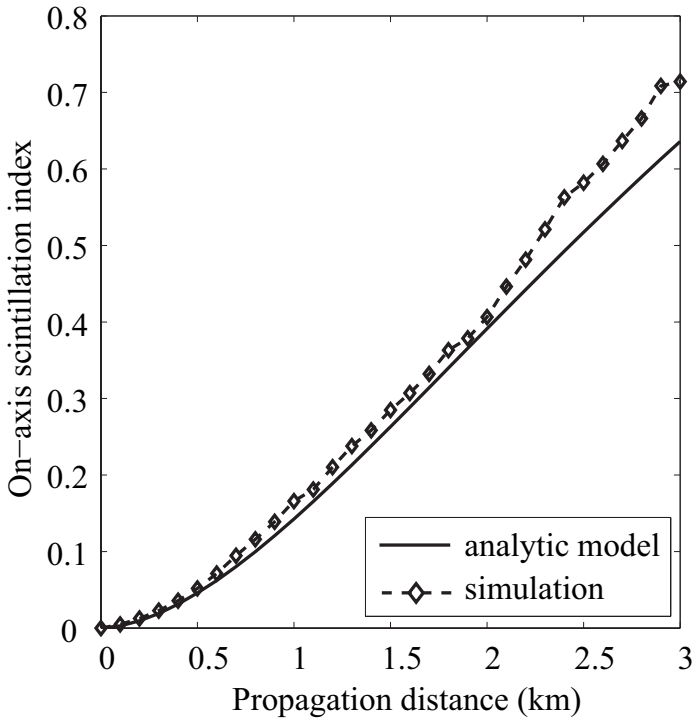

Figure 2.5: On-axis scintillation index of a Gaussian beam propagating in turbulence. The wavelength is taken to be $\lambda = 1.55\,\mu$m and the width of the beam is taken to be $w_0 = 0.05$ m. The turbulence strength parameter is $C_n^2 = 10^{-14}$ m$^{-2/3}$ and the phase screen separation is 100 m.

accurately represent low spatial frequency effects such as tilting. In order to overcome this defect, subharmonic screen techniques have been proposed [35, 36]. However, it has been shown that the FT-based method is accurate for the study of the second order propagation properties of beam propagation in the atmosphere [96]. When the beam intensity fluctuations are weak to moderate, it can also produce relatively accurate results of the scintillation properties of optical beams. Considering the relative high efficiency compared to the subharmonic screen method, the FT-based method is used in this dissertation.

CHAPTER 3: SCINTILLATION REDUCTION BY INCOHERENT BEAM ARRAYS

Scintillation is the name given to intensity fluctuations arising from the turbulence induced random phase modulation that occurs when optical beams propagate through the atmosphere. Strong scintillation will cause significant data transmission errors and inevitably make free-space optical communication impractical. Therefore they are one of the fundamental limitations in the development of free-space optical communication systems [84].

It is now well-known that partially coherent beams have lower scintillation than that of their fully coherent counterparts. On propagation through turbulence, a partially coherent beam delivers its energy through multiple incoherent spatial modes, each of which has its own distinct propagation path and intensity pattern [97]. Because of the mutual independence of these modes, the intensity of the partially coherent beam is the superposition of the individual intensity patterns, and on average the intensity received by the detector is more uniform.

After years of studies on partially coherent beam propagation in the atmosphere, the underlying physics of scintillation reduction by partially coherent beams is still obscure. Finding general guidelines for minimizing scintillation remains an open problem. On the other hand, generating a partially coherent beam with specific statistical properties itself is still a difficult issue. According to the coherent mode

representation theory [81], a partially coherent beam can be expressed as a collection of incoherent spatial modes. As a special case, it has been shown that scintillation can be significantly reduced by using incoherent beam arrays [61–63]. Therefore, they are one of the most promising partially coherent sources for free-space optical communications. However, it has been revealed that the performance of scintillation reduction by these incoherent beam arrays strongly depends on their spatial configurations. The possibility of further optimizing incoherent beam arrays, including the choice of beamlets and their spatial configurations, relies on the understanding of scintillation reduction by partially coherent beams.

In this chapter, the general guidelines for minimizing scintillation with incoherent beam arrays are explored by investigating the scintillation properties of pseudo-Bessel correlated beams in Sec. 3.1. With these guidelines, a novel beam class, Airy beams, is applied in the study of incoherent beam arrays in the atmosphere in Sec. 3.2.

3.1 Scintillation Reduction by Pseudo-Bessel Correlated Beams

So far, most studies on the propagation of partially coherent beams in turbulence have focused on the beams whose spatial correlation function is Gaussian. It has been shown that the scintillation reduction by a Gaussian correlated beam is negligible in the strong turbulence regime [10, Chapter 16]. However, it is known that partially coherent beams of different correlation types have different coherent mode representations and therefore they have different scintillation properties on propagation in the atmosphere. Bessel correlated beams are a distinct and unusual

class of partially coherent beams [98]. The studies on this beam class are inspired by the attractive properties of its counterpart in coherent regime, Bessel beams, whose name originates from the fact that their wavefields are expressed by Bessel functions. Eq. (3.1.1) shows an example of Bessel beam which propagates in the z direction [99],

$$\Phi(x, y, z; k) = \exp(i\beta z) J_0(\alpha\sqrt{x^2 + y^2}), \tag{3.1.1}$$

where J_0 is the zeroth-order Bessel function of the first kind, k is the wavenumber and $\alpha^2 + \beta^2 = k^2$. They have an invariant field distribution across any plane orthogonal to the direction of propagation [99, 100] and therefore are referred to as *nondiffracting beams*. They are also known to be able to reconstruct their initial intensity profiles after both amplitude and phase perturbations [101]. The studies on Bessel *correlated* beams show that they have similar properties to Bessel beams. It has been demonstrated that a Bessel correlated beam of infinite size is propagation-invariant in free space and in ABCD systems [102, 103], while a Bessel correlated beam of Gaussian intensity profile remains almost invariant up to a certain propagation distance [104]. It is also known that Bessel correlated beams can be used in focal spot shaping [105]. On noting the unusual properties of Bessel correlated beams in free-space propagation, it is natural to consider their scintillation properties when propagating in turbulence.

3.1.1 Model of Pseudo-Bessel Correlated Beams

Ref. [98] introduced a modal expansion for Bessel correlated beams, through which a Bessel correlated beam is decomposed as an incoherent collection of Bessel beams

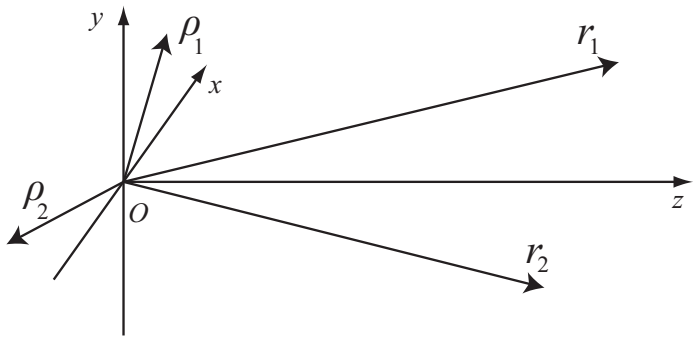

Figure 3.1: Illustration of coordinates. $\boldsymbol{\rho}$ is the projection of position vector $\mathbf{r} = (\boldsymbol{\rho}, z)$ in the transmitter plane $z = 0$.

of different orders. However, it is relatively difficult to mathematically formulate the scintillation of Bessel beams on propagation in turbulence. Therefore this modal expansion is not applicable for the investigation of scintillation properties of Bessel correlated beams. Here the concept of pseudo-Bessel correlated beams is introduced by using a discretized form of the Bessel correlation function.

The second order coherence properties of a wavefield in the transmitter plane $z = 0$ can be characterized by the cross-spectral density $W(\boldsymbol{\rho}_1, \boldsymbol{\rho}_2)$, which may always be written as [see Eq. (2.1.4) in Sec. 2.1]

$$W(\boldsymbol{\rho}_1, \boldsymbol{\rho}_2) = \sqrt{S(\boldsymbol{\rho}_1)}\sqrt{S(\boldsymbol{\rho}_2)}\mu(\boldsymbol{\rho}_1, \boldsymbol{\rho}_2), \tag{3.1.2}$$

where where $\boldsymbol{\rho}_1$ and $\boldsymbol{\rho}_2$ are the position vectors in the transmitter plane (see Fig. 3.1),$S(\boldsymbol{\rho}) = W(\boldsymbol{\rho}, \boldsymbol{\rho})$ is the spectral density at $\boldsymbol{\rho}$ and $\mu(\boldsymbol{\rho}_1, \boldsymbol{\rho}_2)$ is the spectral degree of coherence of the field at $\boldsymbol{\rho}_1$ and $\boldsymbol{\rho}_2$. For a Bessel correlated beam, its spectral degree of coherence takes on the form

$$\mu(\boldsymbol{\rho}_1, \boldsymbol{\rho}_2) = J_0\left(\frac{|\boldsymbol{\rho}_1 - \boldsymbol{\rho}_2|}{r_0}\right), \tag{3.1.3}$$

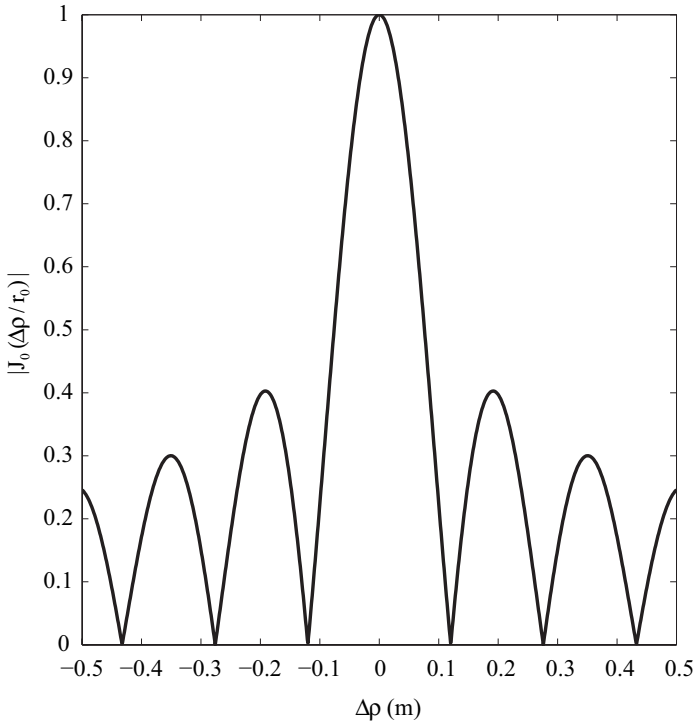

Figure 3.2: Illustration of Bessel correlation. $r_0 = 0.05$ m and $\Delta\boldsymbol{\rho} = |\boldsymbol{\rho}_1 - \boldsymbol{\rho}_2|$. The full width at half maximum (FWHM) of the central lobe is 0.152 m.

where r_0 is the effective correlation length. An illustration of Bessel correlation [Eq. (3.1.3)] is shown in Fig. 3.2.

When investigating the properties of a partially coherent beam, one important issue is the synthesis of the random wavefield such that its cross-spectral density has the desired form. For a Bessel correlated beam characterized by Eq. (3.1.3), it is noted that a Bessel function satisfies the well-known identity [106, Chapter 11]

$$J_0\left(\frac{|\boldsymbol{\rho}_1 - \boldsymbol{\rho}_2|}{r_0}\right) = \frac{1}{2\pi}\int_0^{2\pi} \exp\left[ik\mathbf{u}_\perp \cdot (\boldsymbol{\rho}_1 - \boldsymbol{\rho}_2)\right] d\phi_{u_\perp}, \tag{3.1.4}$$

where k is wavenumber, $|\mathbf{u}_\perp| = 1/(kr_0)$ and $\phi_{u_\perp}$ is the azimuthal angle of $\mathbf{u}_\perp$. On substituting Eq. (3.1.4) into Eq. (3.1.2) and discretizing the integral, the cross-

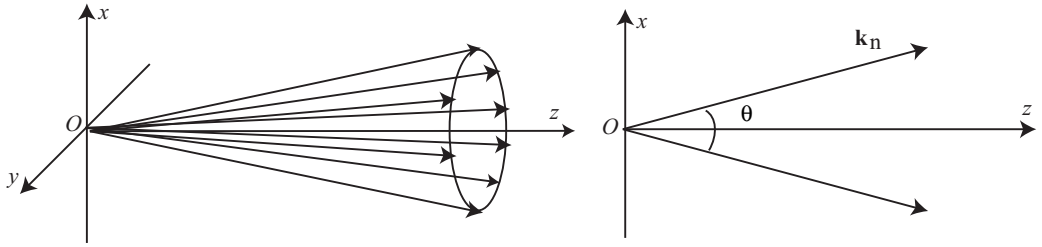

Figure 3.3: Illustration of pseudo-Bessel correlated beam. $\mathbf{k}_n$ is the wave vector of the nth beamlet. $\mathbf{k}_n = k\mathbf{u}_n$ and its direction is specified by the unit vector $\mathbf{u}_n$ whose projection in the source plane is $\mathbf{u}_{\perp n}$. $\theta = 2\text{arcsin}(|\mathbf{u}_{\perp n}|)$ is the vertex of cone.

spectral density can be approximated by a finite number of modes as

$$W(\boldsymbol{\rho}_1, \boldsymbol{\rho}_2) \approx \sum_{n=1}^{N} A_n(\boldsymbol{\rho}_1) A_n^*(\boldsymbol{\rho}_2), \tag{3.1.5}$$

where

$$A_n(\boldsymbol{\rho}) = \frac{1}{\sqrt{N}} \sqrt{S(\boldsymbol{\rho})} \exp(ik\mathbf{u}_{\perp n} \cdot \boldsymbol{\rho}), \tag{3.1.6}$$

N is the number of modes and $\mathbf{u}_{\perp n} = (\frac{1}{kr_0}, \frac{2n\pi}{N})$ in polar coordinates. It can be seen that an exact Bessel correlated beam can be synthesized by the beamlets specified by Eq. (3.1.6) when N approaches infinity. As illustrated in Fig. 3.3, the wave vectors of these beamlets form a cone whose vertex angle is inversely related to the correlation length r_0. When N is of finite value, a partially coherent beam whose cross-spectral density is specified by Eqs. (3.1.5) and (3.1.6) is defined as a *pseudo-Bessel correlated beam*. Fig. 3.3 also suggests a potential method to generate a pseudo-Bessel correlated beam, i.e. a bundle of fiber lasers arranged either to directly diverge at angle θ or first converge in a transmitter plane of angle θ.

In principle the spectral density $S(\boldsymbol{\rho})$ can be of arbitrary profile. In this section, it

is taken to be Gaussian, which is

$$S(\boldsymbol{\rho}) = \exp\left(-\frac{2\rho^2}{w_0^2}\right), \tag{3.1.7}$$

where w_0 indicates the width of the Gaussian profile. The average intensity in the transmitter plane $L = 0$ is therefore a Gaussian, regardless of state of coherence.

3.1.2 Formulation of Scintillation Index in Weak Turbulence

A pseudo-Bessel correlated beam whose constituent beamlets are specified by Eqs. (3.1.6) and (3.1.7) is considered at the source plane $z = 0$. On propagation through weak turbulence, the wavefield of the nth beamlet can be represented by a so-called *Rytov series* (see Sec. 2.3.2)

$$A_n(\boldsymbol{\rho}, z) = A_{0n}(\boldsymbol{\rho}, z) \exp\left[\psi_{n1}(\boldsymbol{\rho}, z) + \psi_{n2}(\boldsymbol{\rho}, z) + \cdots\right], \tag{3.1.8}$$

where $A_{0n}(\boldsymbol{\rho}, z)$ is the wavefield of the nth beamlet in the absence of the turbulence, $\psi_{n1}(\boldsymbol{\rho}, z)$ and $\psi_{n2}(\boldsymbol{\rho}, z)$ are the complex phase perturbations of the first and the second order associated with the nth beamlet, respectively. With the assumption of weak turbulence, perturbation terms of order higher than two are neglected.

Because of the mutual independence of the constituent beamlets, the intensity of the pseudo-Bessel correlated beam at the receiver plane $z = L$ is

$$I(\boldsymbol{\rho}, L) = \sum_{n=1}^{N} I_n(\boldsymbol{\rho}, L), \tag{3.1.9}$$

where $I_n(\boldsymbol{\rho}, L) = |A_n(\boldsymbol{\rho}, L)|^2$ is the intensity of the nth beamlet. The intensity fluctuations of the pseudo-Bessel correlated beam at the receiver plane are

characterized by the scintillation index which is defined as

$$\sigma^2(\boldsymbol{\rho}, L) = \frac{\langle I^2(\boldsymbol{\rho}, L)\rangle}{\langle I(\boldsymbol{\rho}, L)\rangle^2} - 1, \tag{3.1.10}$$

where the angle brackets stand for the average of the realizations of turbulence. With Eq. (3.1.9), the scintillation index can be rewritten as

$$\sigma^2(\boldsymbol{\rho}, L) = \frac{\sum_{m=1}^{N}\sum_{n=1}^{N}\langle I_m(\boldsymbol{\rho}, L) I_n(\boldsymbol{\rho}, L)\rangle}{\left[\sum_{n=1}^{N}\langle I_n(\boldsymbol{\rho}, L)\rangle\right]^2} - 1. \tag{3.1.11}$$

Within the framework of the Rytov approximation, the average intensity of the nth beamlet $\langle I_n(\boldsymbol{\rho}, L)\rangle$ and the average cross-intensity between the mth and nth beamlets $\langle I_m(\boldsymbol{\rho}, L) I_n(\boldsymbol{\rho}, L)\rangle$ in Eq. (3.1.11) are formulated by (for the detailed derivations, see Appendix A)

$$\langle I_n(\boldsymbol{\rho}, L)\rangle = |A_{0n}(\boldsymbol{\rho}, L)|^2 \exp\left\{2\mathrm{Re}[E_1^n(\boldsymbol{\rho}, L)] + E_2^{nn}(\boldsymbol{\rho}, L)\right\}, \tag{3.1.12}$$

$$\begin{aligned} \langle I_m(\boldsymbol{\rho}, L) I_n(\boldsymbol{\rho}, L)\rangle &= \langle I_m(\boldsymbol{\rho}, L)\rangle\langle I_n(\boldsymbol{\rho}, L)\rangle \\ &\times \exp\left\{2\mathrm{Re}[E_2^{mn}(\boldsymbol{\rho}, L)] + 2\mathrm{Re}[E_3^{mn}(\boldsymbol{\rho}, L)]\right\}, \end{aligned} \tag{3.1.13}$$

where

$$\begin{aligned} E_1^n(\boldsymbol{\rho}, L) &= -\pi k^2 \exp\left[\frac{ikLu_{\perp n}^2}{2p(L)}\right]\int \Phi_n(\boldsymbol{\kappa}) d^2\kappa \\ &\times \int_0^L \exp\left[\frac{-ik\eta u_{\perp n}^2}{2p(\eta)}\right]\exp\left[\frac{-ik\gamma(\eta)(L-\eta)u_{\perp n}^2}{2p^2(\eta)}\right] d\eta, \end{aligned} \tag{3.1.14}$$

$$
\begin{aligned}
E_2^{mn}(\boldsymbol{\rho}, L) &= 2\pi k^2 \exp\left[\frac{ikLu_{\perp m}^2}{2p(L)}\right] \exp\left[\frac{-ikLu_{\perp n}^2}{2p^*(L)}\right] \\
&\times \int_0^L \exp\left\{\frac{-ik}{2p(\eta)}\left[\eta + \frac{\gamma(\eta)(L-\eta)}{p(\eta)}\right] u_{\perp m}^2\right\} \\
&\times \exp\left\{\frac{ik}{2p^*(\eta)}\left[\eta + \frac{\gamma^*(\eta)(L-\eta)}{p^*(\eta)}\right] u_{\perp n}^2\right\} d\eta \\
&\times \int \exp\left\{\frac{-i\left[\gamma(\eta) - \gamma^*(\eta)\right](L-\eta)\kappa^2}{2k}\right\} \exp\left\{i\left[\gamma(\eta) - \gamma^*(\eta)\right]\boldsymbol{\kappa}\cdot\boldsymbol{\rho}\right\} \\
&\times \exp\left\{-i(L-\eta)\boldsymbol{\kappa}\cdot\left[\frac{\mathbf{u}_{\perp m}}{p(L)} - \frac{\mathbf{u}_{\perp n}}{p^*(L)}\right]\right\} \Phi_n(\boldsymbol{\kappa}) d^2\kappa, \qquad (3.1.15)
\end{aligned}
$$

$$
\begin{aligned}
E_3^{mn}(\boldsymbol{\rho}, L) &= -2\pi k^2 \exp\left[\frac{ikLu_{\perp m}^2}{2p(L)}\right] \exp\left[\frac{ikLu_{\perp n}^2}{2p^(L)}\right] \\
&\times \int_0^L \exp\left\{\frac{-ik}{2p(\eta)}\left[\eta + \frac{\gamma(\eta)(L-\eta)}{p(\eta)}\right] (u_{\perp m}^2 + u_{\perp n}^2)\right\} d\eta \\
&\times \int \exp\left[\frac{-i(L-\eta)}{p(L)}\boldsymbol{\kappa}\cdot(\mathbf{u}_{\perp m} - \mathbf{u}_{\perp n})\right] \\
&\times \exp\left[\frac{-i\gamma(\eta)(L-\eta)\kappa^2}{k}\right] \Phi_n(\boldsymbol{\kappa}) d^2\kappa, \qquad (3.1.16)
\end{aligned}
$$

where $p(L) = 1 + \frac{i2L}{kw_0^2}$, $\gamma(\eta) = \frac{p(\eta)}{p(L)}$ and $\Phi_n(\boldsymbol{\kappa})$ is the power spectrum of the turbulence.

3.1.3 Examples and Analysis

With the von Karman spectrum

$$
\Phi_n(\boldsymbol{\kappa}) = 0.033 C_n^2 \frac{\exp(-\kappa^2/\kappa_m^2)}{(\kappa^2 + \kappa_0^2)^{11/6}}, \qquad (3.1.17)
$$

the scintillation index of a pseudo-Bessel correlated beam can be numerically evaluated by substituting Eqs. (3.1.12)-(3.1.17) into Eq. (3.1.11). Here $\kappa_m = 5.92/l_m$ with the inner scale $l_m = 1$ mm and $\kappa_0 = 1/l_0$ with the outer scale $l_0 = 10$ m.

A simple example of a Bessel correlated beam is one with two beamlets. Its on-axis scintillation as a function of the relative correlation length r_0/w_0 in weak turbulence

is shown in Fig. 3.4. The turbulence strength parameter is $C_n^2 = 10^{-15}$ m$^{-2/3}$ and the propagation distance is $L = 2$ km. The on-axis scintillation index of a fully coherent Gaussian beam with the same width w_0 is also shown on the plot as a horizontal line for comparison. It can be seen that a minimum of the scintillation for a pseudo-Bessel correlated beam occurs when $r_0/w_0 \approx 0.32$, which is 50% of the scintillation of a Gaussian beam alone. The simulated on-axis scintillation indices for some different values of r_0/w_0, obtained by the multiple random phase screen method, are also shown in Fig. 3.4 for comparison. In the simulation, the constituent beamlets given by Eq. (3.1.6) are propagated through the same realization of the turbulence, and their intensities are added at the receiver plane according to Eq. (3.1.9). As shown by Fig. 3.4, the numeric results have good agreement with the analytic results obtained by the Rytov theory.

The origin of the minimum scintillation in Fig. 3.4 can be explained by straightforward physical reasoning. In the coherent limit $r_0 = \infty$, the cone in Fig. 3.3 shrinks into a line. In effect, all beamlets propagate along the z-axis and through the same region of turbulence. Consequently, the scintillation in this case is equivalent to that of a single Gaussian beam. As the correlation length r_0 decreases from the coherent limit $r_0 \to \infty$, the beamlets gradually separate. They propagate in different directions and through different parts of the atmosphere. As a result, their fields are less correlated on propagation through the turbulence and on average the scintillation of the pseudo-Bessel correlated beam is reduced. However, in the low coherence regime ($r_0 \to 0$), the constituent beamlets propagate in directions

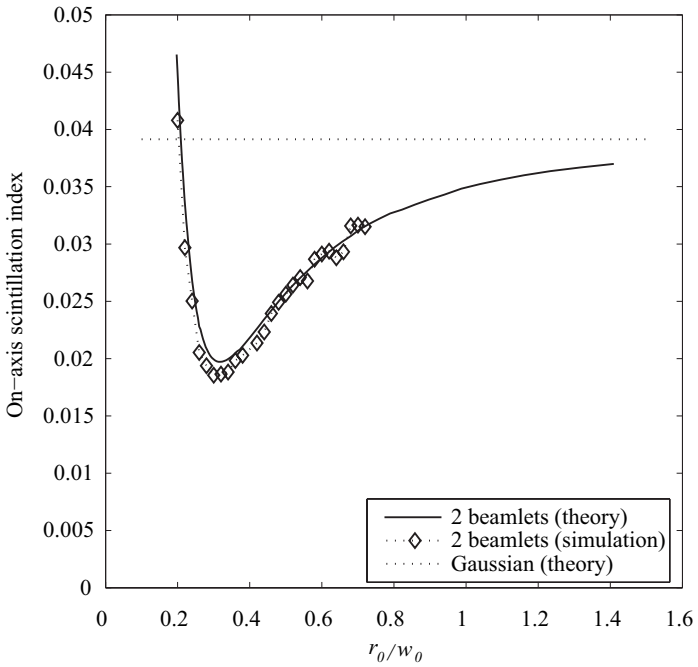

Figure 3.4: The on-axis scintillation of a 2-beamlet pseudo-Bessel correlated beam as a function of the relative correlation length r_0/w_0. Here the wavelength is taken to be $\lambda = 1.55\,\mu$m and the width of the beam is taken to be $w_0 = 0.05$ m. The turbulence strength parameter is $C_n^2 = 10^{-15}$ m$^{-2/3}$ and the propagation distance is $L = 2$ km.

very distant from the horizontal axis, resulting in low light intensity being received by the on-axis detector. This corresponds to a very small denominator in Eq. (3.1.10) and consequently a very large value for the scintillation index. After balancing the path independence of the beamlets with a high intensity at the detector, an optimal solution of r_0 exists between the low and high coherence extremes.

From the beam model developed in Sec. 3.1.1, a true Bessel correlated beam is the extreme case of the pseudo-Bessel correlated beam when the number of beamlets $N \to \infty$. Therefore, its scintillation properties can be probed by investigating the scintillation properties of the corresponding pseudo-Bessel correlated beam with a significantly large N. Fig. 3.5 illustrates the dependence of

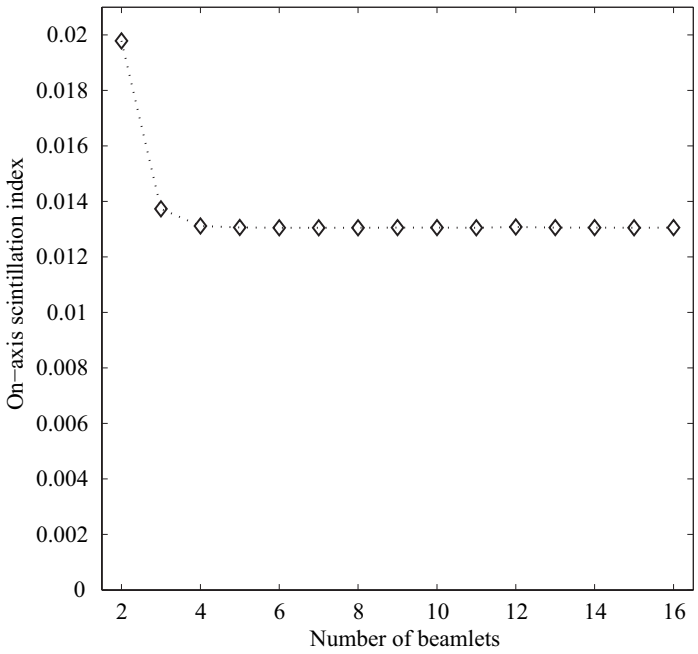

Figure 3.5: The on-axis scintillation of a pseudo-Bessel correlated beam as a function of the number of its constituent beamlets N. The relative correlation length is taken to be $r_0/w_0 = 0.33$. The rest of the parameters are the same as in Fig. 3.4.

the on-axis scintillation index of a pseudo-Bessel correlated beam on the number of its constituent beamlets. The relative correlation length r_0/w_0 is 0.33. As N increases, the on-axis scintillation index falls and saturates rapidly. When N is small, the propagation of the additional beamlets is still relatively uncorrelated with the propagation of the existing beamlets and the scintillation of the pseudo-Bessel correlated beam is reduced. However, when N is large, the additional beamlets propagate through very similar regions of turbulence as the existing beamlets and make no further contribution to the scintillation reduction. From Fig. 3.5, it can be seen that the scintillation of a Bessel correlated beam can be well represented by the scintillation of a pseudo-Bessel correlated beam with a finite number of constituent beamlets. As illustrated by Fig. 3.6, the minimum on-axis scintillation index of a

16-beamlet pseudo-Bessel correlated beam is 21% of the on-axis scintillation index of a Gaussian beam.

Figs. 3.5 and 3.6 show that for the purpose of scintillation reduction a true Bessel correlated beam is not significantly better than a beam with a finite and even small number of modes. This observation has important implications for the use of partially coherent beams in scintillation reduction. In general, the crucial reason for the overall scintillation reduction of a partially coherent beam is the mutually independent propagation of their constituent beamlets through the atmosphere. This requirement is referred to as the need for *diversity* in the beamlet behavior. This diversity could be spatial (beamlets start at different locations as studied in Refs. [61–63]) or directional (beamlets start at the same location but propagate in different directions as shown in Fig. 3.3). However, a partially coherent beam can always be decomposed into a continuous collection of beamlets, and most of this continuum provides no improvement over a discrete set of beamlets. The results here suggest that familiar classes of partially coherent beams are, in a sense, wasteful.

The analytic formulae of scintillation of pseudo-Bessel correlated beams obtained by the Rytov approximation in Sec. 3.1.2 is valid only in weak turbulence. However the multiple random phase screen method does not have this limitation. Now the study on the scintillation of pseudo-Bessel correlated beams is extended into the strong turbulence regime by numeric simulations. The turbulence strength parameter is $C_n^2 = 10^{-14}$ m$^{-2/3}$ and the propagation distance is $L = 3$ km. As shown in Fig. 3.7,

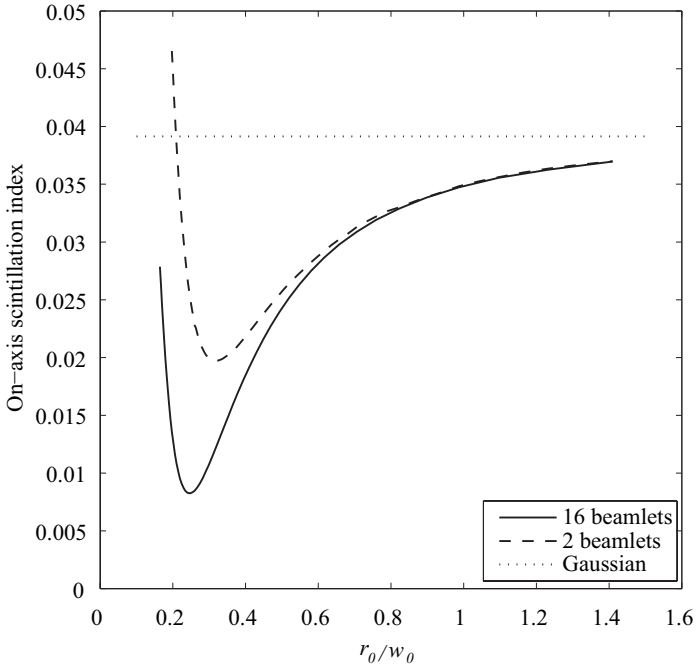

Figure 3.6: The on-axis scintillation of a 16-beamlet pseudo-Bessel correlated beam as a function of the relative correlation length r_0/w_0. The parameters are the same as in Fig. 3.4.

the behavior of the on-axis scintillation index of a pseudo-Bessel correlated beam as a function of the relative correlation length r_0/w_0 is similar to the analytic result obtained by the Rytov theory and the maximum scintillation reduction saturates as the increase of the number of constituent beamlets N. When $N = 8$, a minimum on-axis scintillation index, 26.8% of the on-axis scintillation index of a Gaussian beam, is obtained when $r_0/w_0 = 0.28$. Fig. 3.8 illustrates the on-axis scintillation index of a 8-beamlet pseudo-Bessel correlated beam as a function of the Rytov variance [Eq. (2.3.7)]. The beam is of the optimal correlation length obtained from Fig. 3.7. It can be seen that the pseudo-Bessel correlated beam significantly outperforms the Gaussian beam.

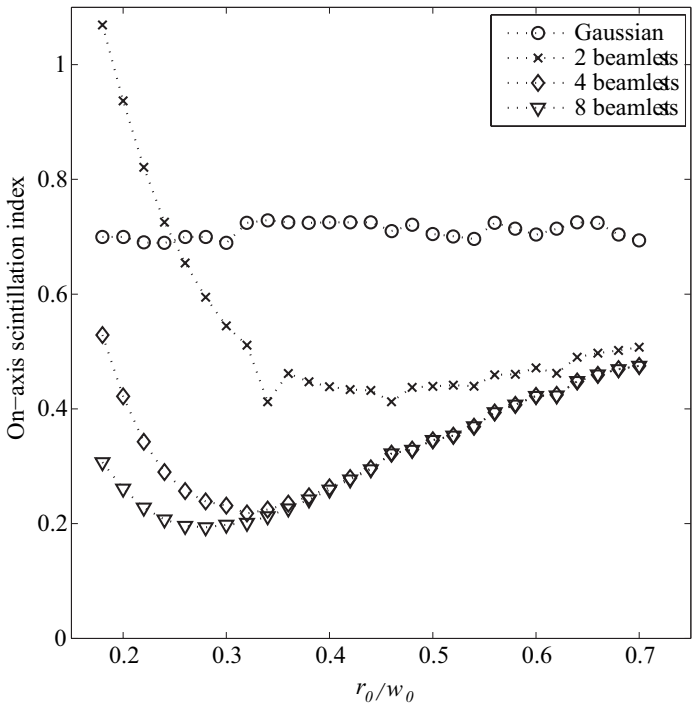

Figure 3.7: The on-axis scintillation of a pseudo-Bessel correlated beam as a function of the relative correlation length r_0/w_0. The wavelength is also $\lambda = 1.55\,\mu$m and the width of the beam is $w_0 = 0.05$ m. Here the turbulence strength parameter is $C_n^2 = 10^{-14}$ m$^{-2/3}$ and the propagation distance is $L = 3$ km.

3.1.4 Scintillation of Modified Pseudo-Bessel Correlated Beams

As discussed in Sec. 3.1.3, the scintillation of a pseudo-Bessel correlated beam increases rapidly if the correlation length decreases below its optimal value. This arises because the beamlets mostly "miss" the detector, but high variations in intensity are produced when a beamlet occasionally wanders into its range. To correct this, the configuration of pseudo-Bessel correlated beams is modified by adding an independent horizontal beamlet

$$E(\boldsymbol{\rho}, z = 0) = E_0 \exp\left(-\frac{\rho^2}{w_0^2}\right), \tag{3.1.18}$$

where E_0 is the amplitude. For simplicity, its beam width is also w_0.

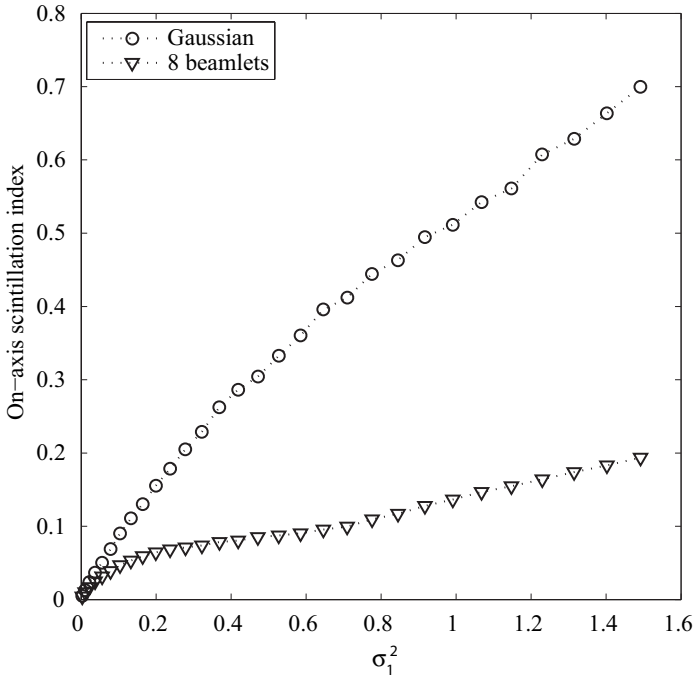

Figure 3.8: The on-axis scintillation of a 8-beamlet pseudo-Bessel correlated beam as a function of the Rytov variance σ_1^2. The relative correlation length is $r_0/w_0 = 0.28$ and the other parameters are the same as in Fig. 3.7.

It can be shown that the on-axis scintillation index of the modified pseudo-Bessel correlated beam takes on the minimum value given by[1]

$$\sigma_{min}^2 = \begin{cases} \frac{\sigma_{pb}^2\sigma_h^2 - (\sigma_{pb,h}^2)^2}{\sigma_{pb}^2 + \sigma_h^2 - 2\sigma_{pb,h}^2} & \text{if } \sigma_{pb,h}^2 < \min[\sigma_{pb}^2, \sigma_h^2] \\ \\ \min[\sigma_{pb}^2, \sigma_h^2] & \text{otherwise} \end{cases}, \tag{3.1.19}$$

when

$$E_0 = \sqrt{\frac{I_{pb}(\sigma_{pb}^2 - \sigma_{pb,h}^2)}{I_h(\sigma_h^2 - \sigma_{pb,h}^2)}} \quad \text{if } \sigma_{pb,h}^2 < \min[\sigma_{pb}^2, \sigma_h^2]. \tag{3.1.20}$$

In Eqs. (3.1.19) and (3.1.20), σ_{pb}^2 and σ_h^2 are the on-axis scintillation indices of the pseudo-Bessel correlated beam and the horizontal beamlet, respectively. $\sigma_{pb,h}^2$ is the on-axis cross scintillation index between the pseudo-Bessel correlated beam and the

[1]Eqs. (3.1.19) and (3.1.20) can be obtained by a similar manner shown in Sec. 4.1.2.

horizontal beamlet, which is defined as

$$\sigma_{pb,h}^2 = \frac{\langle I_{pb} I_h \rangle}{\langle I_{pb} \rangle \langle I_h \rangle} - 1. \tag{3.1.21}$$

I_{pb} and I_h are the on-axis intensities of the pseudo-Bessel correlated beam and the horizontal beamlet. $\min[\sigma_{pb}^2, \sigma_h^2]$ takes the minimum between σ_{pb}^2 and σ_h^2. In addition, with the assumption of isotropic turbulence, it can be shown that

$$\begin{aligned} \langle I_{pb} \rangle &= \langle \Sigma_{n=1}^N I_n \rangle = N \langle I_n \rangle \\ \langle I_{pb} I_h \rangle &= \langle \Sigma_{n=1}^N I_n I_h \rangle = N \langle I_n I_h \rangle. \end{aligned} \tag{3.1.22}$$

On substituting Eq. (3.1.22) into Eq. (3.1.21), it can be shown that $\sigma_{pb,h}^2 = \sigma_{n,h}^2$ where

$$\sigma_{n,h}^2 = \frac{\langle I_n I_h \rangle}{\langle I_n \rangle \langle I_h \rangle} - 1 \tag{3.1.23}$$

is the on-axis cross scintillation index between the n^{th} beamlet of the pseudo-Bessel correlated beam and the horizontal beamlet.

In weak turbulence, the minimum on-axis scintillation index of the modified pseudo-Bessel correlated beams [Eq. (3.1.19)] can be numerically evaluated by the formulae derived in Sec. 3.1.2. It is illustrated as a function of the relative correlation length r_0/w_0 in Fig. 3.9. The corresponding optimal amplitude E_0 is also shown. The number of constituent beamlets of the pseudo-Bessel correlated beam is 16. It can be seen that when coherence is relatively high, the minimum on-axis scintillation index of the modified pseudo-Bessel correlated beam is equal to the on-axis scintillation index of the pseudo-Bessel correlated beam itself because $\sigma_{pb}^2 < \sigma_{pb,h}^2$ and $\sigma_{pb}^2 < \sigma_h^2$.

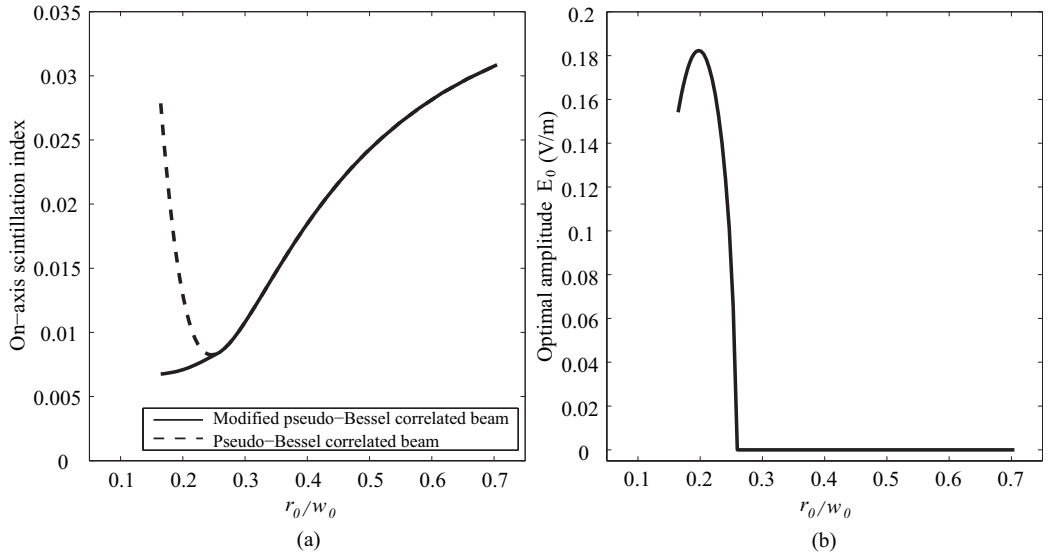

Figure 3.9: In (a) the dashed curve shows the on-axis scintillation of a 16-beamlet pseudo-Bessel correlated beam as a function of the relative correlation length r_0/w_0, while the solid curve shows the minimum on-axis scintillation of the corresponding modified pseudo-Bessel correlated beam. The optimal amplitude E_0 is shown in (b). The parameters are the same as in Fig. 3.6.

Therefore there is no need to add the additional horizontal beamlet in this regime. However in the low coherence regime, $\sigma^2_{pb,h} < \min[\sigma^2_{pb}, \sigma^2_h]$, the additional horizontal beamlet keeps the scintillation of the modified pseudo-Bessel correlated beams at a low level for a relatively large range of the correlation length r_0. If r_0 further decreases, it can be expected that the detected on-axis intensity is dominated by the additional horizontal beamlet and the on-axis scintillation index of the modified pseudo-Bessel correlated beam increases and approaches σ^2_h eventually.

Fig. 3.10 illustrates the minimum on-axis scintillation index of the modified pseudo-Bessel correlated beams as well as the optimal amplitude E_0 in strong turbulence; these quantities are obtained by numeric simulations. The number of constituent beamlets of the pseudo-Bessel correlated beam is 8. A behavior similar to that of Fig. 3.9 is observed.

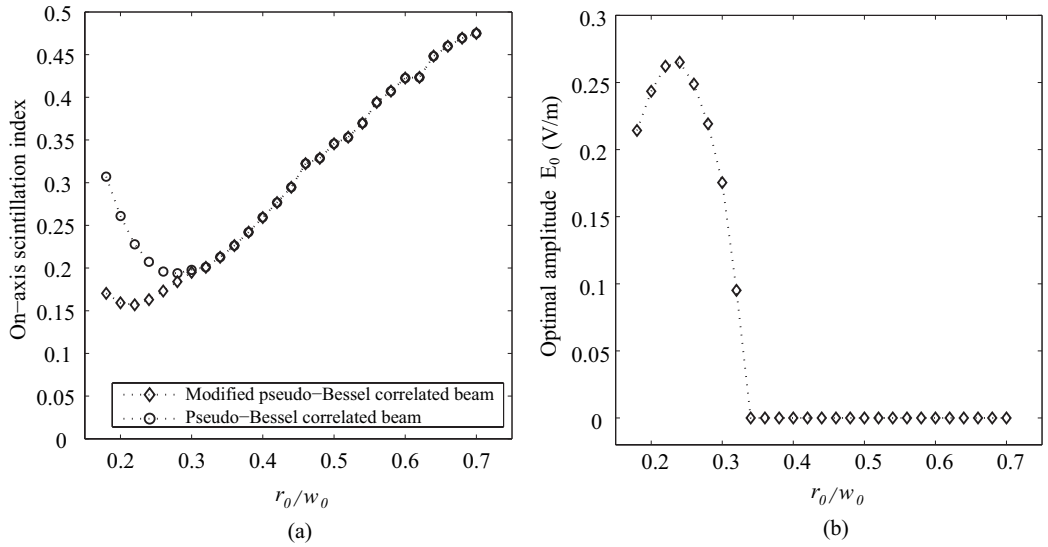

Figure 3.10: In (a) the dashed curve shows the on-axis scintillation of a 16-beamlet pseudo-Bessel correlated beam as a function of the relative correlation length r_0/w_0, while the solid curve shows the minimum on-axis scintillation of the corresponding modified pseudo-Bessel correlated beam. The optimal amplitude E_0 is shown in (b). The parameters are the same as in Fig. 3.7.

3.2 Scintillation Reduction by Airy Beam Arrays

From Sec. 3.1, it has been shown that beamlets' independent propagation in the atmosphere is crucial for scintillation reduction by incoherent beam arrays. For either the directionally diverse incoherent beam arrays such as pseudo-Bessel correlated beams or the spatially diverse incoherent beam arrays studied in Refs. [61–63], significant scintillation reduction can be achieved with appropriate separation of the constituent beamlets. However, both of these two kinds of incoherent beam arrays suffer significant scintillation increase if the spatial separation of beamlets deviates from the optimal value. In addition, the problem of low received energy exists since their beamlets are spatially diverse. Recently a different configuration of incoherent beam array was investigated [107]. The

spatially diverse beamlets are inclined to overlap at the receiver plane and the results show advantages over that the parallel beamlets configuration studied in Refs. [61–63]. However, an optimal inclination could be difficult to achieve over long propagation distances.

The abovementioned problems of incoherent beam arrays in turbulence applications are due in part to the fact that their beamlets belong to conventional beam classes whose average propagation paths in turbulence are straight lines. So far, the typical beam class for the generation of incoherent beam arrays is Gaussian beams. On propagation in the atmosphere, most of the energy transmitted by Gaussian beams is distributed along their own propagation axes. As a result, they only partially overlap on the receiver plane and only a small proportion of the transmitted energy is received by the on-axis detector. In addition to being inefficient, the low received intensity corresponds to a small denominator in Eq. (3.1.10) and consequently a large value for the scintillation index. With these difficulties in mind, a straightforward solution arises, i.e. developing an array of special beamlets that are initially spatially separated but can self-bend on propagation and finally overlap at the receiver plane.

The recent studies on Airy beams provide a potential method to generate such special incoherent beam arrays. Airy wave packets were initially reported as a nondiffracting solution of the free-space Schrödinger equation within the context of quantum mechanics [108]. By the mathematical analogy between the free-space Schrödinger equation and the paraxial wave equation, optical Airy beams were theoretically predicted and experimentally observed [109, 110]. The most exotic

feature of Airy beams is their ability to transversely accelerate, i.e. to propagate along parabolic trajectories in free space [111]. It has also been shown that Airy beams can self-reconstruct themselves after partial obstruction by obstacles and that they retain their intensity profiles under turbulent conditions [78]. These intriguing properties suggest that Airy beams could be a good choice for incoherent beam arrays in turbulence applications.

3.2.1 Propagation of Airy Beams in Atmospheric Turbulence

To begin with, the free-space propagation of Airy beams is considered. They satisfy, as do all beams, the normalized paraxial wave equation

$$i\frac{\partial U}{\partial \xi} + \frac{\partial^2 U}{\partial s^2} = 0, \tag{3.2.1}$$

where $\xi = z/k_0 x_0^2$ is the normalized propagation distance and $s = x/x_0$ is a dimensionless transverse coordinate. x_0 is a arbitrary transverse scale. It can be shown that this equation has the following solution

$$U(\xi, s) = \mathrm{Ai}\left[s - (\xi/2)^2\right] \exp\left[i\left(s\xi/2 - \xi^3/12\right)\right], \tag{3.2.2}$$

where $\mathrm{Ai}(x)$ represents the Airy function

$$\mathrm{Ai}(x) = \frac{1}{\pi}\int_0^\infty \cos\left(\frac{1}{3}t^3 + xt\right) dt. \tag{3.2.3}$$

Eq. (3.2.2) represents a nondiffracting beam since the intensity profile ($\propto |U(\xi, s)|^2$) does not change on propagation. Furthermore, it can be seen that the origin of the beam accelerates in the positive s-direction with increasing ξ. However, an ideal

Airy beam is not physically realizable, as it possesses infinite energy[2]. Siviloglou et al. [109, 110] proposed and demonstrated a feasible model by truncating ideal Airy beams with an exponential function, which takes the following form in the source plane $z = 0$,

$$U(s, \xi = 0) = \mathrm{Ai}(s) \exp(as). \tag{3.2.4}$$

Here a is the exponential truncation factor. With this initial condition, the propagating wavefield at plane z is given by

$$U(s, \xi) = \mathrm{Ai}\left[s - (\xi/2)^2 + ia\xi\right] \exp\left[as - \left(a\xi^2/2\right) - i\left(\xi^3/12\right) + i\left(a^2\xi/2\right) + i\left(s\xi/2\right)\right]. \tag{3.2.5}$$

The propagation dynamics of an Airy beam is illustrated in Fig. 3.11, which clearly shows a parabolic trajectory and indicates that the beam self bends in the transverse direction on propagation in free space. The model of an Airy beam given in Eq. (3.2.5) can be easily extended to a two dimensional model, of the form

$$U(s_x, s_y, \xi) = U(s_x, \xi)U(s_y, \xi), \tag{3.2.6}$$

where $s_x = x/x_0$ and $s_y = y/y_0$. x_0 and y_0 are transverse scales. For the symmetric case when $x_0 = y_0$, it can be anticipated that Airy beams move along the 45° axis in the $x - y$ plane.

The self-bending property of Airy beams seen in Fig. 3.11 indicates a potential type of incoherent beam array configuration: an array of Airy beams that begin at different transverse locations but curve to come together at the detector. However,

[2]The total energy is proportional to $\int |U(\xi, s)|^2 d\xi$, while here $\int |U(\xi, s)|^2 d\xi \to \infty$ for Airy beams.

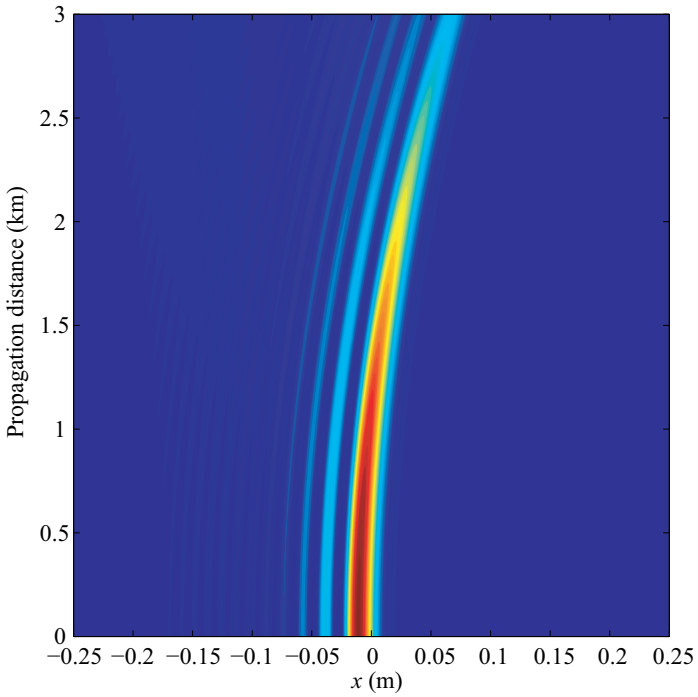

Figure 3.11: Illustration of propagation dynamics of an 1-D Airy beam in free space. The wavelength is taken to be $\lambda = 1.55\,\mu$m, the transverse scale $x_0 = 0.012$ m, and the truncation factor $a = 0.1$.

it is not clear whether Airy beams can maintain their acceleration property over the kilometer-order atmospheric propagation distances required for atmospheric communication. Therefore, before considering scintillation, it is necessary to investigate their propagation dynamics in the atmosphere.

The atmospheric propagation dynamics of a beam can be studied through the evolution of its average intensity profile in the atmosphere. By the extended Huygens-Fresnel principle, the average intensity $\langle I \rangle$ of a beam at plane $z = L$ is given by

$$\begin{aligned} \langle I(\boldsymbol{\rho}, L)\rangle &= \left(\frac{k_0}{2\pi L}\right)^2 \int d^2\rho_1' \int d^2\rho_2' U_0(\boldsymbol{\rho}_1', 0) U_0^*(\boldsymbol{\rho}_2', 0) \exp\left[\frac{ik_0|\boldsymbol{\rho} - \boldsymbol{\rho}_1'|^2}{2L}\right] \\ &\times \exp\left[-\frac{ik_0|\boldsymbol{\rho} - \boldsymbol{\rho}_2'|^2}{2L}\right] \langle \exp\left[\varphi(\boldsymbol{\rho}, \boldsymbol{\rho}_1') + \varphi^*(\boldsymbol{\rho}, \boldsymbol{\rho}_2')\right]\rangle, \end{aligned} \tag{3.2.7}$$

where $U(\boldsymbol{\rho}', 0)$ is the incident wavefield on the source plane and $\varphi(\boldsymbol{\rho}, \boldsymbol{\rho}_1')$ is the random

part of the complex phase of a spherical wave. On substituting the expression of Airy beam on the source plane

$$\begin{aligned} U(\boldsymbol{\rho}', 0) &= U(x', y', 0) \\ &= \mathrm{Ai}(s'_x)\exp(as'_x)\mathrm{Ai}(s'_y)\exp(as'_y), \end{aligned} \tag{3.2.8}$$

and using the quadratic approximation of the turbulence term in Eq. (3.2.7) [see Eq. (2.3.49) in Sec. 2.3.3]

$$\langle \exp\left[\varphi(\boldsymbol{\rho}, \boldsymbol{\rho}'_1) + \varphi^*(\boldsymbol{\rho}, \boldsymbol{\rho}'_2)\right]\rangle \approx \exp\left[-\frac{(\boldsymbol{\rho}'_2 - \boldsymbol{\rho}'_1)^2}{\rho_0^2}\right], \tag{3.2.9}$$

the propagation dynamics of Airy beams in the atmosphere can be studied by numerically evaluating Eq. (3.2.7).

Fig. 3.12 illustrates the average propagation dynamics of a 2-D Airy beam in turbulence. It can be seen that on average the beam still propagates along a parabolic trajectory in the atmosphere; its average intensity decreases more rapidly. However, one precondition to use Airy beams in incoherent beam arrays for turbulence applications is to determine the curvature of their parabolic trajectories, so that the intensity peaks of individual Airy beamlets can be chosen to fully overlap on the detector plane and the the energy received by the on-axis detector can be maximized. Fig. 3.13 shows the position of an Airy beam's peak as a function of propagation distance, which explicitly illustrates the curvature of the beam propagation trajectory. When propagating in free space an Airy beam initially propagates along a parabolic trajectory, but eventually loses the free

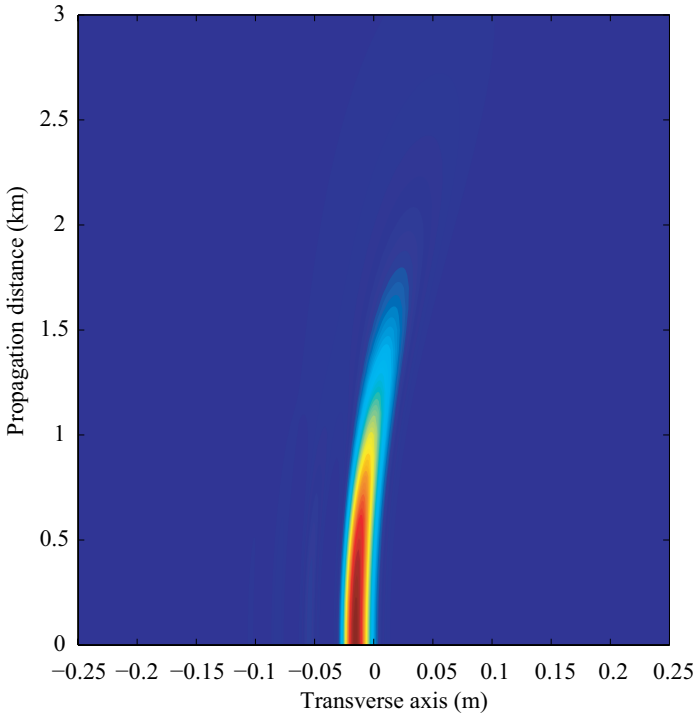

Figure 3.12: Illustration of average propagation dynamics of an 2-D truncated Airy beam in turbulence. The wavelength is taken to be $\lambda = 1.55\,\mu$m, the transverse scale $x_0 = 0.012$ m and $y_0 = 0.012$ m, the truncation factor $a = 0.1$, and the turbulence strength parameter $C_n^2 = 10^{-14}$ m$^{-2/3}$.

transverse acceleration feature due to the exponential truncation, as pointed out in Ref. [109]. For the propagation in the atmosphere, the beam propagates along a similar trace except that the turbulence makes the transverse displacement of the peak smaller than the one in free space propagation in the parabolic part. As shown in Fig. 3.13, this difference in the transverse displacement becomes larger as the propagation distance increases.

3.2.2 Scintillation of Airy Beam Arrays in Atmospheric Turbulence

As the self-bending property of Airy beams in turbulence propagation has been demonstrated in the previous section, now they can be used to generate an incoherent beam array for turbulence applications. A 4-beamlet Airy beam array is defined,

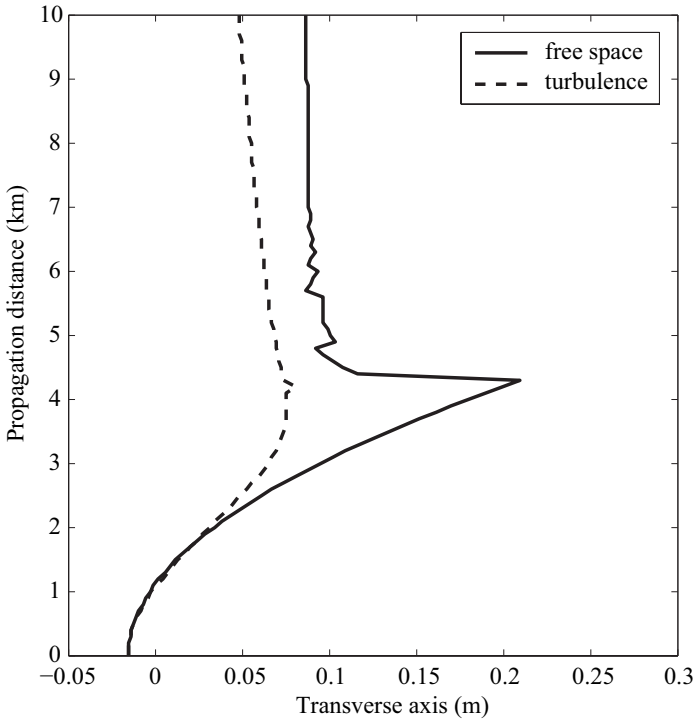

Figure 3.13: The position of the beam peak for an Airy beam in free space (solid) and in turbulence (dashed). The parameters are the same as in Fig. 3.12.

where its beamlets take on the following form in the plane $z = 0$

$$U_m(s_{xm}, s_{ym}) = \mathrm{Ai}(s_{xm}) \exp(a s_{xm}) \mathrm{Ai}(s_{ym}) \exp(a s_{ym}), \tag{3.2.10}$$

where

$$\begin{cases} s_{xm} = (x \cos\theta_m + y \sin\theta_m + d)/x_0, \\ \\ s_{ym} = (-x \sin\theta_m + y \cos\theta_m + d)/y_0, \end{cases} \tag{3.2.11}$$

d is the transverse displacement parameter and $m = 1, 2, 3, 4$ labels the mth beamlet. Here x_0 and y_0 are taken to be 0.012 m, $a = 0.1$ and $\theta_m = \frac{(m-1)\pi}{2}$. The first beamlet is obtained by shifting an Airy beam [Eq. (3.2.6)] in the $x - y$ plane for $(-d, -d)$ and the rest of beamlets are obtained by rotating the first beamlet for

the corresponding angle θ_m in counterclockwise. For specific propagation and turbulence conditions, the transverse displacement parameter d should be carefully chosen so that the average peaks of the all four Airy beamlets will fully overlap on the corresponding receiver plane. From the analysis in Sec. 3.2.1, it can be shown that the position of the Airy beam's average peak is at $(0.046\text{ m}, 0.046\text{ m})$ after propagating 3 km in turbulence when its strength is $C_n^2 = 10^{-14}\text{ m}^{-2/3}$. Therefore the transverse displacement parameter d is taken to be 0.046 m under these conditions[3]. The multiple random phase screen method is used to simulate Airy beam propagation in the atmosphere. Fig. 3.14 illustrates the simulated intensity pattern of the array in the receiver plane $z = 3$ km. Compared to the corresponding intensity pattern in the transmitter plane $z = 0$, it can be seen that the four initially separated beamlets meet in the receiver plane and their intensity peaks fully overlap at the on-axis detector.

The scintillation of an Airy beam array at the receiver plane is characterized by the scintillation index

$$\sigma^2(x, y, L) = \frac{< I^2(x, y, L) >}{< I(x, y, L) >^2} - 1, \tag{3.2.12}$$

where the instantaneous intensity I is the superposition of the constituent beamlets' instantaneous intensities. The correlation of intensity fluctuations between two

[3]It is worth mentioning that for relatively short propagation distances, the difference between the free-space and atmospheric trajectories of an Airy beam is small (Fig. 3.13). Therefore it will not lead to significant difference if the transverse displacement parameter d is estimated based on the Airy beam's free-space expression [Eq. (3.2.5)].

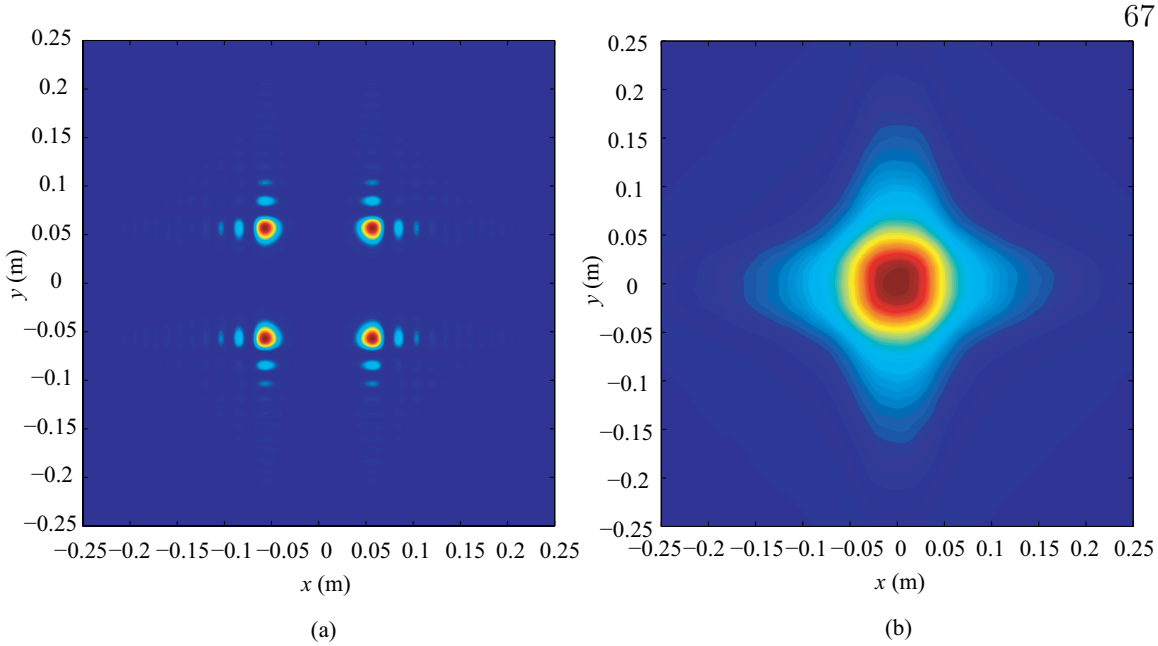

Figure 3.14: Illustration of the intensity patterns of a 4-beamlet Airy beam array in (a) the transmitter plane and (b) receiver plane. The transverse displacement parameter d is taken to be 0.046 m. The rest of the parameters are the same as in Fig. 3.12.

individual beamlets is characterized by the cross scintillation index

$$\sigma^2_{mn}(x,y,L) = \frac{< I_m(x,y,L) I_n(x,y,L) >}{< I_m(x,y,L) >< I_n(x,y,L) >} - 1. \tag{3.2.13}$$

When the subscripts $m = n$, Eq. (3.2.13) reduces to Eq. (3.2.12) and represents the self scintillation index of the mth beamlet. The simulated on-axis self and cross scintillation indices of the four beamlets of Airy beam array are shown in Tab. 3.1. The self scintillation indices are roughly the same, on average about 0.60[4]. The cross scintillation indices are nearly zero. It is shown that the four beamlets propagate through relatively independent regions of turbulence and their own turbulence-induced intensity fluctuations are mutually uncorrelated. As a result, the

[4]The on-axis self scintillation indices of the four beamlets should be theoretically the same by the assumption of the homogeneous and isotropic turbulence. The small discrepancy in Tab. 3.1 is possibly due to the discrete sampling of the turbulence spectrum and the finite number of realizations.

Table 3.1: On-axis self and cross scintillation indices of the four constituent beamlets of an Airy beam array at the receiver plane $L = 3$ km. The transverse displacement parameter d is 0.046 m. The rest parameters are the same as in Fig. 3.12.

σ^2_{mn}	$n = 1$	$n = 2$	$n = 3$	$n = 4$
$m = 1$	0.5835	0.0178	−0.0131	0.0071
$m = 2$	0.0178	0.5962	0.0356	0.0155
$m = 3$	−0.0131	0.0356	0.5980	−0.0163
$m = 4$	0.0071	0.0155	−0.0163	0.6107

on-axis scintillation index of the beam array, which is 0.1551, is roughly one fourth of the on-axis scintillation indices of the individual beamlets. This is very close to the theoretical limit of the maximum scintillation reduction of beam arrays, i.e. $\sigma^2_{min} = \sigma^2_{ind}/N$, where σ^2_{ind} is the scintillation index of the individual beamlet and N is the number of beamlets.

Here the scintillation properties of a 4-beamlet Airy beam array is considered. It is also to be noted from Tab. 3.1 that a two or three-beamlet array will produce a one-half or two-thirds reduction, respectively. In principle, the number of the constituent beamlets could be of any positive integer and the corresponding beam array can be generated in a similar manner as the four beamlet case [Eqs. (3.2.10) and (3.2.11)]. When the prerequisite of the beamlets independent atmospheric propagation is satisfied, the overall scintillation of a beam array can be further reduced by increasing the number of beamlets. However, the maximum number of beamlets is limited by the transverse displacement of Airy beamlets. A typical Airy beam array configuration is shown in Fig. 3.14a. The four beamlets are located on a circle centered on the propagation axis, while the radius of this circle takes the value

of the transverse displacement of Airy beamlets. As the number of beamlets on this circle increases, their mutual separation decreases until it reaches the minimum value required by the prerequisite of the beamlets independent atmospheric propagation. For the beam and atmospheric propagation parameters used in this chapter, the on-axis scintillation indices of an Airy beam array are 0.1152 and 0.0992 when the number of beamlets is 6 and 8 respectively. Compared to the scintillation index of individual beamlets (≈ 0.60), it is evidently shown that the scintillation reduction contributed by adding beamlets is saturated when the number of beamlet is 8.

It is worth noting that a sufficient initial separation between the beamlets of an Airy beam array is crucial for their mutually independent propagation through turbulence. It requires large transverse displacements of the beamlets' intensity peaks so that they can overlap at the receiver plane. However, a practical Airy beam is truncated and of finite energy. As shown in Fig. 3.13, these Airy beams can only keep their free transverse acceleration feature up to a certain propagation distance. Considering the long-range propagation of optical beams in free-space optical communications, the transverse scale and truncation parameters of Airy beams should be appropriately chosen so that they can retain adequate transverse displacements of intensity peaks.

3.3 Summary

In this chapter, the scintillation properties of pseudo-Bessel correlated beams of Gaussian intensity profile have been investigated in both weak and strong turbulence. With an appropriately-chosen coherence parameter, it is demonstrated

that such beams have lower scintillation than comparable fully coherent Gaussian beams. Pseudo-Bessel correlated beams are effectively a kind of directionally diverse incoherent beam array. It is noted that scintillation reduction by incoherent beam arrays is generally due to the constituent beamlets' mutually independent propagation through turbulence, which is the result of sufficient spatial separation between the bemlets. It suggests that in general, the optimal scintillation reduction can always be achieved with a relatively small and finite number of such beamlets. Considering that a partially coherent beam is the incoherent superposition of a continuous collection of beamlets, these results suggest that true partially coherent beams are in sense wasteful and incoherent beam arrays are an effective method for scintillation reduction.

Based on the results on pseudo-Bessel correlated beams, the scintillation properties of Airy beam arrays in the atmosphere was also studied. By utilizing the self-bending property of Airy beams, it has been shown that with appropriate parameters, the Airy beamlets can propagate through relatively independent regions of turbulence but still largely overlap at the on-axis detector. The scintillation of the beam array is significantly reduced compared to a single Airy beam and near the theoretical minimum.

CHAPTER 4: SCINTILLATION REDUCTION BY NONUNIFORMLY POLARIZED BEAMS

In Chapter 3, scintillation reduction by incoherent beam arrays has been investigated. To better understand the mechanism by which reduction occurs, the expression of scintillation index for an incoherent beam array [Eq. (3.1.11)] can be rewritten in the following form

$$\begin{aligned}\sigma^2 &= \frac{\sum_{m=1}^{N}\sum_{n=1}^{N}\langle I_m I_n\rangle}{\left(\sum_{n=1}^{N}\langle I_n\rangle\right)^2} - 1 \\ &= \frac{\sum_{m=1}^{N}\langle I_m\rangle^2\sigma_{mm}^2 + \sum_{m=1}^{N}\sum_{n=1,n\neq m}^{N}\langle I_m\rangle\langle I_n\rangle\sigma_{mn}^2}{\left(\sum_{n=1}^{N}\langle I_n\rangle\right)^2},\end{aligned} \tag{4.0.1}$$

where the argument $(\boldsymbol{\rho}, L)$ is omitted for brevity. The quantities σ_{mm}^2 and σ_{mn}^2 are the self and cross scintillation indices, defined in Eq. (3.2.13). With appropriate angular separation, pseudo-Bessel correlated beams have small scintillation because the intensity correlation between the constituent beamlets is low, corresponding to small cross-scintillation terms σ_{mn}^2 in Eq. (4.0.1). On the other hand, the significant scintillation increase of pseudo-Bessel correlated beams in the low coherence regime is due to low received intensity at the detector, namely the small denominator in Eq. (4.0.1). By utilizing the self-bending property of Airy beams, both low intensity correlation and high received intensity are possible, and the overall scintillation of Airy beam arrays can be significantly reduced. Besides these two kinds of methods, a

third method for scintillation reduction can be found from Eq. (4.0.1), which is to use beamlets with small *self* scintillation indices σ^2_{mm}. This is the topic to be investigated in this chapter.

4.1 Scintillation of Nonuniformly Polarized Beams in Atmospheric Turbulence

Scintillation properties of various beam types, including cosh-Gaussian, Bessel-Gaussian, and annular beams, have been studied recently (see Ref. [27] for details). It has been shown that scintillations strongly depend on the initial beam properties, such as beam intensity profile and phase. In some specific atmospheric propagation scenarios, these different beam types can have lower scintillation than their comparable Gaussian beams. However, due to the complicated nature of the turbulence-induced beam scintillation, it is difficult to find guidelines for scintillation reduction by manipulating initial beam parameters. So far, most of these studies deal with scalar beam types. However, real optical beams are always vectorial, and in general may be represented as the coherent superposition of a pair of orthogonally polarized spatial modes[1]. It is well-known that fields which are generated by partially coherent and partially polarized sources can have a significant change in their degree and state of polarization on propagation through turbulence [112]. Furthermore, recent research has demonstrated that a partially coherent and partially polarized field will have lower scintillation than a comparable, linearly polarized field [113].

The previously mentioned research considered fields which possessed a spatially

[1]Even for a linearly polarized beam, it can also be formally decomposed to two orthogonally polarized modes, one with zero amplitude.

uniform state and degree of polarization. However, nonuniformly polarized beams such as radially and azimuthally polarized beams have been shown to be extremely useful in focusing applications [114], and recently the propagation behavior of such beams in turbulence has been studied [26, 115, 116]. Because depolarization effects are negligible when an optical beam propagates in turbulence, the modes remain orthogonal over appreciable propagation distances. According to the Fresnel-Arago laws [13], the orthogonally polarized modes do not interfere with one another, and their respective interference patterns add by intensity. Therefore nonuniformly polarized beams effectively function as two-mode partially coherent beams and it is natural to expect comparable scintillation behavior.

4.1.1 Beam Model and Scintillation in Atmospheric Turbulence

As a typical example of nonuniformly polarized beams, radially and azimuthally polarized beams are the orthogonal superpositions of Hermite-Gauss modes of order $n = 0, m = 1$ and $n = 1, m = 0$ (HG_{01} and HG_{10}) [117]. They have donut shaped intensity profiles in free space propagation. Although their on-axis intensity null disappears in turbulence propagation [26], the intensity received by an on-axis detector is relatively low. As shown by Fig. 4.1, the corresponding intensity fluctuation is high[2]. Here, a different monochromatic, nonuniformly polarized beam is considered. It consists of a coherent superposition of an x-polarized Laguerre-Gauss beam of order $n = 0$, $m = 0$ (LG_{00}), which has the following form in

[2]Although Ref. [116] reported scintillation reduction by radially polarized beams, this is due to the aperture averaging effect since an annular detector model was used. The result shown in Fig. 4.1 is based on the point detector model.

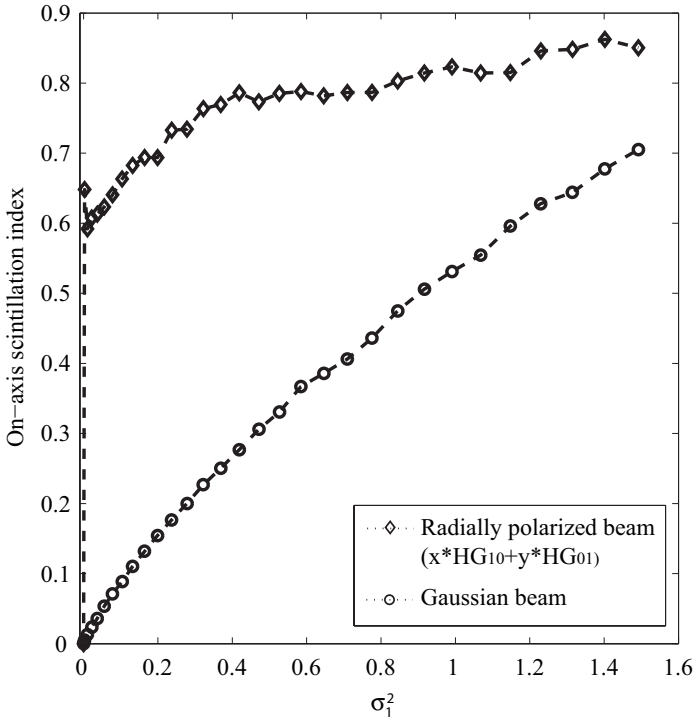

Figure 4.1: The scintillation of radially polarized beam as a function of the Rytov variance $\sigma_1^2 = 1.23 C_n^2 k^{7/6} L^{11/6}$. Here the wavelength is taken to be $\lambda = 1.55\,\mu$m, the turbulence strength $C_n^2 = 10^{-14}$ m$^{-2/3}$ and the width of the beam is taken to be $w_0 = 0.05$ m.

the plane $L = 0$,

$$U_{00}(x,y) = E_{0x}\sqrt{\frac{2}{\pi w_0^2}}\exp\left(-\frac{x^2+y^2}{w_0^2}\right), \tag{4.1.1}$$

and a y-polarized Laguerre-Gauss beam of order $n = 0$, $m = 1$ (LG_{01}) [10, Chapter 4], which in the plane $L = 0$ takes on the form

$$U_{01}(x,y) = E_{0y}\frac{2}{\sqrt{\pi} w_0^2}(x+iy)\exp\left(-\frac{x^2+y^2}{w_0^2}\right). \tag{4.1.2}$$

E_{0x} and E_{0y} are the amplitude of these two modes respectively. The modes are normalized such that

$$\int\int |U_{mn}(x,y)|^2 dxdy = 1, \tag{4.1.3}$$

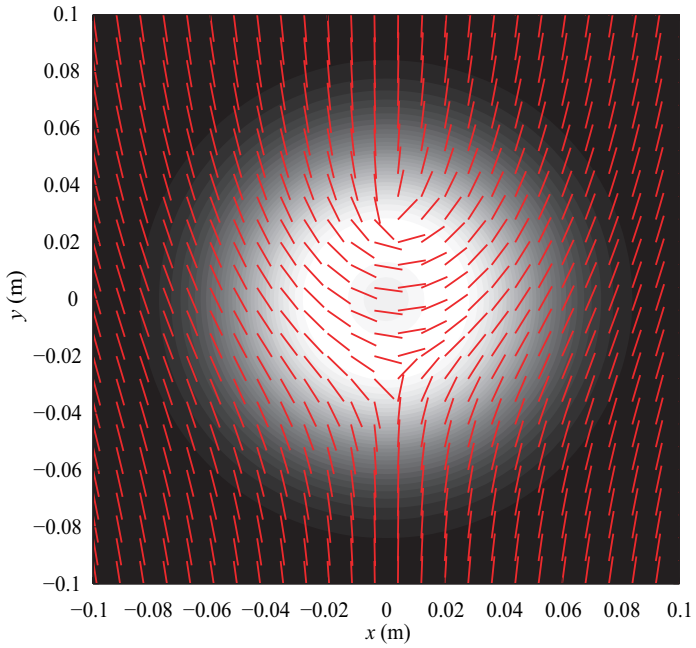

Figure 4.2: Major axis of polarization (red bars) and the corresponding intensity pattern (greyscale) of the wavefield in the source plane $z = 0$. Here the wavelength is taken to be $\lambda = 1.55\,\mu$m, the turbulence strength $C_n^2 = 10^{-14}$ m$^{-2/3}$ and the width of the beam is taken to be $w_0 = 0.05$ m. $E_{0x} = E_{0y} = 1$V/ m.

where the integration extends over the entire source plane. Fig. 4.2 illustrates the major axis of polarization of the wavefield in the source plane $z = 0$. It can be seen that the orientation of these axes are location-dependent. Therefore, these kinds of beams are referred as nonuniformly polarized beams.

The turbulence propagation of such beams is simulated by using the multiple random phase screen method. The two modes are propagated through the same realization of turbulence and their intensities are added at the detector plane. Here the amplitudes of the two modes act as weight of modes in the vectorial beam, while the atmospheric propagation properties of the beam depends on them. Fig. 4.3 illustrates the on-axis scintillation index of such beams as a function of the amplitude of the LG_{01} mode E_{0y}. The amplitude of LG_{01} mode E_{0x} is taken to be

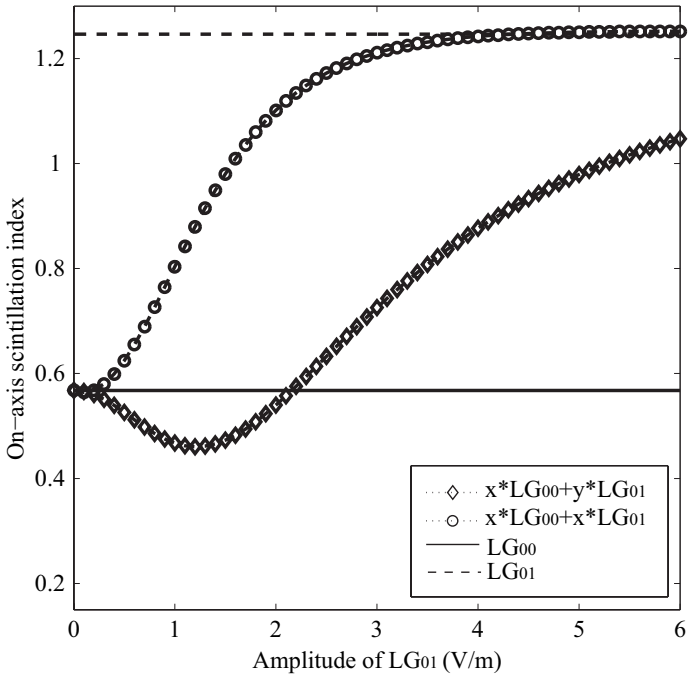

Figure 4.3: Simulation of the scintillation index of beams of different structure on propagation through 2.5 km of turbulence. Here the wavelength is taken to be $\lambda = 1.55\,\mu$m, the turbulence strength $C_n^2 = 10^{-14}$ m$^{-2/3}$ and the width of the beam is taken to be $w_0 = 0.05$ m.

1V/ m. The wavelength is taken to be $\lambda = 1.55\,\mu$m, the turbulence strength $C_n^2 = 10^{-14}$ m$^{-2/3}$, the propagation distance $L = 2.5$ km, and the width of the beam is taken to be $w_0 = 0.05$ m. For comparison, the scintillation index is also shown for the modes individually, and for the modes superimposed with the same polarization state. It can be seen that a minimum of the scintillation occurs when the amplitude of the LG_{01} mode is about 1.2V/ m, providing a 18% reduction as compared to the scintillation of the Gaussian beam alone. Fig. 4.4 illustrates the scintillation index of the same four beams, as a function of the Rytov variance [Eq. (2.3.7)]. It can be seen that the nonuniformly polarized field outperforms the individual modes as well as the combination of the modes with the same polarization.

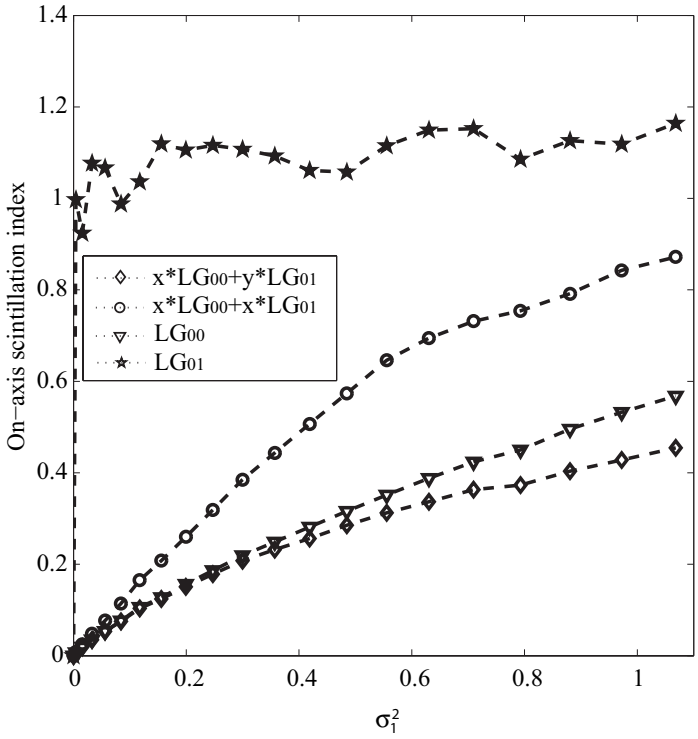

Figure 4.4: The scintillation of beams of different mode structure as a function of the Rytov variance $\sigma_1^2 = 1.23C_n^2k^{7/6}L^{11/6}$. For the simulations, the wavelength is taken to be $\lambda = 1.55\,\mu$m, the turbulence strength $C_n^2 = 10^{-14}$ m$^{-2/3}$ and the width of the beam is taken to be $w_0 = 0.05$ m.$E_{0x} = 1$V/ m and $E_{0y} = 1.21$V/ m.

Fig. 4.5 illustrates the variation of the on-axis scintillation index of the nonuniformly polarized beam as a function of the amplitude of LG_{01} modes E_{0y} for a propagation distance $L = 5$ km. A feature similar to that of Fig. 4.3 can be observed, where a 33% reduction compared to the scintillation of the Gaussian beam is obtained when the amplitude of the LG_{01} mode is 1.26V/ m. This result shows that the optimal amplitude ratio depends on the specific atmospheric propagation parameters.

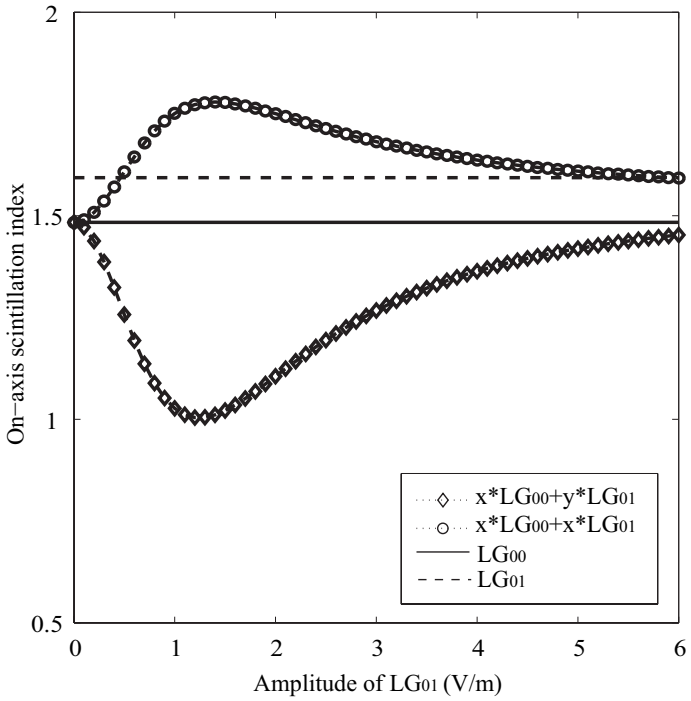

Figure 4.5: Simulation of the scintillation index of beams of different structure on propagation through 5 km of turbulence. Here the wavelength is taken to be $\lambda = 1.55\,\mu$m, the turbulence strength $C_n^2 = 10^{-14}$ m$^{-2/3}$ and the width of the beam is taken to be $w_0 = 0.05$ m.

4.1.2 Optimization of Nonuniformly Polarized Beams for Scintillation Reduction

In Sec. 4.1.1, a simple superposition of a LG_{00} and LG_{01} mode is used to generate a nonuniformly polarized beam. By choosing an appropriate amplitude ratio of the two orthogonally polarized modes, the beam scintillation is reduced compared to the comparable Gaussian beam. This scintillation reduction by nonuniformly polarization effect can be explained by the following straightforward mathematical proof.

The scintillation index of an electromagnetic beam is given by [113]

$$\sigma^2 = \frac{\langle I_x\rangle\sigma_{xx}^2 + 2\langle I_x\rangle\langle I_y\rangle\sigma_{xy}^2 + \langle I_x\rangle\sigma_{yy}^2}{\left(\langle I_x\rangle + \langle I_y\rangle\right)^2}, \tag{4.1.4}$$

where the argument $(\boldsymbol{\rho}, L)$ is omitted for brevity again. The quantities σ_{xx}^2 and σ_{yy}^2

denote the self scintillation indices of the x and y polarized modes respectively, while σ_{xy}^2 is the cross scintillation index between them. Their mathematical expression are the same as Eq. (3.2.13). Now Eq. (4.1.4) is rewritten as a function of the amplitude of LG_{01} mode explicitly (E_{0x} is unity.)

$$\sigma^2 = \frac{\langle I_x\rangle\sigma_{xx}^2 + 2E_{0y}^2\langle I_x\rangle\langle I_y\rangle\sigma_{xy}^2 + E_{0y}^4\langle I_x\rangle\sigma_{yy}^2}{\left(\langle I_x\rangle + E_{0y}^2\langle I_y\rangle\right)^2}. \tag{4.1.5}$$

Following the standard method to calculate the minimum value of a function, it can be shown that an electromagnetic beam has an minimum scintillation index given by

$$\sigma_{min}^2 = \begin{cases} \frac{\sigma_{xx}^2\sigma_{yy}^2-(\sigma_{xy}^2)^2}{\sigma_{xx}^2+\sigma_{yy}^2-2\sigma_{xy}^2} & \text{if } \sigma_{xy}^2 < \min[\sigma_{xx}^2, \sigma_{yy}^2] \\ \\ \min[\sigma_{xx}^2, \sigma_{yy}^2] & \text{otherwise} \end{cases}, \tag{4.1.6}$$

when

$$E_{0y} = \sqrt{\frac{\langle I_x\rangle(\sigma_{xx}^2 - \sigma_{xy}^2)}{\langle I_y\rangle(\sigma_{yy}^2 - \sigma_{xy}^2)}} \quad \text{if } \sigma_{xy}^2 < \min[\sigma_{xx}^2, \sigma_{yy}^2]. \tag{4.1.7}$$

From Eq. (4.1.6), it can be seen that the existence of the minimum scintillation of a nonuniformly polarized beam is because its two orthogonally polarized modes have different scintillation properties on propagation through the turbulence. For the propagation parameters used in Fig. 4.3, the simulated on-axis self scintillation indices of LG_{00} and LG_{01} are $\sigma_{xx}^2 = 0.5815$ and $\sigma_{yy}^2 = 1.2773$. The corresponding value of on-axis cross scintillation index is $\sigma_{xy}^2 = 0.2147$. The corresponding correlation coefficient between the intensity fluctuations of these two modes is $\rho_{I_x,I_y} = 0.2491$,

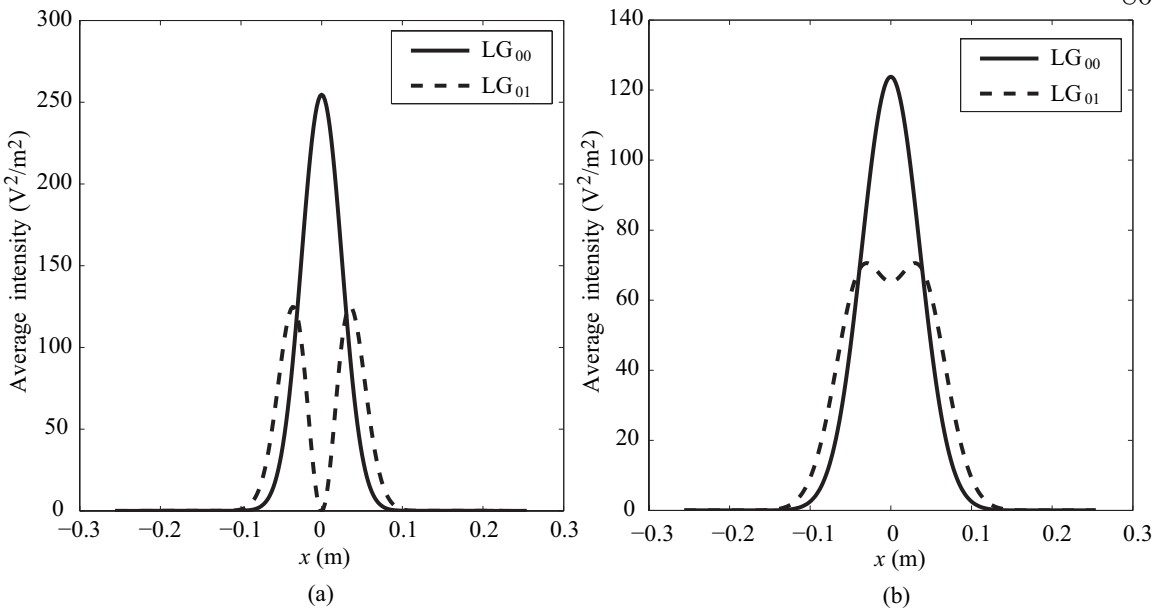

Figure 4.6: Average intensity profiles of the LG_{00} and LG_{01} modes on the source plane $z = 0$ (a) and the detector plane $z = 2.5$ km (b). The parameters are the same as in Fig. 4.4.

which is calculated by the following equation

$$\begin{aligned} \rho_{I_x,I_y} &= \frac{\langle I_x - \langle I_x\rangle\rangle\langle I_y - \langle I_y\rangle\rangle}{\sqrt{\langle I_x^2\rangle - \langle I_x\rangle^2}\sqrt{\langle I_y^2\rangle - \langle I_y\rangle^2}} \\ &= \frac{\sigma_{xy}^2}{\sqrt{\sigma_{xx}^2\sigma_{yy}^2}}. \end{aligned} \tag{4.1.8}$$

The correlation coefficient characterizes the statistical correlation between two random variables. Here the LG_{00} and LG_{01} modes have the same width parameter and propagate along the horizontal axis. However, the small value of their intensity correlation coefficient ($\rho_{I_x,I_y} = 0.2491$) shows that their intensity fluctuations have a low correlation even though they propagate through similar regions of turbulence.

This effect is possible because that the LG_{01} mode propagates through the turbulence in a different manner from the LG_{00} mode. In Fig. 4.6, an analytic

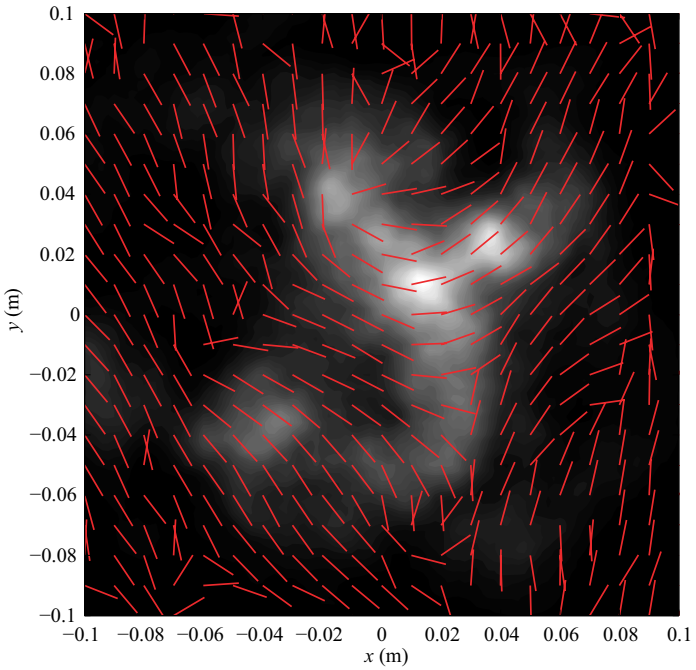

Figure 4.7: Major axis of polarization (red bars) and the corresponding intensity pattern (greyscale) of the wavefield in the detector plane $z = 2.5$ km. Here the wavelength is taken to be $\lambda = 1.55\,\mu$m, the turbulence strength $C_n^2 = 10^{-14}$ m$^{-2/3}$ and the width of the beam is taken to be $w_0 = 0.05$ m. $E_{0x} = E_{0y} = 1$V/ m.

calculation of the average intensity of these two modes is plotted using the extended Huygens-Fresnel principle with a quadratic phase approximation for the turbulence fluctuation. By comparison of the profiles on the source plane and the detector plane, it can be seen that the LG_{00} mode spreads on propagation in turbulence. On the contrary, the wavefield of the LG_{01} mode not only spreads outwardly but also moves inwardly. As a result, the initial doughnut profile gradually disappears on propagation in turbulence. The interference pattern produced by the LG_{01} mode is therefore different from that of the LG_{00} mode. Instead of the two modes producing a mutual interference pattern, the polarization of the field is scrambled; a realization of this, determined by numerical simulation, is shown in Fig. 4.7.

Now scintillation reduction by nonuniformly polarized beams can be understood

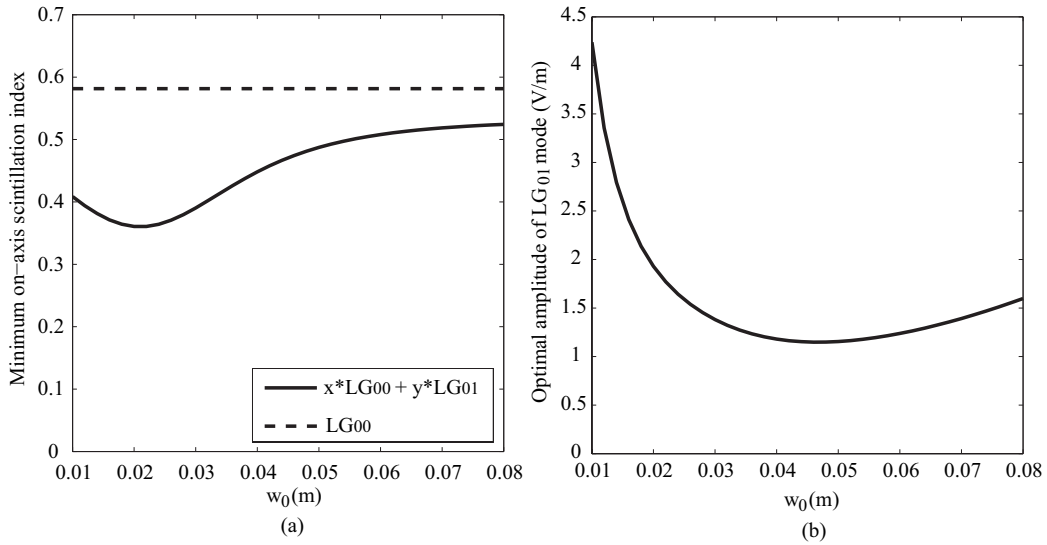

Figure 4.8: Minimum on-axis scintillation of a nonuniformly polarized beam as a function of the initial width of the LG_{01} mode (a). The optimal amplitude E_{0y} is shown in (b). $E_{0x} = 1$V/ m. The rest of the parameters are the same as in Fig. 4.2.

by noting that the orthogonally polarized modes have different transverse profiles and are therefore affected differently by the same turbulence. Since the turbulence propagation of a mode depends on its initial width, the scintillation properties of a nonuniformly polarized beam could be further optimized by varying the width of its modes. Fig. 4.8 illustrates the minimum on-axis scintillation index of a nonuniformly polarized beam as a function of the initial width of the LG_{01} mode. It can be seen that the on-axis scintillation could be further reduced from 18% to 38% when the width of the LG_{01} mode decreases from 5 cm to 2.2 cm. The variation of the intensity correlation coefficient ρ_{I_x,I_y} is illustrated in Fig. 4.9, which clearly shows that the correlation between the intensity fluctuations of these two modes strongly depends on the initial beam profiles and could be even as low as nearly zero when the width of the LG_{01} mode is around 1.5 cm.

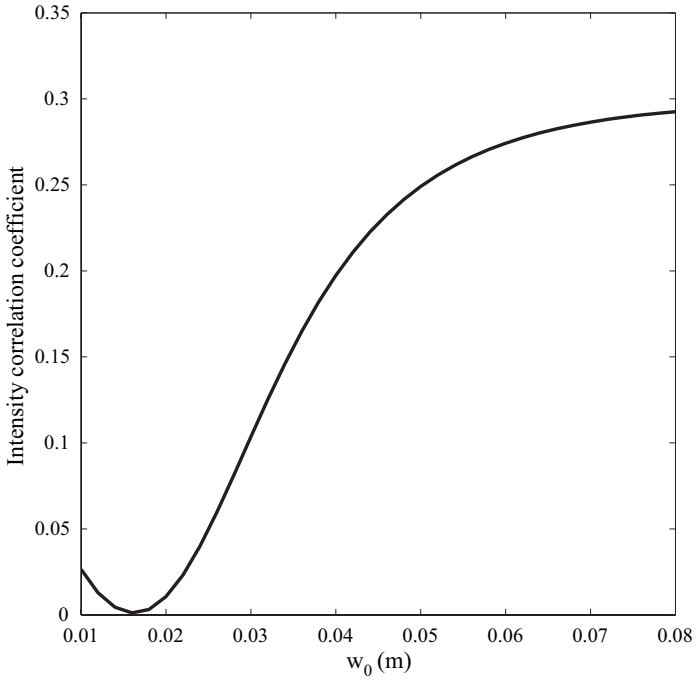

Figure 4.9: Intensity correlation coefficient ρ_{I_x,I_y} as a function of the initial width of the LG_{01} mode. The parameters are the same as in Fig. 4.8.

4.2 Scintillation of Nonuniformly Polarized Beam Arrays in Atmospheric Turbulence

In Sec. 4.1, it has been shown that the nonuniform polarization effect is a relatively easy and inexpensive way to reduce the scintillation of a coherent optical beam. Now optical elements to convert linear to nonuniform polarization are common. For instance, a radially polarized beam can be generated by use of a conical Brewster prism [118]. In this section, nonuniformly polarized beams are used as the beamlets of an incoherent beam array and its scintillation properties on propagation in the atmosphere is studied.

From Chapter 3, it is known that the key points for scintillation reduction by an incoherent beam array are diversity and high received intensity. However, the LG_{01} mode gradually evolves to a Gaussian profile on propagating in turbulence

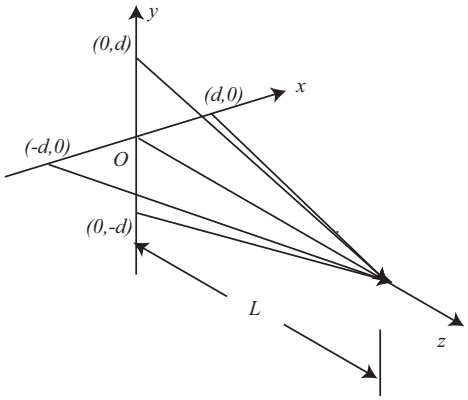

Figure 4.10: Illustration of a nonuniformly polarized beam array.

and a nonuniformly polarized beam eventually propagates along a straight line in turbulence. Therefore, the beamlets of a nonuniformly polarized beam array are inclined to overlap at the receiver plane. A 4-beamlet nonuniformly polarized beam array is defined where its beamlets take on the following form in the plane $z = 0$

$$U_{mx}(x,y) = E_{0x}\sqrt{\frac{2}{\pi w_{0x}^2}}\exp\left[-\frac{(x-d_{mx})^2+(y-d_{my})^2}{w_{0x}^2}\right]\exp\left[-i\left(k_{mx}x+k_{my}y\right)\right], \tag{4.2.1a}$$

$$\begin{aligned} U_{my}(x,y) &= E_{0y}\frac{2}{\sqrt{\pi}w_{0y}^2}\left[(x-d_{mx})+i\left(y-d_{my}\right)\right]\exp\left[-\frac{(x-d_{mx})^2+(y-d_{my})^2}{w_{0y}^2}\right] \\ &\times \exp\left[-i\left(k_{mx}x+k_{my}y\right)\right], \end{aligned} \tag{4.2.1b}$$

where m $= 1, 2, 3, 4$ labels the mth beamlet. The configuration of this beam array is illustrated in Fig. 4.10. Each beamlet is located at (d_{mx}, d_{my}) on the source plane. The corresponding off-axis distance is $d = \sqrt{d_{mx}^2 + d_{my}^2}$. (k_{mx}, k_{my}) is the transverse wave vector. In order to make all beamlets overlap at the receiver plane $z = L$, $k_{mx} = kd_{mx}/L$ and $k_{my} = kd_{my}/L$.

Fig. 4.11 illustrates the on-axis scintillation index of a nonuniformly polarized

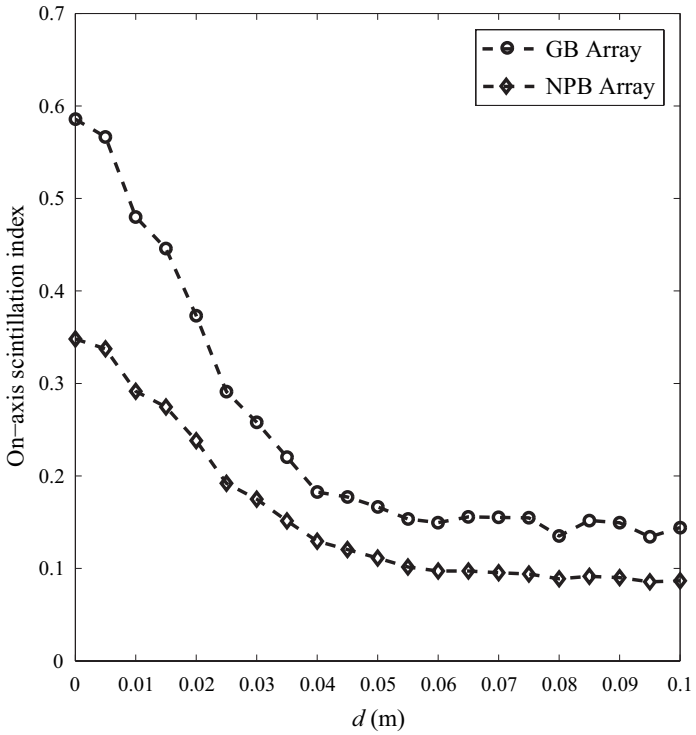

Figure 4.11: On-axis scintillation of a nonuniformly polarized beam (NPB) array as a function of the off-axis distance d. The on-axis scintillation of a Gaussian beam (GB) array is shown as well. $w_{0x} = 5$ cm, $w_{0y} = 2.2$ cm, $E_{0x} = 1$V/ m, and $E_{0y} = 1.8$V/ m. The rest of the parameters are the same as in Fig. 4.2.

beam array as a function of the off-axis distance d after propagating in turbulence for 2.5 km. The parameters of beamlets are optimized based on the results in Sec. 4.1.2. The on-axis scintillation of a 4-beamlet Gaussian beam array is also shown for comparison, whose beamlets take the form of Eq. (4.2.1a). It can be seen that by using beamlets of small scintillation, the nonuniformly polarized beam array has lower scintillation than a comparable Gaussian beam array. When $d = 0.1$ m, the on-axis scintillation of the nonuniformly polarized beam array is 61% of the scintillation index of the Gaussian beam array. In addition, as the off-axis distance d increases, the scintillation of the nonuniformly polarized beam array gradually decreases and 75% reduction, the theoretical maximum reduction of a 4-beamlet incoherent beam

array, is eventually reached.

4.3 Summary

It has been demonstrated that an appropriately chosen nonuniformly polarized beam can have appreciably smaller scintillation than comparable beams of uniform polarization. This results from the fact that a nonuniformly polarized field acts as an effective two-mode partially coherent field. In Chapter 3, it has shown that spatial or directional diversity of beamlets are crucial for scintillation reduction by partially coherent beams. The results obtained in this chapter suggest another kind of diversity, modal diversity. Modes of different transverse profiles propagate through the atmosphere in different manners and therefore their own intensity fluctuations are less correlated. Here a simple superposition of LG_{00} and LG_{01} modes is used. However, nonuniformly polarized beams could be combinations of other mode types, such as higher order Laguerre-Gauss modes. The guideline that the turbulence-induced intensity fluctuations should have a low correlation should be followed when selecting mode pairs.

Now it is known that low intensity correlation between beamlets or orthogonally polarized modes is necessary for scintillation reduction by incoherent beam arrays or nonuniformly polarized beams. It has been shown that a complete lack of correlation can be achieved by either sufficient spatial separation of beamlets or appropriately chosen orthogonal modes. However, by examining the expression of the minimum scintillation index of a nonuniformly polarized beam [Eq. (4.1.6)], it can be found that σ_{min}^2 decreases monotonically as σ_{xy}^2 decreases from 0 to be

negative and reaches its mathematical minimum 0 when $\sigma_{xy}^2 = -\sqrt{\sigma_{xx}^2\sigma_{yy}^2}$. The negative cross scintillation index means the negative correlation between intensity fluctuations of two orthogonally polarized modes, while the value $\sigma_{xy}^2 = -\sqrt{\sigma_{xx}^2\sigma_{yy}^2}$ corresponds to the situation of full anti-correlation since the corresponding intensity correlation coefficient ρ_{I_x,I_y} is -1. Now, the existing methods can only reduce the intensity correlation between beamlets or modes to as much as zero. Therefore, this observation suggests that beam scintillation might be further reduced by exploring methods to make beamlets or modes negatively correlated on propagation in the atmosphere.

CHAPTER 5: MEASUREMENT OF ATMOSPHERIC TURBULENCE STRENGTH BY VORTEX BEAMS

It is now well-known that, due to the turbulence-induced random phase modulation, optical beams are distorted on propagation through the atmosphere. Therefore the performance of a long-range optical system operating in the atmosphere strongly depends upon the turbulence characteristics. In particular, the refractive index structure constant C_n^2, which characterizes the turbulence strength, also dictates the strength of scintillations. As it has been noted, this scintillation is the primary limitation in the development of free-space optical communication systems. It has been demonstrated scintillation reduction by incoherent beam arrays and nonuniformly polarized beams in Chapters 3 and 4. However, the techniques described for minimizing scintillation requires knowledge of the value of C_n^2, which must be measured independently for an optimal solution.

The traditional method to measure C_n^2 is to use an optical scintillometer [119–121]. By measuring the scintillation of a wavefield over a short propagation distance, the path-averaged value of C_n^2 is obtained. However, recent studies on the behavior of spatial correlation singularities carried by vortex beams suggest an alternate solution.

Vortex beams are optical beams that possess an intensity null along their propagation axis and hence have a singular phase structure on that axis. The study of such 'singular' regions of optical wavefields has developed into a subfield of optics

in its own right, now known as *singular optics* [122]. The original studies of singular optics, such as the pioneering work of Nye and Berry [123], investigated regions where the amplitude of coherent wavefields vanish, and hence the phase is undefined. They demonstrated that the zero manifolds of a wavefield are typically lines in three-dimensional space, around which the phase has a circulating or helical structure, now referred to as an *optical vortex*. Such vortices have many interesting and useful properties, including a conserved, discrete *topological charge*, and a consequent stability on propagation, as well as a relationship to the orbital angular momentum of the wavefield [74].

However, an initially coherent vortex beam becomes partially coherent on propagation in the atmosphere and therefore its vortex phase structure is ill defined on average. More recently, the study of phase singularities has been extended to account for partially coherent wavefields. It has been demonstrated that spatial correlation functions of partially coherent wavefields may also carry phase singularities [124–127]. These singular structures are pairs of points at which the wavefield are uncorrelated, now referred to as *spatial correlation singularities* or *coherence vortices*. It has been shown that they are robust as the coherence of a wavefield decreases [126]. Therefore it suggests a possible use of spatial correlation singularities in turbulence applications.

In this chapter, the feasibility of use of spatial correlation singularities for atmospheric turbulence strength measurement is theoretically investigated. It is started by reviewing the basic properties of optical vortices and coherence vortices

in Sec. 5.1. The break-up of a higher-order optical vortex into first-order coherence vortices in the presence of perturbations is investigated in Sec. 5.2. From the result of Sec. 5.2, a method to measure atmospheric turbulence strength by using a vortex beam is proposed in Sec. 5.3.

5.1 Optical Vortices and Coherence Vortices

A monochromatic scalar wavefield $U(\mathbf{r}, t)$ is of the following form

$$U(\mathbf{r}, t) = U(\mathbf{r})e^{-i\omega t}, \tag{5.1.1}$$

where ω denotes frequency. The space-dependent part $U(\mathbf{r})$ can be rewritten in a factorized form

$$U(\mathbf{r}) = A(\mathbf{r})e^{i\phi(\mathbf{r})}, \tag{5.1.2}$$

where $A(\mathbf{r})$ denotes amplitude and $\phi(\mathbf{r})$ denotes phase. If the field amplitude vanishes ($A(\mathbf{r}) = 0$) in certain regions of space, the phase can take on any value in those regions and is therefore undefined, or *singular*. Research over the past few decades has demonstrated that the zeros typically manifest as lines in three dimensional space, around which the phase has a circulating or helical structure [122]. These optical vortices have associated with them a discrete topological charge s, defined as

$$s = \frac{1}{2\pi} \oint_C \nabla\phi \cdot d\mathbf{r}, \tag{5.1.3}$$

where the path C is taken along a closed counterclockwise path enclosing the singularity. The topological charge takes on integer values and is a conserved quantity.

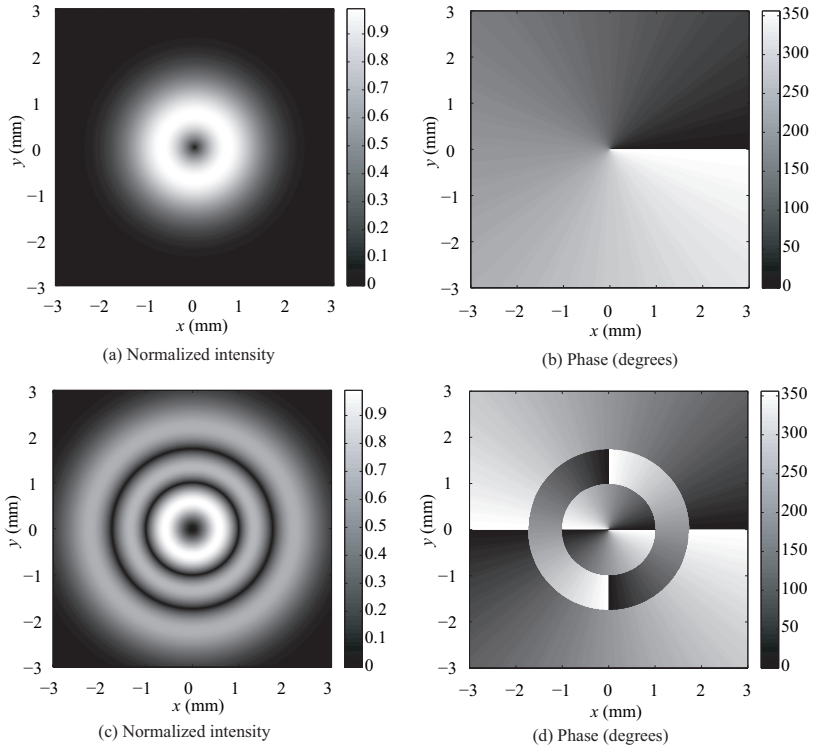

Figure 5.1: Illustration of the transverse profile and phase structure of a pair of Laguerre-Gauss beams: $n = 0$, $m = 1$: (a) intensity, (b) phase, $n = 2$, $m = 2$: (c) intensity (d) phase.

A familiar collection of beams which possess an optical vortex in their center are the Laguerre-Gauss solutions to the paraxial wave equation [10, chapter 4]

$$\begin{aligned} U_{nm}(\rho,\phi,z) &= C_{nm}\left(\frac{\sqrt{2}\rho}{W(z)}\right)^{m} L_n^{(m)}\left(\frac{2\rho^2}{W^2(z)}\right)\exp\left[i(2n+m+1)\varphi(z)\right] \\ &\times \exp\left(im\phi - \rho^2/W^2(z) - ik\rho^2/2F(z)\right), \end{aligned} \tag{5.1.4}$$

where (ρ,ϕ,z) are the cylinder coordinates in space, C_{mn} is a normalization constant and $L_n^{(m)}$ are the Laguerre polynomials of order m and n [128]. $W(z)$ is the beam width on the transverse plane z, defined as

$$W(z) = w_0\sqrt{1+\left(\frac{z}{z_R}\right)^2}, \tag{5.1.5}$$

where w_0 is the beam width at the waist plane $z = 0$ and $z_R = \frac{\pi w_0^2}{\lambda}$ is the *Rayleigh range*. $F(z)$ is the radius of curvature of wavefront on the transverse plane z, defined as

$$F(z) = z\left[1 + \left(\frac{z_R}{z}\right)^2\right]. \tag{5.1.6}$$

$\varphi(z)$ is the longitudinal phase delay on the transverse plane z, also known as the Gouy phase, defined as

$$\varphi(z) = \arctan\left(\frac{z}{z_R}\right). \tag{5.1.7}$$

Fig. 5.1 illustrates several low-order Laguerre-Gauss beams. The central core of the beam possesses an amplitude zero, and the phase of the field increases by a multiple m of 2π as one progresses around the central core. m is referred to as the *order* of the vortex core which is also the topological charge. In Fig. 5.1 the vortex phase structures are illustrated by phase maps. However, a phase plot consisting of a finite number of equiphase lines is usually sufficient to describe the location and topological charge of field vortices. Fig. 5.2 shows an example of the equiphase lines for the phase structure illustrated in Fig. 5.1b. The intersection of the four equiphase lines indicates the vortex position. Four equiphase lines are used in all figures of this chapter.

When such a vortex beam is randomized, intensity nulls are usually removed. However the vortex properties can survive in the spatial coherence of the wavefield [126, 129]. The coherence properties of a statistically stationary scalar wavefield are characterized by the cross-spectral density, which may always be expressed as the average of an ensemble of monochromatic realizations of field [see

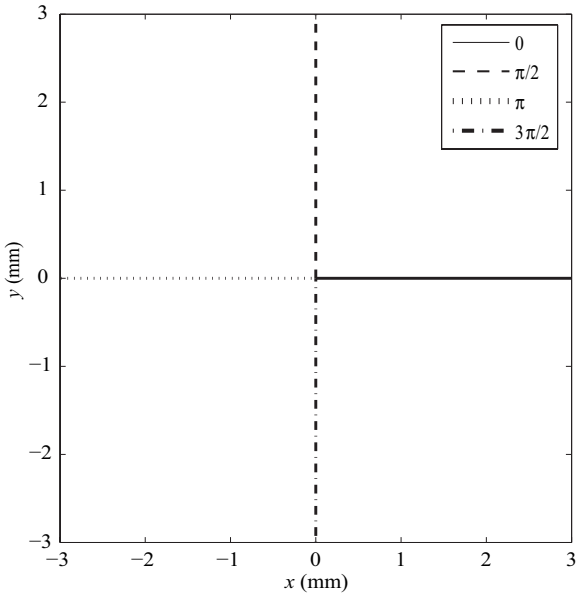

Figure 5.2: Illustration of the equiphase contours of Laguerre-Gauss beam of the order $n = 0$, $m = 1$.

Eq. (2.1.5) in Sec. 2.1]

$$W(\mathbf{r}_1, \mathbf{r}_2) = \langle U(\mathbf{r}_1) U^*(\mathbf{r}_2) \rangle. \tag{5.1.8}$$

Coherence vortices are referred to as the singularities of the cross-spectral density, namely the zeros of $W(\mathbf{r}_1, \mathbf{r}_2)$. Eq. (5.1.8) will be used below to construct a model of a quasi-monochromatic, partially coherent field with a 'built-in' vortex behavior.

To study the relationship between optical vortices and coherence vortices, a 'beam wander' model first developed in Ref. [129] is used. An ensemble of monochromatic fields $U(\boldsymbol{\rho} - \boldsymbol{\rho}_0)$ is considered in the source plane $z = 0$, with $\mathbf{r} \equiv (\boldsymbol{\rho}, z)$. Each member of the ensemble is centered on a transverse location $\boldsymbol{\rho}_0$, which is a random variable of the transverse location. $f(\boldsymbol{\rho}_0)$ is the corresponding probability density, which dictates the coherence properties of the generated partially coherent field. The cross-spectral

density is then given by

$$W(\boldsymbol{\rho}_1, \boldsymbol{\rho}_2) = \int U(\boldsymbol{\rho}_1 - \boldsymbol{\rho}_0) U^*(\boldsymbol{\rho}_2 - \boldsymbol{\rho}_0) f(\boldsymbol{\rho}_0) d^2\rho_0, \tag{5.1.9}$$

where the integral, representing the ensemble average, is taken in the source plane of the field. This construction may be taken as a simple model of beam wander in atmospheric turbulence [10, Chapter 6]. This construction was used previously to study the behavior of a partially coherent field created with an $n = 0$, $m = 1$ vortex beam, as the degree of coherence is changed [129]. It was also demonstrated that the construction produces results consistent with the general behavior of vortices in partially coherent fields [130].

5.2 Breakup of Second-order Optical Vortex to Two First-order Coherence Vortices

Recently the propagation of an optical vortex beam through atmospheric turbulence was studied [77]. It has been shown that on propagation, a high-order optical vortex breaks down into a collection of first-order optical vortices, though the total topological charge is conserved. If the field is averaged over times long compared to the fluctuations of the medium, one readily finds that the spatial coherence of a beam decreases on propagation [10]. Consequently, the optical vortices are converted into coherence vortices. It is natural to ask whether an mth-order optical vortex is replaced with an mth-order coherence vortex when the spatial coherence of the field decreases, or whether a number of lower-order coherence vortices are produced.

A Laguerre-Gauss beam of order $n = 0$ and $m = 2$ possesses a second-order optical

vortex in its center. Its transverse profile in the source plane is

$$U_{02}(\rho,\phi) = C_{02}\left(\frac{\sqrt{2}\rho}{w_0}\right)^2 \exp(2i\phi)\exp(-\rho^2/w_0^2), \tag{5.2.1}$$

where w_0 is the beam width in the source plane, and $\boldsymbol{\rho} \equiv (\rho,\phi)$. With beam wander model, the topological structure of the corresponding coherence vortex can be studied by substituting Eq. (5.2.1) into Eq. (5.1.9). Here for the purpose of illustration, the probability density $f(\boldsymbol{\rho}_0)$ in Eq. (5.1.9) is taken to be Gaussian[1]

$$f(\boldsymbol{\rho}_0) = \frac{1}{\sqrt{\pi}\delta} e^{-\rho_0^2/\delta^2}, \tag{5.2.2}$$

where the quantity δ represents the average beam wander, and also restrict ourselves to a single frequency ω. For simplicity, further expression of the frequency ω will be suppressed. In the limit $\delta \to 0$, the beam does not wander and is therefore fully coherent. Increasing δ represents a decrease in spatial coherence.

As the cross-spectral density $W(\boldsymbol{\rho}_1,\boldsymbol{\rho}_2)$ contains two variables, $\boldsymbol{\rho}_1$ is taken to be fixed and behavior of $W(\boldsymbol{\rho}_1,\boldsymbol{\rho}_2)$ is studied as a function of $\boldsymbol{\rho}_2$. Here $\boldsymbol{\rho}_1$ and $\boldsymbol{\rho}_2$ are referred to as the reference point and the observation point respectively. Two examples of these coherence vortices are shown in Fig. 5.3. In both cases *four* first-order coherence vortices are observed. Two of these (the left-most in both figures) are first-order coherence vortices of the same sign which result from the break-up of the second-order optical vortex. Evidently no choice of reference point or state of coherence (other than complete coherence) will maintain a pure second-order vortex,

[1]In Sec. 5.3, it will be shown that the turbulence effects can be approximated by a Gaussian function when the cross-spectral density of a wavefield in the atmosphere is studied [Eq. (5.3.12)].

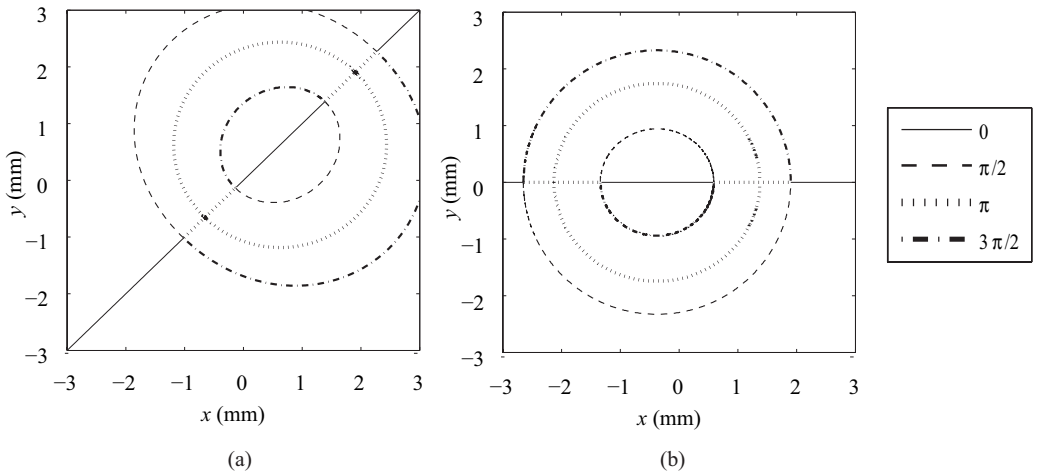

Figure 5.3: Equal phase contours of the cross-spectral density, with the reference point at (a) $(0.5 \text{ mm}, 0.5 \text{ mm})$, and (b) $(-0.3 \text{ mm}, 0)$. In both plots, $w_0 = 1$ mm and $\delta = 1$ mm.

i.e. the second-order optical vortex is unstable under changes in the state of coherence. The other two coherence vortices in each figure (the right-most) are of opposite sign from the first pair.

Fig. 5.4 illustrates the dependence of coherence vortices structure on parameter δ. It can be readily seen that, as $\delta \to 0$, i.e. as the field becomes fully coherent, the left-most coherence vortices merge and become the second-order optical vortex. It can also be seen that the right-most coherence vortices recede to the point at infinity. This observation shows that they are singularities which are 'hidden' at the point at infinity when the field is fully coherent. A similar behavior is seen for a first-order optical vortex, which has been shown to have an opposite vortex 'hidden' at infinity [129].

In our 'beam wander' model [Eq. (5.2.2)], δ characterizes the strength of perturbations. Strong perturbations correspond to large range of wander, namely

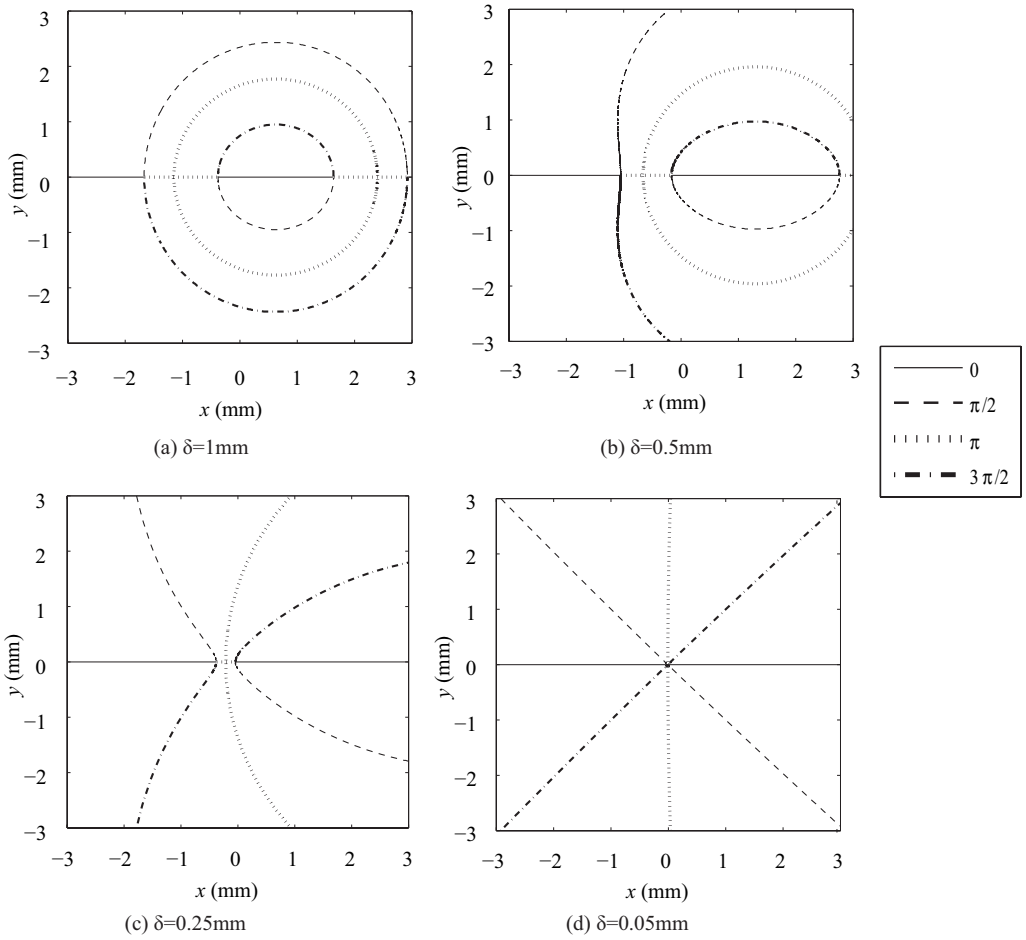

Figure 5.4: Illustration of the relationship between a second-order optical vortex and a pair of first-order correlation vortices. The reference point is at $(0.5\text{ mm}, 0)$ and $w_0 = 1$ mm.

large δ. It can be seen from Fig. 5.4 that the separation of the first-order coherence vortices is directly related to δ. Fig. 5.5 illustrates the separation of the two vortices (the left-most in Fig. 5.4a) as a function of δ. the separation increases monotonically with δ, eventually saturating at a finite value. This observation raises the possibility that this 'splitting' could be used as a simple measure of either the spatial coherence properties of a partially coherent field or, indirectly, the strength of a turbulent medium which the vortex beam has passed through.

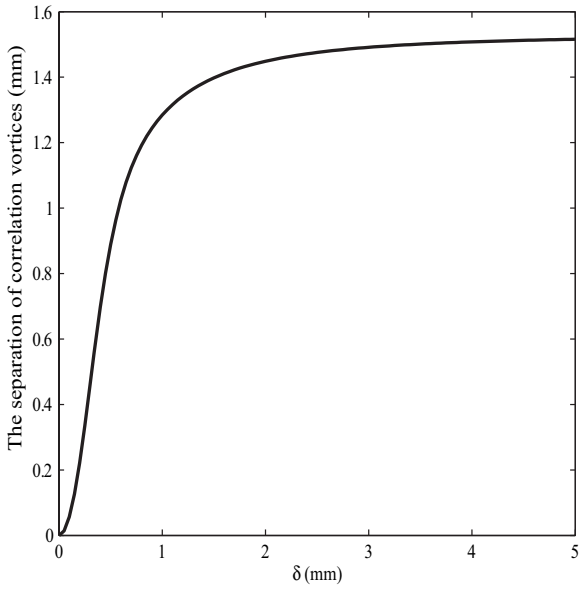

Figure 5.5: Illustration of the dependence of the correlation vortices separation on the average beam wander parameter δ. The reference point is at $(0.5\text{ mm}, 0)$ and $w_0 = 1$ mm.

5.3 Atmospheric Turbulence Strength Measurement by Vortex Beams

In Sec. 5.2, it has been shown that a second-order optical vortex is unstable under perturbations and breaks into a pair of first-order coherence vortices under a decrease of coherence. The dependence of the coherence vortex separation on the perturbation strength parameter δ suggests the possible use of coherence vortices as a probe of the statistical properties of random media. However, it is difficult to experimentally realize high-order Laguerre-Gauss beams which carry a high-order optical vortex. On the other side, the phase structure of the cross-spectral density corresponding to a second-order optical vortex contains four coherence vortices (Fig. 5.3) which are grouped as two pairs. Isolating one pair of them and measuring the separation is also challenging.

Recently another kind of coherence singularity was demonstrated [126, 127]. It has

been shown that a ring dislocation exists in the cross-correlation function of a partially coherent field when passed through a vortex mask and can be observed by a wavefront folding interferometer. Unlike coherence vortices which are the phase singularities of the cross-spectral density $W(\boldsymbol{\rho}_1, \boldsymbol{\rho}_2)$ as a function of the observation point $\boldsymbol{\rho}_2$, a ring dislocation is a collection of phase singularities of the cross-spectral density $W(\boldsymbol{\rho}_1, \boldsymbol{\rho}_2)$ while the reference point $\boldsymbol{\rho}_1$ and the observation point $\boldsymbol{\rho}_2$ are symmetric with respect to the origin, namely $\boldsymbol{\rho}_1 = -\boldsymbol{\rho}_2$. When the wavefield is rotationally symmetric, these singularities usually form a ring and therefore are referred to as a *ring dislocation*. More recently, the properties of the ring dislocation in the the presence of fluctuations and on propagation in free space were investigated [131, 132]. It is demonstrated that the radius of this ring dislocation is inversely related to coherence length of the wavefield. As spatial coherence decreases on propagation through turbulence, it suggests that a measurement of such a ring dislocation could be used as a measure of turbulence strength, namely C_n^2.

5.3.1 Theoretical Derivation

The propagation geometry is illustrated in Fig. 5.6. After passing through an idealized vortex mask at the transmitter plane, the incident Gaussian beam possesses a vortex phase structure. By using the extended Huygens-Fresnel principle [23], the transmitted field at the receiver plane $z = L$ (in the far-field regime) can be expressed

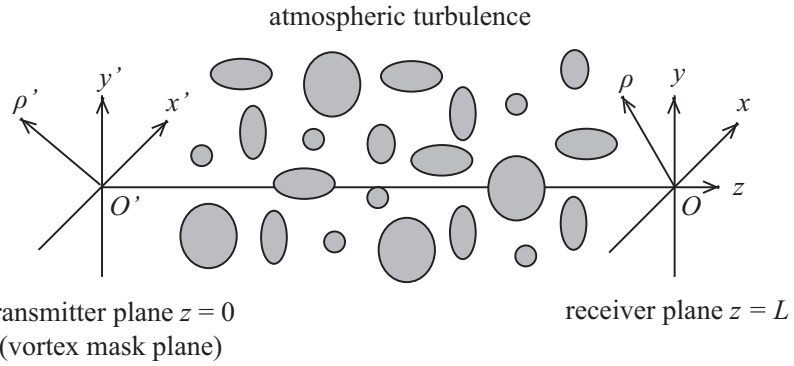

Figure 5.6: Illustration of the propagation geometry. The vortex mask of order 1 is placed at the transmitter plane $z = 0$. It imparts a phase factor $\exp(i\phi')$ to the incident Gaussian beam $U_0 = \exp(-\rho'^2/w_0^2)$. For simplicity, the waist plane of the Gaussian beam is also at the transmitter plane.

in the form

$$\begin{aligned} U(\boldsymbol{\rho}, L) &= -\frac{ik}{2\pi L}\exp\left(ikL + \frac{ik\rho^2}{2L}\right) \\ &\times \int U(\boldsymbol{\rho}', 0)\exp\left[-i2\pi\frac{\boldsymbol{\rho}}{\lambda L}\cdot\boldsymbol{\rho}' + \psi\left(\boldsymbol{\rho}, \boldsymbol{\rho}'\right)\right]d^2\rho', \end{aligned} \tag{5.3.1}$$

where $U(\boldsymbol{\rho}', 0) = \exp\left(-\rho'^2/w_0^2\right)\exp(i\phi')$ is the field at the transmitter plane, k is the wavenumber, w_0 is the beam width at the transmitter plane, and $\psi(\boldsymbol{\rho}, \boldsymbol{\rho}')$ is the random part of the complex phase of a spherical wave propagating in turbulence. Coherence properties of the field at the receiver plane are characterized by the cross-spectral density [see Eq. (2.1.5) in Sec. 2.1]

$$\begin{aligned} W(\boldsymbol{\rho}_1, \boldsymbol{\rho}_2, L) &= \langle U(\boldsymbol{\rho}_1, L)U^*(\boldsymbol{\rho}_2, L)\rangle \\ &= A\iint U(\boldsymbol{\rho}_1', 0)U^*(\boldsymbol{\rho}_2', 0)\exp\left[-i2\pi\left(\frac{\boldsymbol{\rho}_1\cdot\boldsymbol{\rho}_1' - \boldsymbol{\rho}_2\cdot\boldsymbol{\rho}_2'}{\lambda L}\right)\right] \\ &\times \langle\exp\left[\psi(\boldsymbol{\rho}_1, \boldsymbol{\rho}_1') + \psi^*(\boldsymbol{\rho}_2, \boldsymbol{\rho}_2')\right]\rangle d^2\rho_1' d^2\rho_2', \end{aligned} \tag{5.3.2}$$

where $A = (1/\lambda L)^2 \exp\left[-ik(\rho_2^2 - \rho_1^2)/(2L)\right]$, the asterisk indicates complex conjugation, and the angular brackets denote an ensemble average over the turbulence fluctuations. When turbulence is homogeneous, the random part of the complex phase of a spherical wave in Eq. (5.3.2) can be approximated by [see Eq. (2.3.49) in Sec. 2.3.3]

$$\begin{aligned} \langle \exp\left[\psi(\boldsymbol{\rho}_1, \boldsymbol{\rho}_1') + \psi^*(\boldsymbol{\rho}_2, \boldsymbol{\rho}_2')\right] \rangle &\approx \exp\left(-\frac{|\mathbf{r}|^2 + \mathbf{r}\cdot\mathbf{r}' + |\mathbf{r}'|^2}{\rho_0^2}\right) \\ &= T(\mathbf{r}', \mathbf{r}), \end{aligned} \tag{5.3.3}$$

where

$$\rho_0 = (0.55 C_n^2 k^2 L)^{-3/5} \tag{5.3.4}$$

is the coherence length of a spherical wave propagating in turbulence, $\mathbf{r} = \boldsymbol{\rho}_2 - \boldsymbol{\rho}_1$, $\mathbf{r}' = \boldsymbol{\rho}_2' - \boldsymbol{\rho}_1'$, and C_n^2 is the the refractive index structure constant. Here C_n^2 is assumed to be a constant over the propagation path. In Appendix B, it will be shown that ρ_0 can also represent a spatially-averaged value if C_n^2 is varying on propagation. With this approximation, the cross-spectral density at the receiver plane can be written as

$$\begin{aligned} W(\boldsymbol{\rho}_1, \boldsymbol{\rho}_2, L) &= A \iint U(\boldsymbol{\rho}_1', 0) U^*(\boldsymbol{\rho}_2', 0) T(\mathbf{r}', \mathbf{r}) \\ &\times \exp\left[-i2\pi\left(\frac{\boldsymbol{\rho}_1\cdot\boldsymbol{\rho}_1' - \boldsymbol{\rho}_2\cdot\boldsymbol{\rho}_2'}{\lambda L}\right)\right] d^2\rho_1' d^2\rho_2'. \end{aligned} \tag{5.3.5}$$

Eq. (5.3.5) may be expressed in a more suggestive form by using the following Fourier expansions,

$$T(\mathbf{r}', \mathbf{r}) = \int \tilde{T}(\boldsymbol{\kappa}, \mathbf{r}) \exp(i2\pi \mathbf{r}'\cdot\boldsymbol{\kappa}) d^2\kappa \tag{5.3.6}$$

$$U(\boldsymbol{\rho}_j', 0) = \int \tilde{U}(\boldsymbol{\kappa}_j, 0) \exp(i2\pi \boldsymbol{\rho}_j' \cdot \boldsymbol{\kappa}_j) d^2\kappa_j \quad (j = 1, 2). \tag{5.3.7}$$

On substituting Eqs. (5.3.6) and (5.3.7) into Eq. (5.3.5) and applying standard Fourier transform techniques, one can find that

$$W(\boldsymbol{\rho}_1, \boldsymbol{\rho}_2, L) = A \int \tilde{U}\left(\frac{\boldsymbol{\rho}_1}{\lambda L} - \boldsymbol{\kappa}, 0\right) \tilde{U}^*\left(\frac{\boldsymbol{\rho}_2}{\lambda L} - \boldsymbol{\kappa}, 0\right) \tilde{T}(\boldsymbol{\kappa}, \mathbf{r}) d^2\kappa, \tag{5.3.8}$$

where

$$\tilde{T}(\boldsymbol{\kappa}, \mathbf{r}) = \pi\rho_0^2 \exp(-\pi^2\rho_0^2\kappa^2) \exp\left(-\frac{3|\mathbf{r}|^2}{4\rho_0^2} + i\pi \mathbf{r} \cdot \boldsymbol{\kappa}\right) \tag{5.3.9}$$

$$\begin{aligned} \tilde{U}(\boldsymbol{\kappa}, 0) &= -\frac{i}{2}\pi^{5/2} w_0^3 \kappa \exp(i\theta) \exp\left(-\frac{1}{2}\pi^2 w_0^2 \kappa^2\right) \\ &\times \left[I_0\left(\frac{1}{2}\pi^2 w_0^2 \kappa^2\right) - I_1\left(\frac{1}{2}\pi^2 w_0^2 \kappa^2\right)\right]. \end{aligned} \tag{5.3.10}$$

In Eq. (5.3.10), θ is the azimuthal angle of $\boldsymbol{\kappa}$, I_0 and I_1 are the zero and first order modified Bessel function of the first kind respectively. With Eq. (5.3.9) and Eq. (5.3.10), Eq. (5.3.8) can be written as

$$W(\boldsymbol{\rho}_1, \boldsymbol{\rho}_2, L) = A \exp\left(-\frac{3|\mathbf{r}|^2}{4\rho_0^2}\right) \int U_1(\boldsymbol{\rho}_1, \boldsymbol{\kappa}) {U_1}^*(\boldsymbol{\rho}_2, \boldsymbol{\kappa}) p(\boldsymbol{\kappa}) d^2\kappa, \tag{5.3.11}$$

where

$$p(\boldsymbol{\kappa}) = \pi\rho_0^2 \exp(-\pi^2\rho_0^2\kappa^2) \tag{5.3.12}$$

$$U_1(\boldsymbol{\rho}_j, \kappa) = \tilde{U}(\frac{\boldsymbol{\rho}_j}{\lambda L} - \boldsymbol{\kappa}, 0) \exp(i\pi \boldsymbol{\kappa} \cdot \boldsymbol{\rho}_j) \quad (j = 1, 2). \tag{5.3.13}$$

By comparison between Eq. (5.1.9) and Eq. (5.3.11), it can be seen that the cross-spectral density at the receiver plane [Eq. (5.3.11)] can be explained by the 'beam wander' model [129]. Here $p(\boldsymbol{\kappa})$ [Eq. (5.3.12)], which satisfies $\int p(\boldsymbol{\kappa}) d^2\kappa = 1$, is the probability density function of $\boldsymbol{\kappa}$, corresponding to $f(\boldsymbol{\rho}_0)$ in Eq. (5.1.9). The field

U_1 is centered on a transverse random location $\boldsymbol{\kappa}$, which is limited in a circular area defined by Eq. (5.3.12).

The direct evaluation of Eq. (5.3.11) by substituting Eqs. (5.3.10), (5.3.12), and (5.3.13) is difficult. However, it can be simplified by using the following approximation for $\tilde{U}(\boldsymbol{\kappa}, 0)$

$$\tilde{U}(\boldsymbol{\kappa}, 0) \approx -\frac{i}{2}\pi^{5/2} w_0^3 \kappa \exp(i\theta) \exp\left(-\frac{1}{2}\pi^2 w_0^2 \kappa^2\right). \tag{5.3.14}$$

This expression contains only the lowest nonzero term of the series expansion of the modified Bessel functions in Eq. (5.3.10). The use of Eq. (5.3.14) can be explained by straightforward physical reasoning. The radius of the circular area where the field center wanders is inversely related to ρ_0. For a large ρ_0, the field only wanders in a small area around the origin. Considering the fact that the difference between Eqs. (5.3.10) and (5.3.14) is negligible when the argument is small, the evaluation of Eq. (5.3.11) is accurate for small $|\boldsymbol{\rho}_1|$ and $|\boldsymbol{\rho}_2|$ by substituting Eqs. (5.3.12), (5.3.13), and (5.3.14). On substitution and choosing $(\boldsymbol{\rho}_1, \boldsymbol{\rho}_2)$ to be $(\boldsymbol{\rho}, -\boldsymbol{\rho})$, the approximate cross-spectral density at the receiver plane is

$$\begin{aligned} W(\boldsymbol{\rho}, -\boldsymbol{\rho}, L) &= \frac{\pi^6 w_0^6 \rho_0^2}{4\lambda^2 L^2} \exp\left\{-\left[\frac{\pi^2 w_0^2}{\lambda^2 L^2} + \frac{3}{w_0^2 \sigma_c^2} + \frac{1}{w_0^2(1+\sigma_c^2)}\right]\rho^2\right\} \\ &\times \left[\frac{1}{\pi^3 w_0^4 (1+\sigma_c^2)^2} - \frac{\lambda^2 L^2 + \pi^2 w_0^4 (1+\sigma_c^2)^2}{\pi^3 \lambda^2 L^2 w_0^6 (1+\sigma_c^2)^3}\rho^2\right], \end{aligned} \tag{5.3.15}$$

where

$$\sigma_c = \rho_0 / w_0 \tag{5.3.16}$$

is the relative coherence length which is a measure of the global spatial coherence of a beam on propagation through turbulence. From Eq. (5.3.15), it shows that there exist

spatial correlation singularities at which the amplitude of the cross-spectral density $W(\boldsymbol{\rho}, -\boldsymbol{\rho})$ is zero and the phase is undefined. These spatial correlation singularities form a ring dislocation whose radius is

$$\rho = \lambda L \left[\frac{w_0^2(1+\sigma_c^2)}{\lambda^2 L^2 + \pi^2 w_0^4 (1+\sigma_c^2)^2} \right]^{1/2} . \tag{5.3.17}$$

5.3.2 Examples and Analysis

Eq. (5.3.17) is the central analytical result of this section. However, before applying it to analyze the relationship between the radius of ring dislocation and the turbulence strength parameter C_n^2, it is necessary to give conditions for its accuracy since it is obtained from Eq. (5.3.15) where the approximation Eq. (5.3.14) is used. An example of the absolute value of the cross-spectral density $W(\boldsymbol{\rho}, -\boldsymbol{\rho})$ calculated from Eq. (5.3.15) is shown in Fig. 5.7. As a comparison, the numerical result obtained by simulation is also shown in Fig. 5.7. A multiple phase screen method is used for the simulations. The relative coherence length σ_c is 7.73, which indicates high spatial coherence. As shown by Fig. 5.7, the numerical result of $|W(\boldsymbol{\rho}, -\boldsymbol{\rho})|$ and the analytic result calculated from Eq. (5.3.15) have good agreement in the central area around the origin. The simulated radius of such a ring dislocation is 3 mm, while the radius calculated from Eq. (5.3.17) is 3.2 mm. Therefore, the approximate analytic expression of the radius of a ring dislocation Eq. (5.3.17) is accurate for large relative coherence length σ_c. By numerical simulation, it has been found that Eq. (5.3.17) is accurate when $\sigma_c > 0.9$.

Fig. 5.8 shows the radius of a ring dislocation as a function of the turbulence

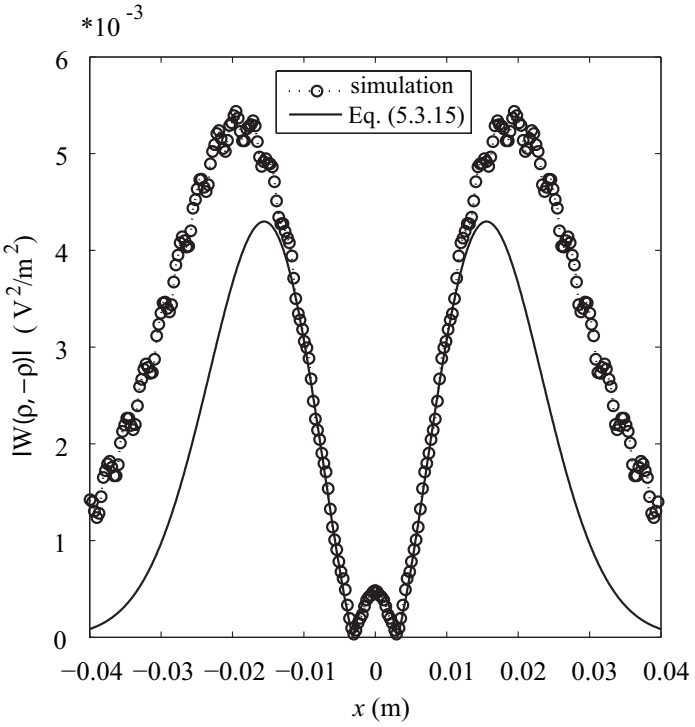

Figure 5.7: The transverse distribution of the absolute value of the cross-spectral density $W(\boldsymbol{\rho}, -\boldsymbol{\rho})$ at the receiver plane ($L = 250$ m). The solid curve represents analytic result calculated from Eq. (5.3.15), while the unfilled shapes ∘ represent numerical result. The wavelength is taken to be $\lambda = 1.55\,\mu$m, $C_n^2 = 10^{-13}$ m$^{-2/3}$, and the beam width is taken to be $w_0 = 5$ mm.

strength parameter C_n^2. It can be seen that the radius of the dislocation increases monotonically with a considerable dynamic range in weak and moderate turbulence, eventually saturating for exceedingly strong turbulence. The simulated radii of some different C_n^2 obtained by propagating a Gaussian beam through a vortex mask and turbulence are also shown in Fig. 5.8. They have good agreement with the radii calculated from Eq. (5.3.17). As the radius of a ring dislocation can be measured by a wavefront folding interferometer [126], Eq. (5.3.17) suggests that C_n^2 can be obtained by measuring the radius of such a ring dislocation at the receiver plane.

It is worth noting that C_n^2 can be obtained by measuring the radius of a ring

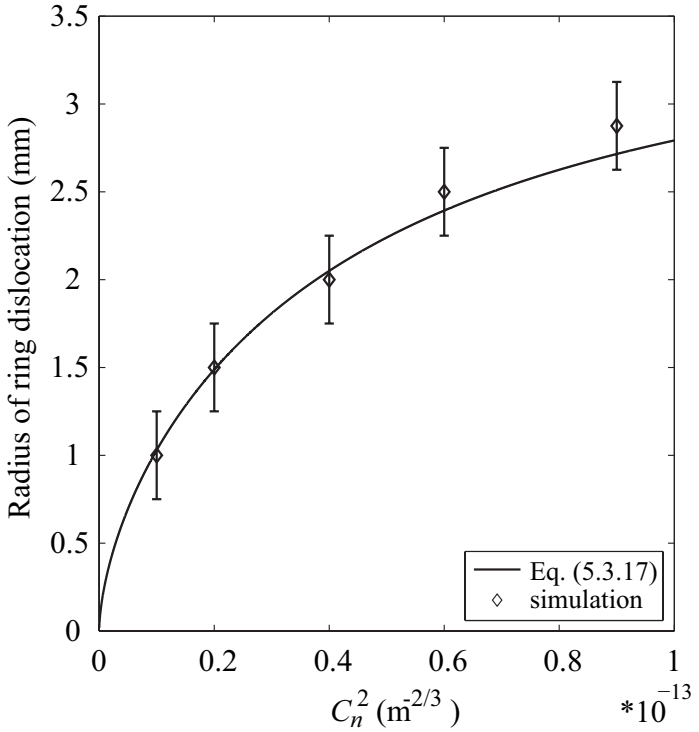

Figure 5.8: Illustration of the radius of a ring dislocation as a function of C_n^2. The solid curve represents analytic result calculated from Eq. (5.3.17), while the unfilled shapes $\diamond$ represent numerical result. The error bars represent the spatial resolution of the simulations. The propagation distance is taken to be $L = 300$ m, $\lambda = 1.55\,\mu$m, and the beam width $w_0 = 4$ cm.

dislocation even in the strong turbulence regime with some modification. As illustrated by Fig. 5.8, the measurement is saturated in the strong turbulence regime. It can be anticipated that the variation of the radius of a ring dislocation is small and therefore C_n^2 may be undistinguishable due to the limited resolution of an imaging system. However, considering the fact that saturation in the strong turbulence regime corresponds to low spatial coherence at the receiver plane, it can be solved by increasing spatial coherence, namely increasing the relative coherence length σ_c by decreasing either the beam width w_0 or the propagation distance L. As shown in Fig. 5.9, for a Gaussian beam with a small beam width ($w_0 = 5$ mm), the

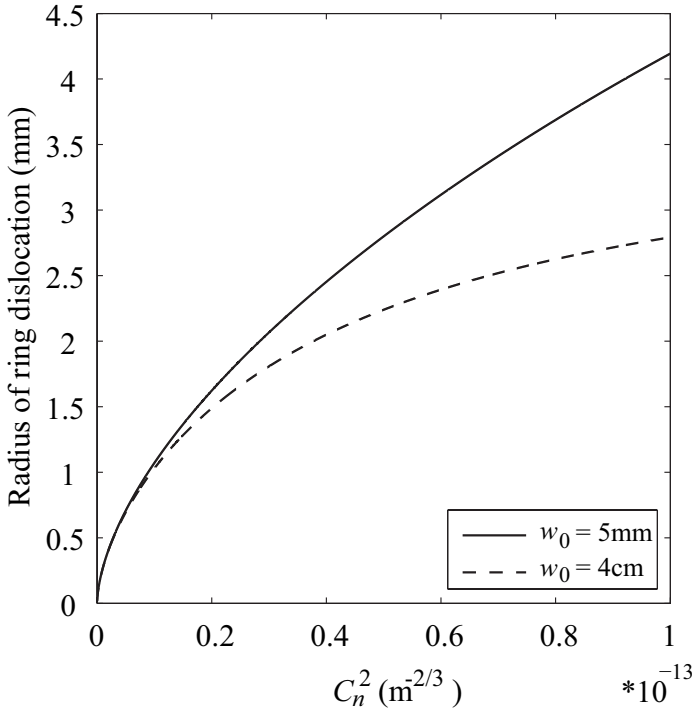

Figure 5.9: Illustration of the radius of a ring dislocation of different beam width w_0. The curves are calculated from Eq. (5.3.17). The propagation distance is taken to be $L = 300$ m and $\lambda = 1.55\,\mu$m.

slope of the corresponding plot is larger than that of the beam with a large beam width ($w_0 = 4$ cm), which indicates a relatively large variation of the radius of ring dislocation even in the strong turbulence regime.

5.4 Summary

In this chapter, the topological behavior of a second-order optical vortex under perturbations was first investigated. Due to the perturbations, the field becomes partially coherent and a second-order optical vortex breaks up into first-order coherence vortices. Their separation is directly related to the strength of perturbations. Inspired by this observation, a method to measure atmospheric turbulence strength by a vortex beam was proposed and its feasibility was

theoretically investigated. It is shown that the atmospheric turbulence strength parameter C_n^2 or its averaged value when C_n^2 is varying on propagation can be obtained by measuring the radius of a ring dislocation after a vortex beam passes through turbulence, even in the saturated regime.

The helical phase structure is crucial for the use of vortex beams in turbulence applications, as it is robust under turbulence perturbations. In principle the method for turbulence strength measurement presented in this chapter can be extended to the measurement of other weakly scattering random media or random fields, such as the statistical parameters of tissue [133] or the coherence length of a Gaussian Schell-model beam. In general, it suggests a relatively straightforward and flexible method to study the statistical properties of a random medium or a random field.

CHAPTER 6: CONCLUSIONS

This dissertation considered the use of nonconventional beam classes in turbulence applications. The scintillation reduction by incoherent beam arrays and nonuniformly polarized beams was investigated with the goal to develop general guides for minimizing beam scintillation on propagation in the atmosphere. The application of vortex beams for atmospheric turbulence strength measurement was also studied.

Scintillation reduction is one of the primary concerns in development of free-space optical communication systems. Through the studies on the scintillation properties of pseudo-Bessel correlated beams, it has been found that the scintillation rapidly decreases to an asymptotic limit as the number of the constituent beamlets is increased. As a partially coherent beam can be decomposed into a collection of infinite incoherent spatial modes, this observation shows that optimal scintillation reduction can be achieved by an incoherent beam array instead of a true partially coherent beam. Since manipulating the coherence properties of an optical beam is still difficult, it suggests that incoherent beam arrays are the promising partially coherent sources for free-space optical communications.

The general guidelines of use of incoherent beam arrays for scintillation reduction were developed. Independence of beamlet propagation in the atmosphere is crucial

for the overall scintillation reduction of a beam array. It can be achieved by enough spatial separation between beamlets so that they propagate through uncorrelated regions of turbulence. The spatial configuration of beam arrays can be either spatially diverse or directionally diverse. It was shown that with appropriate beamlet angular separation, pseudo-Bessel correlated beams, a kind of directionally diverse incoherent beam arrays, can have appreciably small scintillation than comparable fully coherent beams. Besides sufficient beamlet spatial separation, maximizing the received intensity should also be following when designing a incoherent beam array. These two requirements can be met by using a recently discovered special beam class, Airy beams. It was demonstrated that Airy beams propagate along parabolic trajectories in free space and can maintain this unique feature under turbulence-induced perturbations when propagating in the atmosphere. By choosing appropriate beam parameters and suitable initial separation, the beamlets of an Airy beam array can propagate mutually independently in the atmosphere and finally fully overlap to maximize the intensity caught by the detector on the receiver plane. The overall scintillation of the array is significantly reduced.

Scintillation reduction by incoherent beam arrays also relies on the selection of the constituent beamlets with low scintillation. Considering the analogy between a vectorial beam and a two-mode partially coherent beam, it was demonstrated that a nonuniformly polarized beam, composed by LG_{00} and LG_{01} modes, has lower scintillation than comparable beams of uniform polarization. Although its

mechanism for scintillation reduction is also the low correlated mode propagation in turbulence, the low correlation is the result of different mode profiles. It was found that the intensity fluctuations of the LG_{00} and LG_{01} modes could be as low as nearly uncorrelated even though they propagate through the similar regions of turbulence. In addition, the studies on nonuniformly polarized beam propagation in turbulence suggest that beam scintillation might be further reduced if the two orthogonally polarized modes can be negatively correlated on propagation in turbulence.

Techniques for turbulence-induced scintillation reduction also requires knowledge of the turbulence strength which is characterized by the refractive index structure constant C_n^2. The use of vortex beams for atmospheric turbulence strength measurement was investigated. As turbulence-induced decrease of spatial coherence, it was shown that vortex phase structure is transferred from the wavefield function of a coherent vortex beam to the cross-spectral density of a partially coherent vortex beam. It was demonstrated that the atmospheric turbulence strength can be obtained by measuring the radius of the ring dislocation after a vortex beam passes through turbulence.

Over the decades of studies, the propagation behavior of optical beams in the atmosphere has been gradually characterized. Due to the complicated nature of atmospheric turbulence, turbulence effects on optical beam propagation in the atmosphere are involved. The improvement on the performance of any optical system operating in the atmosphere relies on the continuous efforts to deepen the

understanding of the complicated underlying physics of turbulence effects. On the other hand, eyes should be also put on emerging special beam classes whose newly discovered exotic properties may be used in turbulence applications. It is hoped that the results obtained in this dissertation could contribute to this purpose and inspire new ideas for the work of developing 'superbeams' suited for specific turbulence applications.

REFERENCES

[1] P.A. Clayton and M.J. Price. *The Seven Wonders of the Ancient World*. Routledge, New York, NY, 1988.

[2] Zhewen Luo. *The Great Wall of China*. Tsinghua University Press, Beijing, CN, 2008.

[3] The heliograph. *Science*, 1:22, 1880.

[4] J.W. Strohbehn. Optical propagation through the turbulent atmosphere. In E. Wolf, editor, *Progress in Optics*, volume 9, pages 73–122. Elsevier, Amsterdam, NL, 1971.

[5] J.W. Strohbehn, editor. *Laser Beam Propagation in the Atmosphere*. Springer, New York, 1978.

[6] V.I. Tatarskii and V.U. Zavorotnyi. Strong fluctuations in light propagation in a randomly inhomogeneous medium. In E. Wolf, editor, *Progress in Optics*, volume 18, pages 204–256. Elsevier, Amsterdam, NL, 1980.

[7] R.L. Fante. Wave propagation in random media: a system approach. In E. Wolf, editor, *Progress in Optics*, volume 22, pages 341–398. Elsevier, Amsterdam, NL, 1985.

[8] M.I. Charnotskii, J. Gozani, V.I. Tatarskii, and V.U. Zavorotny. Wave propagation theories in random media based on the path-integral approach. In E. Wolf, editor, *Progress in Optics*, pages 203–266. Elsevier, Amsterdam, NL, 1993.

[9] A. Ishimaru. *Wave Propagation and Scattering in Random Media*. IEEE Press, Piscataway, NJ, 1997.

[10] L.C. Andrews and R.L. Phillips. *Laser Beam Propagation through Random Media*. SPIE Press, Bellingham, WA, second edition, 2005.

[11] L.A. Chernov. *Wave Propagation in a Random Medium*. McGraw-Hill, New York, 1960.

[12] V.I. Tatarskii. *Wave Propagation in a Turbulent Medium*. McGraw-Hill, New York, 1961.

[13] M. Born and E. Wolf. *Principles of Optics*. Cambridge University Press, Cambridge, UK, seventh edition, 1999.

[14] D.L. Fried. Limiting resolution looking down through the atmosphere. *J. Opt. Soc. Am.*, 56:1380–1384, 1966.

[15] D.L. Fried. Propagation of a spherical wave in a turbulent medium. *J. Opt. Soc. Am.*, 57:175–180, 1967.

[16] R.A. Schmeltzer. Means, variances, and covariances for laser beam propagation through a random medium. *Q. Appl. Math.*, 24:339–354, 1967.

[17] F.G. Gebhardt and S.A. Collins Jr. Log-amplitude mean for laser-beam propagation in the atmosphere. *J. Opt. Soc. Am.*, 59:1139–1148, 1969.

[18] D.L. Fried and J.B. Seidman. Laser beam scintillations in the atmosphere. *J. Opt. Soc. Am.*, 57:181–185, 1967.

[19] A. Ishimaru. Fluctuations of a beam wave propagating through a locally homogeneous medium. *Radio Sci.*, 4:295–305, 1969.

[20] A. Ishimaru. Flustuations of a focused beam wave for atmospheric turbulence probing. In *Proc. IEEE*, volume 57, pages 407–414, 1969.

[21] M.E. Gracheva and A.S. Gurvich. Strong fluctuations in the intensity of light propagated through the atmosphere close to the earth. *Radiophys. Quantum Electron.*, 8:511–515, 1965.

[22] Z.I. Feizulin and Y.A. Kravtsov. Broadening of a laser beam in a turbulent medium. *Radiophys. Quantum Electron.*, 10:33–35, 1967.

[23] R.F. Lutomirski and H.T. Yura. Propagation of a finite optical beam in an inhomogeneous medium. *Appl. Opt.*, 10:1652–1658, 1971.

[24] H.T. Yura. Mutual coherence function of a finite cross section optical beam propagating in a turbulent medium. *Appl. Opt.*, 11:1399–1406, 1972.

[25] O. Korotkova, M. Salem, A. Dogariu, and E. Wolf. Changes in the polarization ellipse of random electromagnetic beams propagating through the turbulent atmosphere. *Waves Random Complex Media*, 15:353–364, 2005.

[26] Y. Cai, Q. Lin, H.T. Eyyuboğlu, and Y. Baykal. Average irradiance and polarization properties of a radially or azimuthally polarized beam in a turbulent atmosphere. *Opt. Express*, 16:7665–7673, 2008.

[27] Y. Baykal, H.T. Eyyuboğlu, and Y. Cai. Effect of beam types on the scintillations: a review. In *Proc. SPIE*, volume 7200, page 720002, 2009.

[28] K.S. Gochelashvili and V.I. Shishov. Saturated fluctuations in the laser radiation intensity in a turbulent medium. *Sov. Phys. JETP*, 39:605–609, 1974.

[29] A.M. Prokhorov, F.V. Bunkin, K.S. Gochelashvily, and V.I. Shishov. Laser irradiance propagation in turbulent media. In *Proc. IEEE*, volume 63, pages 790–809, 1975.

[30] M.I. Charnotskii. Asymptotic analysis of finite-beam scintillations in a turbulent medium. *Waves Random Media*, 4:243–273, 1994.

[31] M.I. Charnotskii. Beam scintillations for ground-to-space propagation. Part I: Path integrals and analytic techniques. *J. Opt. Soc. Am. A*, 27:2169–2179, 2010.

[32] M.I. Charnotskii. Beam scintillations for ground-to-space propagation. Part 2: Gaussian beam scintillation. *J. Opt. Soc. Am. A*, 27:2180–2187, 2010.

[33] J.M. Martin and S.M. Flatté. Intensity images and statistics from numerical simulation of wave propagation in 3-D random media. *Appl. Opt.*, 27:2111–2126, 1988.

[34] J.M. Martin and S.M. Flatté. Simulation of point-source scintillation through three-dimentional random media. *J. Opt. Soc. Am. A*, 7:838–847, 1990.

[35] B.J. Herman and L.A. Strugala. Method for inclusion of low-frequency contributions in numerical representation of atmospheric turbulence. In *Proc. SPIE*, volume 1221, pages 183–192, 1990.

[36] R.G. Lane, A. Glindemann, and J.C. Dainty. Simulation of a Kolmogorov phase screen. *Waves Random Media*, 2:209–224, 1992.

[37] J.D. Schmidt. *Numerical Simulation of Optical Wave Propagation With examples in MATLAB®*. SPIE Press, Bellingham, WA, 2010.

[38] M.J. Beran. Propagation of the mutual coherence function through random media. *J. Opt. Soc. Am*, 56:1475–1480, 1966.

[39] L.S. Taylor. Decay of mutual coherence in random media. *J. Opt. Soc. Am.*, 57:304–308, 1967.

[40] R.L. Fante. Two-position, two-frequence mutual-coherence function in turbulence. *J. Opt. Soc. Am.*, 71:1446–1451, 1981.

[41] M.S. Belenkii, A.I. Kon, and V.L. Mironov. Turbulent distortions of the spatial coherence of a laser beam. *Sov. J. Quantum Electron*, 7:287–290, 1977.

[42] A.I. Kon and V.I. Tatarskii. On the theory of the propagation of partially coherent light beams in a turbulent atmosphere. *Radiophys. Quantum Electron.*, 15:1187–1192, 1972.

[43] J.C. Leader. Atmospheric propagation of partially coherent radiation. *J. Opt. Soc. Am.*, 67:175–185, 1978.

[44] R.L. Fante. The effect of source temporal coherence on light scintillations in weak turbulence. *J. Opt. Soc. Am.*, 69:71–73, 1979.

[45] J.C. Leader. Intensity fluctuations resulting from partially coherent light propagating through atmospheric turbulence. *J. Opt. Soc. Am.*, 69:73–84, 1979.

[46] R.L. Fante. Intensity fluctuations of an optical wave in a turbulent medium. Effect of source coherence. *Optica Acta*, 28:1203–1207, 1981.

[47] V.A. Banakh, V.M. Buldakov, and V.L. Mironov. Intensity fluctuations of a partially coherent light beam in a turbulent atmosphere. *Opt. Spectroc.*, 54:626–629, 1983.

[48] G. Gbur and E. Wolf. Spreading of partially coherent beams in random media. *J. Opt. Soc. Am. A*, 19:1592–1598, 2002.

[49] A. Dogariu and S. Amarande. Propagation of partially coherent beams: turbulence-induced degradation. *Opt. Lett.*, 28:10–12, 2003.

[50] S.A. Ponomarenko, J.-J. Greffet, and E. Wolf. The diffusion of partially coherent beams in turbulent media. *Opt. Commun.*, 208:1–8, 2002.

[51] T. Shirai, A. Dogariu, and E. Wolf. Mode analysis of spreading of partially coherent beams propagatiing through atmospheric turbulence. *J. Opt. Soc. Am. A*, 20:1094–1102, 2003.

[52] M. Salem, T. Shirai, A. Dogariu, and E. Wolf. Long-distance propagation of partially coherent beams through atmospheric turbulence. *Opt. Commun.*, 2002:261–265, 2002.

[53] X. Ji, X. Chen, and B. Lü. Spreading and directionality of partially coherent hermite-gaussian beams propagating through atmospheric turbulence. *J. Opt. Soc. Am. A*, 25:21–28, 2008.

[54] Y. Dan, B. Zhang, and P. Pan. Propagation of partially coherent flat-topped beams through a turbulent atmosphere. *J. Opt. Soc. Am. A*, 25:2223–2231, 2008.

[55] O. Korotkova, L. C. Andrews, and R. L. Phillips. A model for a partially coherent gaussian beam in atmospheric turbulence with application in lasercom. *Opt. Eng.*, 43:330–341, 2004.

[56] T.J. Schulz. Optimal beams for propagation through random media. *Opt. Lett.*, 30:1093–1095, 2005.

[57] X. Xiao and D. Voelz. Wave optics simulation approach of partially coherent beams. *Opt. Express*, 14:6986–6992, 2006.

[58] D. Voelz and K. Fitzhenry. Pseudo-partially coherent beam for free-space laser communication. In *Proc. SPIE*, volume 5550, pages 218–224, 2004.

[59] X. Qian, W. Zhu, and R. Rao. Numerical investigation on propagation effects of pseudo-partially coherent gaussian schell-model beams in atmospheric turbulence. *Opt. Express*, 17:3782–3791, 2009.

[60] G.P. Berman, A.R. Bishop, B.M. Chernobrod, D.C. Nguyen, and V.N. Gorshkov. Suppression of intensity fluctuations in free space high-speed optical communication based on spectral encoding of a partially coherent beam. *Opt. Commun.*, 280:264–270, 2007.

[61] A. Peleg and J.V. Moloney. Scintillation index for two gaussian laser beams with different wavelengths in weak atmospheric turbulence. *J. Opt. Soc. Am. A*, 23:3114–3122, 2006.

[62] P. Polynkin, A. Peleg, L. Klein, T. Rhoadarmer, and J.V. Moloney. Optimized multiemitter beams for free-space optical communications through turbulent atmosphere. *Opt. Lett.*, 32:885–887, 2007.

[63] A. Peleg and J.V. Moloney. Scintillation reduction by use of multiple gaussian laser beams with different wavelengths. *IEEE Photonics Technol. Lett.*, 19:883–885, 2007.

[64] Y. Baykal, H.T. Eyyuboğlu, and Y. Cai. Scintillations of partially coherent multiple gaussian beams in turbulence. *Appl. Opt.*, 48:1943–1954, 2009.

[65] K. Kiasaleh. On the scintillation index of a multiwavelength gaussian beam in a turbulent free-space optical communications channel. *J. Opt. Soc. Am. A*, 23:557–566, 2006.

[66] J.C. Ricklin and F.M. Davidson. Atmospheric turbulence effects on a partially coherent Gaussian beam: implications for free-space laser communication. *J. Opt. Soc. Am. A*, 19:1794–1802, 2002.

[67] J.C. Ricklin and F.M. Davidson. Atmospheric optical communication with a Gaussian Schell beam. *J. Opt. Soc. Am. A*, 20:856–866, 2003.

[68] C. Chen, H. Yang, X. Feng, and H. Wang. Optimization criterion for initial coherence degree of lasers in free-space optical links through atmospheric turbulence. *Opt. Lett.*, 34:419–421, 2009.

[69] D.G. Voelz and X. Xiao. Metric for optimizing spatially partially coherent beams for propagation through turbulence. *Opt. Eng.*, 48:036001, 2009.

[70] D.K. Borah and D.G. Voelz. Spatially partially coherent beam parameter optimization for free space optimal communications. *Opt. Express*, 18:20746–20758, 2010.

[71] Z. Bouchal and R. Čelechovský. Mixed vortex states of light as information carriers. *New J. Phys.*, 6:131, 2004.

[72] C. Paterson. Atmospheric turbulence and orbital angular momentum of single photons for optical communication. *Phys. Rev. Lett.*, 94:153901, 2005.

[73] N.B. Simpson, K. Dholakia, L. Allen, and M.J. Padgett. Mechanical equivalence of spin and orbital angular momentum of light: an optical spanner. *Opt. Lett.*, 22:52–54, 1997.

[74] L. Allen, S.M. Barnett, and M.J. Padgett. *Optical Angular Momentum*. IOP Press, 2004.

[75] A. Vincott and L. Bergé. Femtosecond optical vortices in air. *Phys. Rev. Lett.*, 95:193901, 2005.

[76] Z. Bouchal. Resistance of nondiffracting vortex beam against amplitude and phase perturbations. *Opt. Commun.*, 210:155–164, 2002.

[77] G. Gbur and R.K. Tyson. Vortex beam propagation through atmospheric turbulence and topological charge conservation. *J. Opt. Soc. Am. A*, 25:225–230, 2008.

[78] J. Broky, G.A. Siviloglou, A. Dogariu, and D.N. Christodoulides. Self-healing properties of optical airy beams. *Opt. Express*, 16:12880–12891, 2008.

[79] E. Wolf. *Introduction to the Theory of Coherence and Polarization of Light*. Cambridge University Press, Cambridge, UK, 2007.

[80] L. Mandel and E. Wolf. *Optical Coherence and Quantum Optics*. Cambridge University Press, Cambridge, UK, 1995.

[81] E. Wolf. New theory of partial coherence in the space-frequency domain. Part I: spectra and cross spectra of steady-state sources. *J. Opt. Soc. Am.*, 72:343–351, 1982.

[82] C.A. Davis and D.L. Walters. Atmospheric inner-scale effects on normalized irradiance variance. *Appl. Opt.*, 33:8406–8411, 1994.

[83] D.H. Tofsted. Outer-scale effects on beam-wander and angle-of-arrival variances. *Appl. Opt.*, 31:5865–5870, 1992.

[84] L.C. Andrews, R.L. Phillips, and C.Y. Hopen. *Laser Beam Scintillation with Applications*. SPIE Press, 2001.

[85] A.N. Kolmogorov. The local structure of turbulence in incompressible viscous fluid for very large Reynolds numbers. *C. R. (Doki) Acad Sci. U.S.S.R.*, 30:301–305, 1941.

[86] S. Corrsin. On the spectrum of isotropic temperature fluctuations in an isotropic turbulence. *J. Appl. Phys.*, 22:469–473, 1951.

[87] F.H. Champange, C.A. Friehe, J.C. LaRue, and J.C. Wyngaard. Flux measurements, flux-estimation techniques, and fine-scale turbulence measurements in the unstable surface layer over land. *J. Atmosp. Sci.*, 34:515–530, 1977.

[88] R.M. Williams and C.A. Paulson. Microscale temperature and velocity spectra in the atmospheric boundary layer. *J. Fluid Mech.*, 83:547–567, 1977.

[89] R.J. Hill. Models of the scalar spectrum for turbulent advection. *J. Fluid Mech.*, 88:541–562, 1977.

[90] L.C. Andrews. An analytical model for the refractive index power spectrum and its application to optical scintillations in the atmosphere. *J. Mod. Opt.*, 39:1849–1853, 1992.

[91] H.T. Yura, C.C. Sung, S.F. Clifford, and R.J. Hill. Second-order Rytov approximation. *J. Opt. Soc. Am.*, 73:500–502, 1983.

[92] A. Stuart and J.K. Ord. *Kendall's Advanced Theory of Statistics*. Oxford University Press, New York, NY, fifth edition, 1987.

[93] H.T. Yura and S.G. Hanson. Second-order statistics for wave propagation thourgh complex optical systems. *J. Opt. Soc. Am. A*, 6:564–575, 1989.

[94] S.M. Wandzura. Meaning of quadratic structure functions. *J. Opt. Soc. Am.*, 70:745–747, 1980.

[95] G.W. Goodman. *Introduction ot Fourier Optics*. Roberts and Company Publishers, Greenwood Village, CO, 2004.

[96] R. Frehlich. Simulation of laser propagation in a turbulent atmosphere. *Appt. Opt.*, 39:393–397, 2000.

[97] G. Gbur. Simulating fields of arbitrary spatial and temporal coherence. *Opt. Express*, 14:7567–7578, 2006.

[98] F. Gori, G. Guattaria, and C. Padovani. Modal expansion of J_0-correlated schell-model sources. *Opt. Commun.*, 64:311–316, 1987.

[99] J. Durnin, J.J. Miceli, Jr., and J.H. Eberly. Diffraction-free beams. *Phys. Rev. Lett.*, 58:1499–1501, 1987.

[100] J. Durnin. Exact solutions for nondiffracting beams. I. The scalar theory. *J. Opt. Soc. Am. A*, 4:651–654, 1987.

[101] Z. Bouchal, J. Wagner, and M. Chlup. Self-reconstruction of a distorted nondiffracting beam. *Opt. Commun.*, 151:207–211, 1998.

[102] J. Turunen, A. Vasara, and A.T. Friberg. Propagation invariance and self-imaging in variable-coherence optics. *J. Opt. Soc. Am. A*, 8:282–289, 1991.

[103] A.T. Friberg, A. Vasara, and J. Turunen. Partially coherent propagation-invariant beams: Passage through paraxial optical systems. *Phys. Rev. A*, 43:7079–7082, 1991.

[104] C. Palma, R. Borghi, and G. Cincotti. Beams originated by j_0-correlated schell-model planar sources. *Opt. Commun.*, 125:113–121, 1996.

[105] G. Gbur and T.D. Visser. Can spatial coherence effects produce a local minimum of intensity at focus? *Opt. Lett.*, 28:1627–1629, 2003.

[106] G.B. Arfken and H.J. Weber. *Mathematical Methods for Physicists*. Academic Press, San Diego, CA, fourth edition, 1995.

[107] X. Xiao, J. Aluguri, and D. Voelz. Wave optics simulation study of multiple gaussian beam transmitters for free space optical transmission through turbulence. In *Proc. SPIE*, volume 7200, page 72000K, 2009.

[108] M.V. Berry and N.L. Balazs. Nonspreading wave packets. *Am. J. Phys.*, 47:264–267, 1979.

[109] G.A. Siviloglou and D.N. Christodoulides. Accelerating finite energy airy beams. *Opt. Lett.*, 32:979–981, 2007.

[110] G.A. Siviloglou, J. Broky, A. Dogariu, and D.N. Christodoulides. Observation of accelerating airy beams. *Phys. Rev. Lett.*, 99:213901, 2007.

[111] G.A. Siviloglou, J. Broky, A. Dogariu, and D.N. Christodoulides. Ballistic dynamics of airy beams. *Opt. Lett.*, 33:207–209, 2008.

[112] M. Salem, O. Korotkova, A. Dogariu, and E. Wolf. Polarization changes in partially coherent em beams propagating through turbulent atmosphere. *Waves in Random Media*, 14:513–523, 2004.

[113] O. Korotkova. Scintillation index of a stochastic electromagnetic beam propagating in random media. *Opt. Commun.*, 281:2342–2348, 2008.

[114] K. Youngworth and T. Brown. Focusing of high numerical aperture cylindrical-vector beams. *Opt. Express*, 7:77–87, 2000.

[115] T. Wang and J. Pu. Propagation of non-uniformly polarized beams in a turbulent atmosphere. *Opt. Commun.*, 281:3617–2622, 2008.

[116] W. Chen, J.W. Haus, and Q. Zhan. Propagation of vector vortex beam through a turbulent atmosphere. *Opt. Express*, 17:17829–17836, 2009.

[117] Q. Zhan. Cylindrical vector beams: from mathematical concepts to applications. *Adv. Opt. Photon.*, 1:1–57, 2009.

[118] Y. Kozawa and S. Sato. Generation of a radial polarized laser beam by use of a conical brewster prism. *Opt. Lett.*, 30:3063–3065, 2007.

[119] A.V. Artem'ev and A.S. Gurvich. Experimental study of coherence-function spectra. *Radiophys. Quantum Electron.*, 14:580–583, 1971.

[120] T. Wang, G.R. Ochs, and S.F. Clifford. A saturation-resistant optical scintillometer to measure c_n^2. *J. Opt. Soc. Am.*, 68:334–338, 1978.

[121] R.J. Hill and G.R. Ochs. Inner-scale dependence of scintillation variances measured in weak scintillation. *J. Opt. Soc. Am. A*, 9:1406–1411, 1992.

[122] M.S. Soskin and M.V. Vasnetsov. Singular optics. In E. Wolf, editor, *Progress in Optics*, volume 42, page 201. Elsevier, Amsterdam, 2001.

[123] J.F. Nye and M.V. Berry. Dislocations in wave trains. *Proc. R. Soc. Lond. A*, 336:165–190, 1974.

[124] H.F. Schouten, G. Gbur, T.D. Visser, and E. Wolf. Phase singularities of the coherence functions in Young's interference pattern. *Opt. Lett.*, 28:968–970, 2003.

[125] G. Gbur and T.D. Visser. Coherence vortices in partially coherent beams. *Opt. Commun.*, 222:117–125, 2003.

[126] D.M. Palacios, I.D. Maleev, A.S. Marathay, and G.A. Swartzlander, Jr. Spatial correlation singularity of a vortex field. *Phys. Rev. Lett.*, 92:143905, 2004.

[127] I.D. Maleev, D.M. Palacios, A.S. Marathay, and G.A. Swartzlander, Jr. Spatial correaltion vortices in partially coherent light: theory. *J. Opt. Soc. Am. B*, 21:1895–1900, 2004.

[128] G. Gbur. *Mathematical Methods for Optical Physics and Engineering*. Cambridge Univeristy Press, Cambridge, UK, 2011.

[129] G. Gbur, T.D. Visser, and E. Wolf. 'Hidden' singularities in partially coherent wavefields. *Pure Appl. Opt.*, 6:S239, 2004.

[130] G. Gbur and T.D. Visser. Phase singularities and coherence vortices in linear optical systems. *Opt. Commun.*, 259:428–435, 2005.

[131] G.A. Swartzlander, Jr. and R.I. Hernandez-Aranda. Optical rankine vortex and anomalous circulation of light. *Phys. Rev. Lett.*, 99:169301, 2007.

[132] I.D. Maleev and G.A. Swartzlander, Jr. Propagation of spatial correlation vortices. *J. Opt. Soc. Am. B*, 25:915–922, 2008.

[133] W. Gao and O. Korotkova. Changes in the state of polarization of a random electromagnetic beam propagating through tissue. *Opt. Commun.*, 270:474–478, 2007.

APPENDIX A: DERIVATION OF E_1^n, E_2^{mn}, and E_3^{mn}

In this Appendix, the expressions for E_1^n, E_2^{mn}, and E_3^{mn} in Sec. 3.1 [Eqs. (3.1.14)-(3.1.16)] are derived in detail. They are the second order statistical moments which are defined as

$$E_1^n(\boldsymbol{\rho}, L) =< \psi_{n2}(\boldsymbol{\rho}, L) > + \frac{1}{2} < \psi_{n1}(\boldsymbol{\rho}, L) >^2, \tag{A.1}$$

$$E_2^{mn}(\boldsymbol{\rho}, L) =< \psi_{m1}(\boldsymbol{\rho}, L)\psi_{n1}^*(\boldsymbol{\rho}, L) >, \tag{A.2}$$

$$E_3^{mn}(\boldsymbol{\rho}, L) =< \psi_{m1}(\boldsymbol{\rho}, L)\psi_{n1}(\boldsymbol{\rho}, L) > . \tag{A.3}$$

The expressions for the average intensity $< I_n(\boldsymbol{\rho}, L) >$ [Eq. (3.1.12)] and the average cross-intensity $< I_m(\boldsymbol{\rho}, L)I_n(\boldsymbol{\rho}, L) >$ [Eq. (3.1.13)] can be obtained by the similar derivations as shown in Ref. [10] and Ref. [61] respectively.

By the Rytov approximation, the wavefield in the turbulence can be expressed by Eq. (3.1.8). For the n^{th} beamlet specified by Eqs. (3.1.6) and (3.1.7), it can be shown that by using the angular spectrum theory the wavefield at the receiver plane $z = L$ in the absence of the turbulence is

$$A_{0n}(\boldsymbol{\rho}, L) = \frac{1}{\sqrt{N}p(L)} \exp\left[ikL - \frac{\rho^2}{p(L)w_0^2}\right] \exp\left[\frac{i(2k\mathbf{u}_{\perp n} \cdot \boldsymbol{\rho} - kLu_{\perp n}^2)}{2p(L)}\right]. \tag{A.4}$$

The first order complex phase perturbation term $\psi_{n1}(\boldsymbol{\rho}, L)$ can be evaluated by the following equation [[10], Chapter 5, Eq. (36)]

$$\psi_{n1}(\boldsymbol{\rho}, L) = \frac{k^2}{2\pi} \int_0^L dz \int \exp\left[ik(L-z) + \frac{ik|\mathbf{s} - \boldsymbol{\rho}|^2}{2(L-z)}\right] \frac{A_{0n}(\mathbf{s}, z)}{A_{0n}(\boldsymbol{\rho}, L)} \frac{n_1(\mathbf{s}, z)}{L-z} d^2s. \tag{A.5}$$

$n_1(\boldsymbol{\rho}, z)$ is the turbulence-induced refractive index fluctuation which can be written

in the following form

$$n_1(\boldsymbol{\rho}, z) = \iint \exp(i\boldsymbol{\kappa}\cdot\boldsymbol{\rho}) dv(\boldsymbol{\kappa}, z), \tag{A.6}$$

where $dv(\boldsymbol{\kappa}, z)$ is the random amplitude of $n_1(\boldsymbol{\rho}, z)$. On substituting Eqs. (A.4) and (A.6) into Eq. (A.5), the following expression is obtained,

$$\begin{aligned}
\psi_{n1}(\boldsymbol{\rho}, L) &= ik \exp\left[\frac{ikLu_{\perp n}^2}{2p(L)}\right] \int_0^L \exp\left\{\frac{-ik}{2p(z)}\left[z + \frac{\gamma(z)(L-z)}{p(z)}\right] u_{\perp n}^2\right\} dz \\
&\times \iint \exp\left[-\frac{i\gamma(z)(L-z)\kappa^2}{2k}\right] \exp\left[i\gamma(z)\boldsymbol{\kappa}\cdot\boldsymbol{\rho}\right] \\
&\times \exp\left[-\frac{i\gamma(z)(L-z)}{p(z)}\boldsymbol{\kappa}\cdot\mathbf{u}_{\perp n}\right] dv(\boldsymbol{\kappa}, z),
\end{aligned} \tag{A.7}$$

where again $\gamma(z) = \frac{p(z)}{p(L)}$. E_2^{mn} can be obtained by substituting Eq. (A.7) into Eq. (A.2). With the relationship

$$< dv(\boldsymbol{\kappa}, z) dv^*(\boldsymbol{\kappa}', z') >= F_n(\boldsymbol{\kappa}, |z - z'|)\delta(\boldsymbol{\kappa} - \boldsymbol{\kappa}') d^2\kappa d^2\kappa', \tag{A.8}$$

where δ is the Dirac delta function and $F_n(\boldsymbol{\kappa}, |z - z'|)$ is a two dimensional spectral density of the turbulence, it can be shown that, after some calculations,

$$\begin{aligned}
E_2^{mn}(\boldsymbol{\rho}, L) &= k^2 \exp\left[\frac{ikLu_{\perp m}^2}{2p(L)}\right] \exp\left[\frac{-ikLu_{\perp n}^2}{2p^*(L)}\right] \\
&\times \int_0^L \int_0^L \exp\left\{\frac{-ik}{2p(z)}\left[z + \frac{\gamma(z)(L-z)}{p(z)}\right] u_{\perp m}^2\right\} \\
&\times \exp\left\{\frac{ik}{2p^*(z')}\left[z' + \frac{\gamma^*(z')(L-z')}{p^*(z')}\right] u_{\perp n}^2\right\} dz dz' \\
&\times \iint \exp\left\{-\frac{i}{2k}\left[\gamma(z)(L-z) - \gamma^*(z')(L-z')\right]\kappa^2\right\} \\
&\times \exp\left\{-i\boldsymbol{\kappa}\cdot\left[\frac{L-z}{p(L)}\mathbf{u}_{\perp m} - \frac{L-z'}{p^*(L)}\mathbf{u}_{\perp n}\right]\right\} \\
&\times \exp\left\{i\left[\gamma(z) - \gamma^*(z')\right]\boldsymbol{\kappa}\cdot\boldsymbol{\rho}\right\} F_n(\boldsymbol{\kappa}, |z - z'|) d^2\kappa.
\end{aligned} \tag{A.9}$$

Now the integration variables z and z' are replaced by $\eta = (z + z')/2$ and $\mu = z - z'$. With the assumption that the turbulence is delta correlated in the propagation direction, $F_n(\boldsymbol{\kappa}, \mu)$ has the appreciable values only when $\mu \approx 0$. Thus the integration on μ can be extended to be from $-\infty$ to ∞ without significant error and let $z \approx z' \approx \eta$. With these approximations and the relationship between $F_n(\boldsymbol{\kappa}, \mu)$ and the power spectrum of the turbulence $\Phi_n(\boldsymbol{\kappa})$

$$\Phi_n(\boldsymbol{\kappa}) = \frac{1}{2\pi} \int_{-\infty}^{\infty} F_n(\boldsymbol{\kappa}, \mu) d\mu, \tag{A.10}$$

Eq. (A.9) can reduce to the expression

$$\begin{aligned} E_2^{mn}(\boldsymbol{\rho}, L) &= 2\pi k^2 \exp\left[\frac{ikLu_{\perp m}^2}{2p(L)}\right] \exp\left[\frac{-ikLu_{\perp n}^2}{2p^*(L)}\right] \\ &\times \int_0^L \exp\left\{\frac{-ik}{2p(\eta)}\left[\eta + \frac{\gamma(\eta)(L-\eta)}{p(\eta)}\right] u_{\perp m}^2\right\} \\ &\times \exp\left\{\frac{ik}{2p^*(\eta)}\left[\eta + \frac{\gamma^*(\eta)(L-\eta)}{p^*(\eta)}\right] u_{\perp n}^2\right\} d\eta \\ &\times \int \exp\left\{\frac{-i\left[\gamma(\eta) - \gamma^*(\eta)\right](L-\eta)\kappa^2}{2k}\right\} \exp\left\{i\left[\gamma(\eta) - \gamma^*(\eta)\right]\boldsymbol{\kappa} \cdot \boldsymbol{\rho}\right\} \\ &\times \exp\left\{-i(L-\eta)\boldsymbol{\kappa} \cdot \left[\frac{\mathbf{u}_{\perp m}}{p(L)} - \frac{\mathbf{u}_{\perp n}}{p^*(L)}\right]\right\} \Phi_n(\boldsymbol{\kappa}) d^2\kappa, \end{aligned} \tag{A.11}$$

which is Eq. (3.1.15) for E_2^{mn}. Eq. (3.1.16) for E_3^{mn} can be obtained by a similar derivation except that the following relationship is used

$$< dv(\boldsymbol{\kappa}, z) dv(\boldsymbol{\kappa}', z') >= F_n(\boldsymbol{\kappa}, |z - z'|)\delta(\boldsymbol{\kappa} + \boldsymbol{\kappa}') d^2\kappa d^2\kappa'. \tag{A.12}$$

For E_1^n defined as Eq. (A.1), it has been shown that it is equivalent to the ensemble average of the second order normalized Born perturbation term [[10], Chapter 5, Eqs. (35) and (39)]. Therefore, it can be derived by using the following equation [[10],

Chapter 5, Eq. (40)]

$$
\begin{aligned}
E_1^n(\boldsymbol{\rho}, L) &= \frac{k^2}{2\pi}\int_0^L dz \int \exp\left[ik(L-z) + \frac{ik|\mathbf{s}-\boldsymbol{\rho}|^2}{2(L-z)}\right] \\
&\times \frac{A_{0n}(\mathbf{s}, z)}{A_{0n}(\boldsymbol{\rho}, L)} \frac{<\psi_{n1}(\mathbf{s}, z) n_1(\mathbf{s}, z)>}{L-z} d^2 s. \qquad \text{(A.13)}
\end{aligned}
$$

On substituting Eqs. (A.4), (A.6) and (A.7) into Eq. (A.13), it can be shown that, after integrating with respect to the variable $\mathbf{s}$,

$$
\begin{aligned}
E_1^n(\boldsymbol{\rho}, L) &= -k^2 \exp\left[\frac{ikLu_{\perp n}^2}{2p(L)}\right] \\
&\times \int_0^L dz \int_0^z dz' \exp\left\{-\frac{ik}{2}\left[\frac{z'}{p(z')} + \frac{\gamma'(z-z')}{p^2(z')} + \frac{\gamma(L-z)}{p^2(z)}\right] u_{\perp n}^2\right\} \\
&\times \int\int\int\int_{-\infty}^{\infty} < dv(\boldsymbol{\kappa}, z) dv(\boldsymbol{\kappa}', z') > \exp\left[-\frac{i\gamma'(z-z')\kappa'^2}{2k}\right] \\
&\times \exp\left[-\frac{i\gamma'(z-z')}{p(z')}\boldsymbol{\kappa}' \cdot \mathbf{u}_{\perp n}\right] \exp\left[-\frac{i\gamma(L-z)|\boldsymbol{\kappa} + \gamma'\boldsymbol{\kappa}'|^2}{2k}\right] \\
&\times \exp\left[-\frac{i\gamma(L-z)}{p(z)}(\boldsymbol{\kappa} + \gamma'\boldsymbol{\kappa}') \cdot \mathbf{u}_{\perp n}\right] \exp\left[i\gamma(\boldsymbol{\kappa} + \gamma'\boldsymbol{\kappa}') \cdot \boldsymbol{\rho}\right], \qquad \text{(A.14)}
\end{aligned}
$$

where $\gamma = \frac{p(z)}{p(L)}$ and $\gamma' = \frac{p(z')}{p(z)}$. Eq. (A.14) can be simplified by using the relationship Eq. (A.12) and the similar approximations as applied in the derivation of E_2^{mn}. Recognizing that $\gamma' \approx 1$ and the integration on μ is from 0 and ∞, it can reduce to

$$
\begin{aligned}
E_1^n(\boldsymbol{\rho}, L) &= -\pi k^2 \exp\left[\frac{ikLu_{\perp n}^2}{2p(L)}\right] \int \Phi_n(\boldsymbol{\kappa}) d^2\kappa \\
&\times \int_0^L \exp\left[\frac{-ik\eta u_{\perp n}^2}{2p(\eta)}\right] \exp\left[\frac{-ik\gamma(\eta)(L-\eta)u_{\perp n}^2}{2p^2(\eta)}\right] d\eta, \qquad \text{(A.15)}
\end{aligned}
$$

which is Eq. (3.1.14).

APPENDIX B: RADIUS OF RING DISLOCATION AS A VARYING C_n^2

This appendix is used to show that when the refractive index structure constant C_n^2 is varying during propagation, the average value $\bar{C}_n^2$ can still be obtained by measuring the radius of a ring dislocation at the receiver plane.

As illustrated by Fig. B.1, atmospheric turbulence between the transmitter plane and the receiver plane can be divided into slabs of equal thickness. By the slow-varying assumption, C_n^2 in each slab is a constant and the difference of C_n^2 in each two adjacent slabs is small. The propagation in the first two slabs is taken as an example. By the extended Huygens-Fresnel principle and the quadratic approximation of the random phase structure function, the cross-spectral densities at the plane $z = L/n$ and $z = 2L/n$ are

$$\begin{aligned} W_1(\boldsymbol{\rho}_{11}, \boldsymbol{\rho}_{12}) \;\propto\; & \iint W_0(\boldsymbol{\rho}_1', \boldsymbol{\rho}_2') \exp\left[-\frac{ink}{2L}(|\boldsymbol{\rho}_{11} - \boldsymbol{\rho}_1'|^2 - |\boldsymbol{\rho}_{12} - \boldsymbol{\rho}_2'|^2)\right] \\ & \times \exp\left(-\frac{|\mathbf{r}_1|^2 + \mathbf{r}_1 \cdot \mathbf{r}' + |\mathbf{r}'|^2}{\rho_{01}^2}\right) d^2\rho_1' d^2\rho_2' \end{aligned} \tag{B.1}$$

$$\begin{aligned} W_2(\boldsymbol{\rho}_{21}, \boldsymbol{\rho}_{22}) \;\propto\; & \iint W_1(\boldsymbol{\rho}_{11}, \boldsymbol{\rho}_{12}) \exp\left[-\frac{ink}{2L}(|\boldsymbol{\rho}_{21} - \boldsymbol{\rho}_{11}|^2 - |\boldsymbol{\rho}_{22} - \boldsymbol{\rho}_{12}|^2)\right] \\ & \times \exp\left(-\frac{|\mathbf{r}_2|^2 + \mathbf{r}_2 \cdot \mathbf{r}_1 + |\mathbf{r}_1|^2}{\rho_{02}^2}\right) d^2\rho_{11} d^2\rho_{12}, \end{aligned} \tag{B.2}$$

where $W_0(\boldsymbol{\rho}_1', \boldsymbol{\rho}_2')$ is the cross-spectral density at the transmitter plane, $\mathbf{r}' = \boldsymbol{\rho}_2' - \boldsymbol{\rho}_1'$, $\mathbf{r}_1 = \boldsymbol{\rho}_{12} - \boldsymbol{\rho}_{11}$, $\mathbf{r}_2 = \boldsymbol{\rho}_{22} - \boldsymbol{\rho}_{21}$, $\rho_{01} = (0.55 C_{n1}^2 k^2 \frac{L}{n})^{-3/5}$ and $\rho_{02} = (0.55 C_{n2}^2 k^2 \frac{L}{n})^{-3/5}$. For convenience, the new variables $(\mathbf{R}', \mathbf{r}')$, $(\mathbf{R}_1, \mathbf{r}_1)$ and $(\mathbf{R}_2, \mathbf{r}_2)$ are introduced, where $\mathbf{R}' = (\boldsymbol{\rho}_2' + \boldsymbol{\rho}_1')/2$, $\mathbf{R}_1 = (\boldsymbol{\rho}_{12} + \boldsymbol{\rho}_{11})/2$ and $\mathbf{R}_2 = (\boldsymbol{\rho}_{22} + \boldsymbol{\rho}_{21})/2$. On substituting Eq. (B.1) into Eq. (B.2) and taking integral with respect to $(\mathbf{R}_1, \mathbf{r}_1)$, the cross-spectral

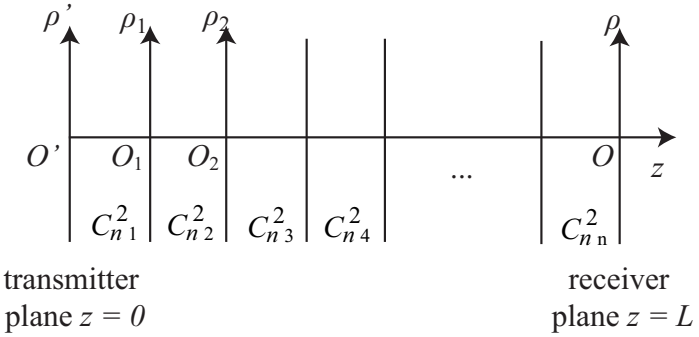

Figure B.1: Illustration of the propagation geometry in the case of varying C_n^2. The whole propagation path is divided into n slabs. The thickness of each slab is L/n. C_{ni}^2 is the refractive index structure constant in the i^{th} slab, while $i = 1, 2...n$.

density at plane $z = 2L/n$ can be written as

$$\begin{aligned} W_2(\mathbf{R}_2, \mathbf{r}_2) &\propto \int d^2R' \int d^2r' W_0(\mathbf{R}', \mathbf{r}') \\ &\times \exp\left[-\frac{(\rho_{02}^2 + 7\rho_{01}^2)|\mathbf{r}_2|^2 + 4(\rho_{01}^2 + \rho_{02}^2)\mathbf{r}_2 \cdot \mathbf{r}' + (7\rho_{01}^2 + \rho_{02}^2)|\mathbf{r}'|^2}{4\rho_{01}^2\rho_{02}^2} \right] \\ &\times \exp\left[\frac{ink}{2L}(\mathbf{R}' \cdot \mathbf{r}' + \mathbf{R}_2 \cdot \mathbf{r}_2 - \mathbf{R}' \cdot \mathbf{r}_2 - \mathbf{R}_2 \cdot \mathbf{r}') \right]. \end{aligned} \tag{B.3}$$

By the assumption of small difference of C_n^2 in the two adjacent slabs, it can be assumed that

$$\rho_{02}^2 + 7\rho_{01}^2 \approx 4(\rho_{01}^2 + \rho_{02}^2) \approx 7\rho_{01}^2 + \rho_{02}^2 \approx 8\bar{\rho_{12}}^2, \tag{B.4}$$

where $\bar{\rho_{12}}$ is the average coherence length of a spherical wave in the first two slabs. On substituting Eq. (B.4), Eq. (B.3) can be written as

$$\begin{aligned} W_2(\mathbf{R}_2, \mathbf{r}_2) &\propto \int d^2R' \int d^2r' W_0(\mathbf{R}', \mathbf{r}') \exp\left[-\frac{2\bar{\rho_{12}}^2(|\mathbf{r}_2|^2 + \mathbf{r}_2 \cdot \mathbf{r}' + |\mathbf{r}'|^2)}{\rho_{01}^2\rho_{02}^2} \right] \\ &\times \exp\left[\frac{ink}{2L}(\mathbf{R}' \cdot \mathbf{r}' + \mathbf{R}_2 \cdot \mathbf{r}_2 - \mathbf{R}' \cdot \mathbf{r}_2 - \mathbf{R}_2 \cdot \mathbf{r}') \right]. \end{aligned} \tag{B.5}$$

$W_2(\mathbf{R}_2, \mathbf{r}_2)$ can also be calculated from $W_0(\mathbf{R}', \mathbf{r}')$ by the extended Huygens-Fresnel

principle directly, which is

$$\begin{aligned} W_2(\mathbf{R}_2, \mathbf{r}_2) &\propto \int d^2R' \int d^2r' W_0(\mathbf{R}', \mathbf{r}') \exp\left(-\frac{|\mathbf{r}_2|^2 + \mathbf{r}_2 \cdot \mathbf{r}' + |\mathbf{r}'|^2}{\bar{\rho_{12}}^2}\right) \\ &\times \exp\left[\frac{ink}{2L}(\mathbf{R}' \cdot \mathbf{r}' + \mathbf{R}_2 \cdot \mathbf{r}_2 - \mathbf{R}' \cdot \mathbf{r}_2 - \mathbf{R}_2 \cdot \mathbf{r}')\right]. \end{aligned} \tag{B.6}$$

By comparing Eqs. (B.5) and (B.6), one can find that

$$\bar{\rho_{12}}^2 = \frac{1}{\sqrt{2}} \rho_{01} \rho_{02}. \tag{B.7}$$

When the field is propagating into the third slab, the first two slabs can be treated as unity whose average coherence length of a spherical wave is $\bar{\rho_{12}}$. By a similar derivation, one can show that the average coherence length of a spherical wave in the whole propagation path L is

$$\bar{\rho_0}^2 = 2^{-\frac{1}{2}-2(\frac{1}{2})^n} \rho_{01}^{\frac{1}{2^{n-2}}} \rho_{02}^{\frac{1}{2^{n-2}}} \prod_{i=3}^{n} \rho_{0i}^{\frac{1}{2^{n-i}}} \quad (n \geq 3), \tag{B.8}$$

where

$$\begin{aligned} \bar{\rho_0} &= (0.55 \bar{C_n^2} k^2 L)^{-3/5} \\ \rho_{0i} &= (0.55 C_{ni}^2 k^2 \frac{L}{n})^{-3/5} \quad (i = 1, 2...n). \end{aligned} \tag{B.9}$$

It can be readily seen that the average value $\bar{C_n^2}$ can be measured by the radius of a ring dislocation when it is varying along the propagation path, while $\bar{C_n^2}$ is defined by Eqs. (B.8) and (B.9).